University of Lille

Doctoral School ED SMRE

Department of Physics

PhLAM: Laboratory of Physics of Lasers, Atoms, and Molecules
Building P5 – 2 Avenue Jean Perrin – 59655 Villeneuve d'Ascq – Cedex – France.

Cerla: Center for Laser Studies and Research Applications
Cité scientifique – 59655 Villeneuve d'ascq – Cedex – France.

Thesis defended by **Tony Mathew Blessan**

Defended on **24 February 2026**

To become a Doctor from the University of Lille

Academic Field **Physics**

Specialty **Diluted Media And Fundamental Optics**

Transport, localization and orbital line lasing in driven-dissipative polariton lattices

---

Thesis supervised by:	DR Alberto Amo Garcia	Director
President of the jury	DR Sylvain Barbay	University of Paris-Saclay
Jury composition		
Referees	PR Thierry Guillet	University of Montpellier
	PR Barbara Pietka	University of Warsaw
Examiner	PR Dmitry Solnyshkov	University of Clermont-Auvergne
	DR Sylvain Barbay	University of Paris-Saclay
Director	DR Alberto Amo Garcia	University of Lille

Transport, localization and orbital line lasing in driven-dissipative polariton lattices, © 24 February 2026

Université de Lille

École doctorale ED SMRE

Département de physique

PhLAM: Laboratoire de Physique des Lasers, Atomes et Molécules
Building P5 – 2 Avenue Jean Perrin – 59655 Villeneuve d'Ascq – Cedex – France.

Cerla: Centre d'Études et de Recherches Lasers et Applications
Cité scientifique – 59655 Villeneuve d'ascq – Cedex – France.

Thèse présentée par **Tony Mathew Blessan**

Soutenue le **24 février 2026**

En vue de l'obtention du grade de docteur de l'Université de Lille

Discipline **Physique**

Spécialité **Milieux dilués et optique fondamentale**

Transport, localisation et émission laser orbitale en ligne dans des réseaux de polaritons sous forçage et dissipation

---

Thèse dirigée par:	DR Alberto Amo Garcia	Directeur
Président du jury	DR Sylvain Barbay	Université de Paris-Saclay
Composition du jury		
Rapporteurs	PR Thierry Guillet	Université de Montpellier
	PR Barbara Pietka	Université de Warsaw
Examinateur	PR Dmitry Solnyshkov	Université de Clermont-Auvergne
	DR Sylvain Barbay	Université de Paris-Saclay
Directeur	DR Alberto Amo Garcia	Université de Lille

Transport, localisation et émission laser orbitale en ligne dans des réseaux de polaritons sous forçage et dissipation, © 24 février 2026

TABLE OF CONTENT

Abstract

Transport, localization and orbital line lasing in driven-dissipative polariton lattices.

The implementation of lattice Hamiltonians in driven–dissipative photonic platforms offers new routes to control transport, localization, and lasing beyond what is accessible in equilibrium solid-state systems. In this thesis, we experimentally and numerically investigate these properties using a hybrid light-matter quasiparticle called exciton–polaritons in semiconductor lattices with non-trivial band structures in the presence of gain, loss and particle interactions. In the first part, we study a one-dimensional chain of coupled micropillars and show that interference between coherent drives and lattice eigenmodes enables phase-controlled directional transport and interference-induced localization. Furthermore, by increasing the pump power, we demonstrate nonlinearity-enabled localization at detunings where the linear system remains only weakly localized. In the second part, we engineer a two-dimensional Lieb sp lattice where the s and p orbital modes of two pillars with different diameters are hybridized to form line-like eigenmodes. Using spatially structured non-resonant pumping, we realize reconfigurable line lasing and show that cross-shaped excitation produces two orthogonal line lasers that lock in energy, phase, and polarization. Finally, we develop a driven–dissipative lattice lasing model that identifies orbital coupling and reservoir-induced blueshift as the minimal ingredients required for this phase locking. Overall, this work highlights polariton lattices as a powerful system for tailoring interference, band structure, and nonlinearity to realize unconventional transport, localization, and lasing phenomena that are difficult to achieve in lattices with trivial band structures.

Keywords: *Exciton polaritons, Semiconductor micropillars, Drive and dissipation, Interference, Lieb sp lattice, Orbital line lasing, Cross locking laser.*

Résumé

Transport, localisation et émission laser orbitale en ligne dans des réseaux de polaritons sous forçage et dissipation.

L'implémentation d'Hamiltoniens décrivant des réseaux dans des plateformes photoniques sous forçage et dissipation ouvre de nouvelles voies pour contrôler le transport, la localisation et l'émission laser, au-delà de ce qui est accessible dans les systèmes à l'état solide à l'équilibre. Dans cette thèse, nous étudions expérimentalement et numériquement ces propriétés en utilisant une quasi-particule hybride lumière–matière, l'exciton-polariton, dans des réseaux semi-conducteurs à structures de bandes non triviales en présence de gain, de pertes et d'interactions entre particules. Dans une première partie, nous étudions une chaîne unidimensionnelle de micropiliers couplés et montrons que l'interférence entre excitations cohérentes et modes propres du réseau permet de réaliser un transport directionnel contrôlé par la phase ainsi qu'une localisation induite par interférence. En augmentant la puissance de pompage, nous démontrons en outre une localisation permise par la non-linéarité, à des désaccords pour lesquels le système linéaire reste seulement faiblement localisé. Dans une deuxième partie, nous concevons un réseau de Lieb sp bidimensionnel, dans lequel les modes orbitaux s et p de deux micropiliers de diamètres différents sont hybridés pour former des modes propres de type ligne. À l'aide d'un pompage non résonant spatialement structuré, nous réalisons une émission laser en ligne reconfigurable et montrons qu'une excitation en forme de croix produit deux lasers en ligne orthogonaux qui se verrouillent en énergie, en phase et en polarisation. Enfin, nous développons un modèle d'émission laser dans un réseau sous forçage et dissipation qui identifie le couplage orbital et le décalage vers le bleu induit par le réservoir comme ingrédients minimaux nécessaires à ce verrouillage de phase. Globalement, ce travail met en évidence les réseaux de polaritons comme une plateforme puissante pour façonner l'interférence, la structure de bande et la non-linéarité, afin de réaliser des phénomènes de transport, de localisation et d'émission laser non conventionnels, difficiles à obtenir dans des réseaux à structure de bande triviale.

Mots-clés: *Excitons-polaritons, micropiliers semi-conducteurs, forçage et dissipation, interférence, réseau de Lieb sp, émission laser orbitale en ligne, laser à verrouillage croisé.*

ACKNOWLEDGMENTS

Looking back on one of the most important chapters of my life over the past three years in France, I realize that this thesis is not only the result of academic effort, but also the result of love, support, patience and encouragement of the people who stood by me through every stage of this journey.

Firstly, I thank Almighty God for giving me strength and perseverance throughout this journey.

I express my deepest gratitude to my PhD Director Prof. Alberto Amo Garcia. Coming to a country so far from my own, with a language and culture that were completely unfamiliar to me, was a true leap of faith not only for me, but also for my supervisor, who believed in me from the very beginning. Your confidence in my potential and your guidance throughout this journey helped me grow as a researcher. Beyond academic supervision, he taught me to think critically, explore and truly understand the deeper meaning behind scientific work. I will always remember the book "The Structure of Scientific Revolutions" that you gifted me, because it marked a beautiful beginning to this journey and helped me understand not only how science is done, but why it should be done.

A special mention goes to my co-supervisor Dr. Clément Hainaut, who played an important role in shaping this thesis work. I have always admired your pedagogical approach, which played a crucial role in helping me carry out both my experimental and numerical work in a more systematic and rigorous manner.

I also wish to acknowledge the administrative teams, the P5 team, the CERLA team, and the PhLAM team for their kindness and assistance. Their unseen efforts greatly helped create an environment that was both encouraging and conducive to my research.

My heartfelt thanks go to the members of the jury for kindly accepting our request to evaluate this thesis and for the insightful comments they have given to my work. I am honored by their presence during the defence and for their valuable remarks.

A special and heartfelt thanks to my master's supervisor Prof. Yogesh Natesan, whose influence has been deeply important in my life. He helped me to lay the foundation of my scientific rigour and shaped the way I reflect on society and its political realities. His teachings have left a lasting mark on both my intellectual

growth and my understanding of the world.

This milestone would not have been possible without the care and encouragement I received from so many people. During my stay in France, I had the privilege of meeting remarkable individuals, many of whom became close friends. To all of you, I will always cherish the memories we created together. Reaching this point would not have been conceivable without you. However, among them, there are a few friends whom I owe a particularly special mention: Cécilia Ouarkoub, Rabih El Sokhen, Rajesh Kumari Rajendran, Abdu Subahan Mohammed, Nathalie Moubarak, Ribal Beyrouti, Rajesh Asapanna, Clarisse Fournier, Kayce Ouahrouch. Each of you made this chapter of my life richer and far more memorable in your own way.

My deepest affection goes to my family, from my grandmother to each of my uncles and aunts, who have been the foundation of every step I have taken on this journey and life. To my parents, no words will ever be enough to express what I owe you for your sacrifices and for the unconditional love you have always showered upon me. To my sister, you have always had a special place in my life as the person to whom I turn to whenever I stand before an important decision. Your advice, understanding and constant presence have guided me through so many moments, and your love and warmth remain forever. To my brother-in-law and all my cousins, you have truly been pillars in my life. Knowing that I could always count on you has been one of the greatest blessings. This highest academic degree is not my accomplishment alone; it is a shared achievement that belongs to all of you.

Finally, to my wife and dearest friend, Mrs. Divya Sherin, who has been with me for around 8 years, words cannot hardly express what your presence has meant to me. Your love, companionship, and unwavering support have carried me through every high and low, and this chapter of my life would not have been the same without you.

This thesis work has been a space of learning, growth, and self-discovery. I have made mistakes, learned from them, and have come to believe that this is how one truly grows not in perfection, but in reflection, humility, and perseverance. For that reason, I do not see this as an ending, but as the beginning of a new chapter, one that I hope will be guided by purpose, responsibility, and the desire to contribute, in whatever way I can, to building a better world for all.

> *"The philosophers have only interpreted the world, in various ways; the point is to change it."- Karl Marx.*

DECLARATION OF AUTHORSHIP

I, Tony Mathew Blessan, born in Kerala, India, on April 19, 1997, declare that all the material in this thesis, entitled '*Transport, localization and orbital line lasing in driven-dissipative polariton lattices*', is the product of my work. I certify that I conducted this research primarily while pursuing a research degree at the University of Lille from December 2022 to February 2026.

Except for instances explicitly cited within the thesis, I have not incorporated any material previously published or sourced from another thesis for any degree or diploma. All contributions from other individuals have been duly acknowledged within the body of the thesis. Furthermore, this thesis has not been presented for the attainment of any other degree or diploma from any other educational institution.

Signature: Tony Mathew Blessan 24 February 2026

PUBLICATIONS

This thesis entitled *'Transport, localization and orbital line lasing in driven-dissipative polariton lattices'* presents original research conducted by the author. Some sections of this work have been published or are currently under review. Permission has been obtained from the respective publishers to reproduce and incorporate these materials in this thesis for academic purposes.

Some of the results and figures presented herein may appear in future publications after the submission of this thesis.

- **Tony Mathew Blessan**, Bastián Real, Camille Druelle, Clarisse Fournier, Alberto Muñoz de las Heras, Alejandro González-Tudela, Isabelle Sagnes, Abdelmounaim Harouri, Luc Le Gratiet, Aristide Lemaître, Sylvain Ravets, Jacqueline Bloch, Clément Hainaut, and Alberto Amo, *Directional transport and nonlinear localization of light in a one-dimensional driven-dissipative photonic lattice*, Physical Review Research, vol. 7, p. 033283, 25 Sep. 2025. DOI: 10.1103/b3wk-r8r3.

- **Tony Mathew Blessan**, Bastián Real, Clément Hainaut, Marijana Milicevic, Isabelle Sagnes, Abdelmounaim Harouri, Luc Le Gratiet, Aristide Lemaître, Sylvain Ravets, Jacqueline Bloch, and Alberto Amo, *Line lasing in a two-dimensional lattice of orbital photonic resonators*. The article was submitted to OPTICA on 21 Dec. 2025. The preprint is available on arXiv: 2512.18719.

Except for the references cited in this thesis, no part of its content has been copied or derived, in whole or in part, from any previously approved thesis or dissertation. The main content of this thesis contains no unacknowledged material drawn from the research or publications of others. This thesis has not been submitted, either in full or in part, to any other university or institution for the award of a degree or diploma.

INTRODUCTION

Artificial lattices are engineered structures that replicate the periodicity and coupling patterns of crystalline solids but for classical or quantum waves instead of electrons [1, 2]. By carefully designing the geometry and interaction between discrete sites whether optical cavities, microwave resonators, or acoustic scatterers these platforms can emulate the physics of tight binding models originally developed for solid state systems [2–4]. At the heart of this analogy is the tight-binding Hamiltonian, which describes a particle or wave hopping between discrete sites with a characteristic coupling strength [4, 5]. In artificial lattices, this coupling corresponds to physical parameters such as optical tunneling between waveguides, evanescent coupling between resonators, or acoustic wave overlap between scatterers. This mapping enables experimental platforms with high control over lattice geometry, boundary conditions, and coupling strengths, allowing them to emulate a wide range of band-structure and topological phenomena [2, 4, 5].

Artificial lattices have been realized across a wide range of platforms: In photonic crystals, periodic modulation of the refractive index creates bandgaps and dispersion resembling electron bands [6, 7]. In laser-written waveguide arrays, light propagation along the longitudinal axis simulates time evolution in tight-binding chains [1]. In microwave and acoustic resonator networks, localized modes are coupled through near-field interactions to form artificial band structures [3, 8]. These systems have enabled the exploration of fundamental wave phenomena such as: 1) Bloch oscillations: oscillatory motion of wavepackets under external potential gradients [1, 9, 10]. 2) Topological edge states, where waves propagate uni-directionally along boundaries [11–14]. 3) Flat band localization, where interference leads to compact localized states even without disorder [15, 16].

What makes artificial lattices particularly interesting is it's tunability and observability they offer: parameters like coupling strength, disorder or dimensionality can be precisely engineered, and both real-space and spectral responses can often be directly measured [1, 5, 10, 17]. As a result, these systems serve as highly controllable testbeds to explore wave transport, localization, and topological physics in a variety of classical and quantum regimes [1, 5, 10, 12].

In contrast to conservative (Hermitian) systems, where energy is conserved and dynamics are unitary, photonic and polaritonic implementations of artificial lattices are typically realized as open systems. In such lattices, energy is continuously exchanged with the environment through external driving (e.g. optical or electrical pumping) and dissipation (e.g. radiative losses, absorption). For il-

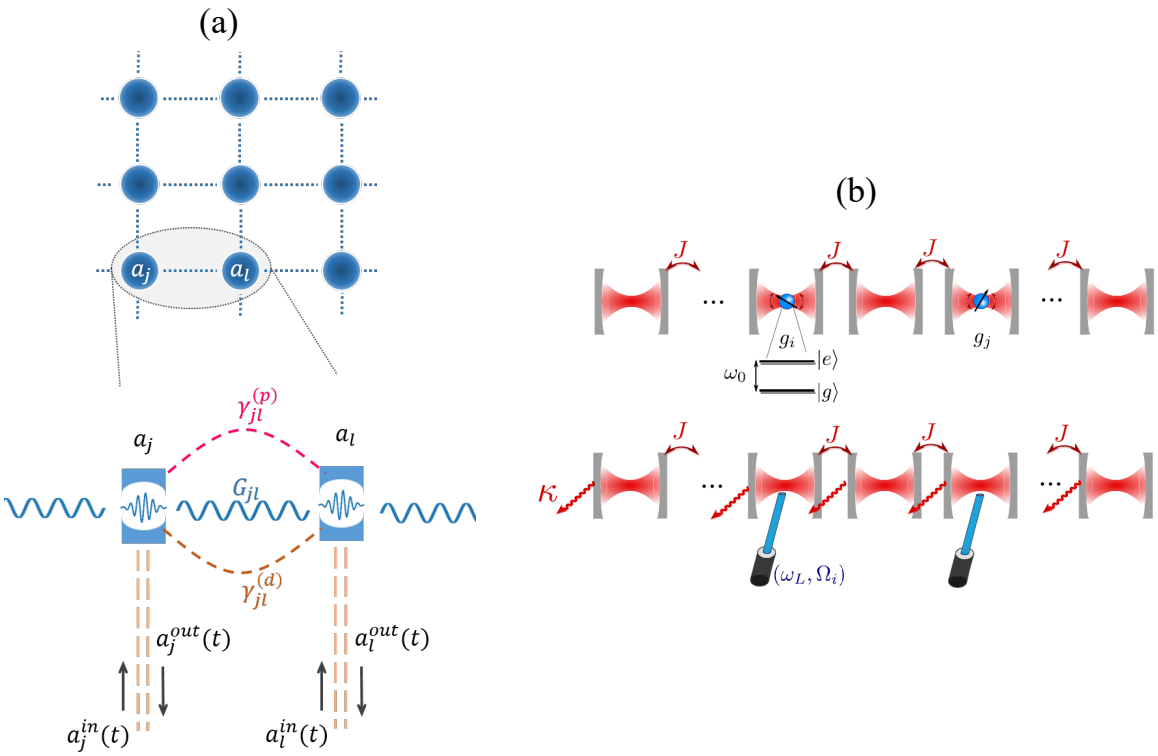

Figure 0.1: (a) Schematic representation of a photonic lattice with zoomed view of two sites having input/ouput fields and couplings where G_{jl} is a coherent, photon tunneling term, whereas $\gamma_{jl}^{(p)}$ and $\gamma_{jl}^{(d)}$ are dissipative gain and loss couplings, respectively. Taken from [18]. (b) Quantum emitter and driven-dissipative configuration: quantum emitters with nearest-neighbour hopping J having one or several lasers with frequency ω_L and amplitude Ω_0 driving locally the cavities of the coupled cavity array of loss rate κ. Taken from [19].

lustration, Fig. 0.1 shows schematic examples of such driven–dissipative lattices which include the hopping, pumping and loss processes. Consequently, steady states are not equilibrium ground states of a conservative Hamiltonian, but non-equilibrium steady states set by a dynamical balance between gain and loss [20]. This class of systems, commonly referred to as driven–dissipative lattices, is naturally described by lattice models with hopping supplemented by drive and loss terms in the form of driven Bose–Hubbard or Jaynes–Cummings–Hubbard arrays governed by a Lindblad master equation framework [20, 21]. As a result, driven–dissipative lattices exhibit non-equilibrium behavior, including complex eigenvalue spectra [22], non-thermal steady states [21], and mode selectivity governed by gain saturation and nonlinear interactions rather than energy minimization [23]. These features give rise to rich physics beyond traditional band theory and make driven–dissipative artificial lattices a versatile platform for exploring non-Hermitian and non-equilibrium phenomena [20–23].

For these reasons, over the past decade, driven-dissipative systems have become fertile grounds for exploring new phenomena. In particular, they have enabled the observation of 1) Exceptional points and non-Hermitian degeneracies, where both

eigenvalues and eigenvectors coalesce [24, 25]. 2) Parity-time (PT) symmetric systems, exhibiting sharp phase transitions between real and complex spectra [26, 27]. 3) Non-Hermitian skin effects in lattices with asymmetric (non-reciprocal) couplings, where modes accumulate at boundaries even in periodic lattices [22, 28, 29]. 4) mode competition between different spatial, spectral, or polarization modes of the lattice [30, 31], leading to non-linear phenomena such as bistability [32–34], mode locking [35, 36], and multistability [37, 38]. These phenomena illustrate how driven–dissipative lattices go beyond Hermitian systems, offering access to tunable, non-equilibrium behavior. In practice, this tunability can be realized either by engineering gain and loss via non-resonant pumping or, in resonantly driven implementations, by tailoring the coherent pump through its amplitude, phase, detuning, polarization, and spatial pattern that control the populated modes and the resulting effective non-Hermitian dynamics.

Although many of the phenomena discussed above can, in principle, be realized in a variety of artificial lattices, most existing photonic implementations remain non-reconfigurable: the band structure and localization properties are fixed by the geometry and refractive-index profile and are difficult to modify once fabricated. A particularly suitable platform to overcome these limitations is provided by exciton-polariton lattices that allow both resonant (coherent) and non-resonant (incoherent) pumping. Exciton–polaritons (microcavity polaritons) are hybrid light-matter quasiparticles that arise from the strong coupling between quantum-well excitons (i.e. bound electron-hole pairs) and confined photons in a semiconductor microcavity, leading to a characteristic mode splitting into upper and lower polariton branches [39]. Because polaritons are superpositions of photons and excitons, their properties inherit contributions from both components. From the photonic part, polaritons acquire an extremely small effective mass (about 10^{-5} times the mass of free electrons) and the ability to leak out of the cavity as photons that encode the full information on the polariton field corresponding to its amplitude, phase, energy, polarization (pseudospin) and coherence. This direct optical readout allows one to reconstruct band structures for studying transport properties via photoluminescence experiments. From the excitonic part, polaritons inherit strong non-linear interactions and a spin degree of freedom, which make them sensitive to external control using magnetic fields [40–42]. Therefore, the combination of a flexible photonic landscape with sizable excitonic interactions provides a driven-dissipative lattice platform in which transport and localization properties can be fundamentally explored and engineered.

Thanks to modern lithography and etching techniques, microcavity polaritons can be laterally confined to cylindrically symmetric mesas of a few micrometers in diameter, known as micropillars. In these structures, the in-plane motion of polaritons is quantized, giving rise to a discrete set of confined modes (s, p, d, ...) in close analogy with the electronic levels of an atom. Individual micropillars therefore act as artificial atoms and can be used as the basic building blocks of

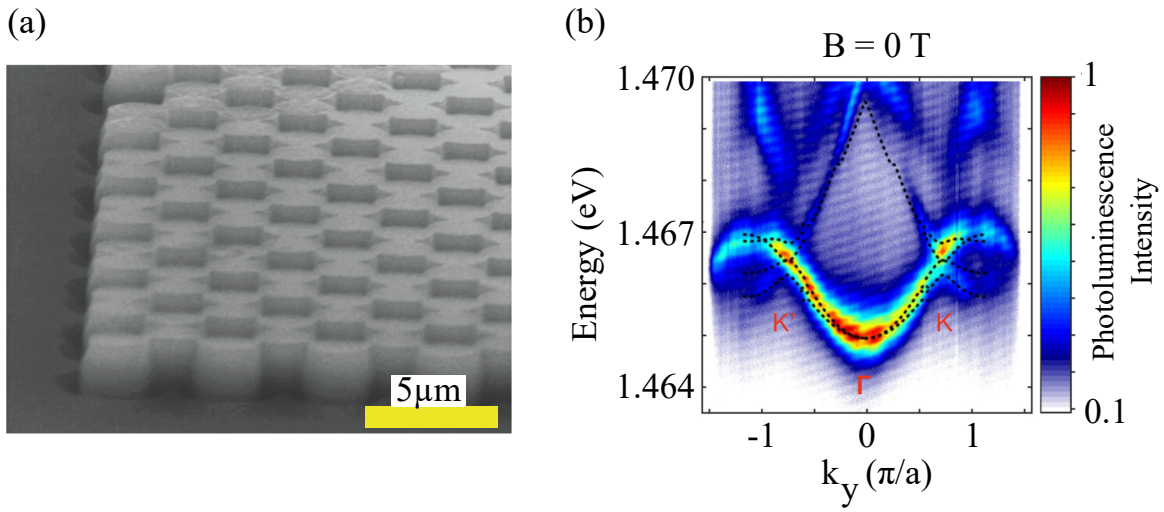

Figure 0.2: (a) Tilted SEM view of the half-etched honeycomb lattice of micropillars. (b) Measured lower-polariton dispersion along the ($K' \rightarrow \Gamma \rightarrow K$) direction at ($B = 0$ T) where black dots indicate the corresponding band structure calculated from a Bloch-mode model for the same honeycomb geometry. Taken from [43].

polariton lattices. By arranging several micropillars in a way that their photonic modes overlap, one- and two-dimensional arrays can be realized (an example is shown in Fig. 0.2(a). The resulting collective modes form polariton bands that are described by a tight-binding model [44] (as shown in Fig. 0.2(b)) with well-defined onsite energies and hopping amplitudes. In practice, this control can be most conveniently realized experimentally in microstructured cavities such as micropillar lattices, where the in-plane potential is defined by etching the cavity layer into coupled pillars. The driven–dissipative nature of polaritons allows localiza-

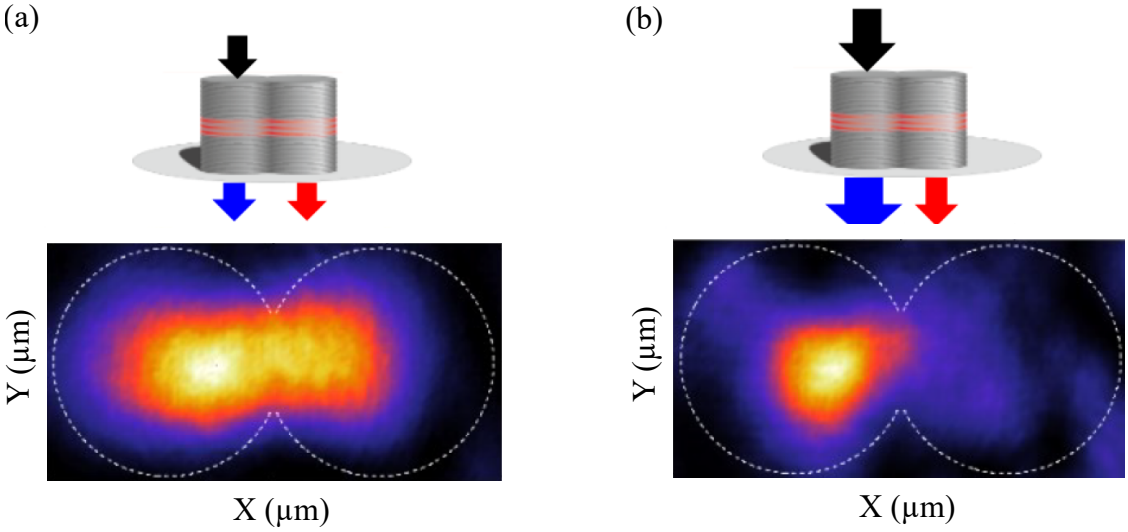

Figure 0.3: Real-space emission from a resonantly driven polariton dimer, showing the transition from a de-localized two-site mode (a) to a self-localized state on the driven cavity as the pump power (non-linearity) increases (b). Taken from [45].

tion to be engineered by shaping pump and loss: for example, spatially structured pumping in a honeycomb lattice creates localized gap states whose emission forms

localized lasing modes [46]. Localization can also be realized with resonant pumping. For example, in a polariton dimer, coherently driving only one of the two sites excites a superposition of the bonding and antibonding modes. Repulsive polariton–polariton interactions shift the energies of these modes in a population dependent way, such that the population distribution between the two sites depends on the total density. This leads to multi-stable, self-trapped states in which most of the polaritons remain localized at the driven site [45]. An illustration of this phenomenon is presented in Fig. 0.3(a,b). In lattices with flat bands, localization instead originates from destructive interference imposed by the lattice geometry, and the combination of interactions and resonant driving gives rise to non-linear localized solitons built from the flat-band manifold, such as discrete gap solitons in one dimension and compact localized states in two dimensions, with polariton densities pinned to only a few micropillars [47, 48].

Interference-based localization in lattices, particularly in the non-linear regime, has been explored theoretically, but experimental demonstrations remain scarce. This gap leads to one of the central questions in this thesis: how can interference between external drives and lattice eigenmodes be actively used to achieve robust control of transport in linear regime and localization in non-linear settings experimentally?

Recently, it has been demonstrated that external drives can be used as an additional control knob: by tailoring the spatial profile and phase of the pump, one can engineer interference between the drive and the lattice eigenmodes, and thereby control transport properties without modifying the lattice itself [49–52]. Some earlier work by members of our group has already explored this idea. Jamadi et al. [49] demonstrated reconfigurable localization within a honeycomb lattice of lossy micropillars. By resonantly driving the lattice with multiple laser spots at energies inside the photonic bands, they were able to localize light down to a single lattice site of micrometer scale. Real et al. [50] performed a numerical study of a square photonic lattice driven at energies near a saddle point of its band structure, where light propagation is strongly anisotropic. By manipulating the phase and placement of multiple coherent drives, they engineered interference between the drives and lattice modes to obtain quasi-1D, uni-directional bulk propagation, as well as drive-induced localized states with controllable localization length. Muñoz de las Heras et al. [51, 52] theoretically examined how Kerr non-linearity affects interference-based driven–dissipative localization in 1D and 2D photonic lattices. They showed that nonlinearities do not destroy this localization; instead, extend it to pump frequencies where the linear system would remain delocalized ("nonlinearity-enabled localization"). These localized states appear precisely where the total intensity inside the lattice is minimal, with nonlinear signatures such as optical bistability being strongly suppressed.

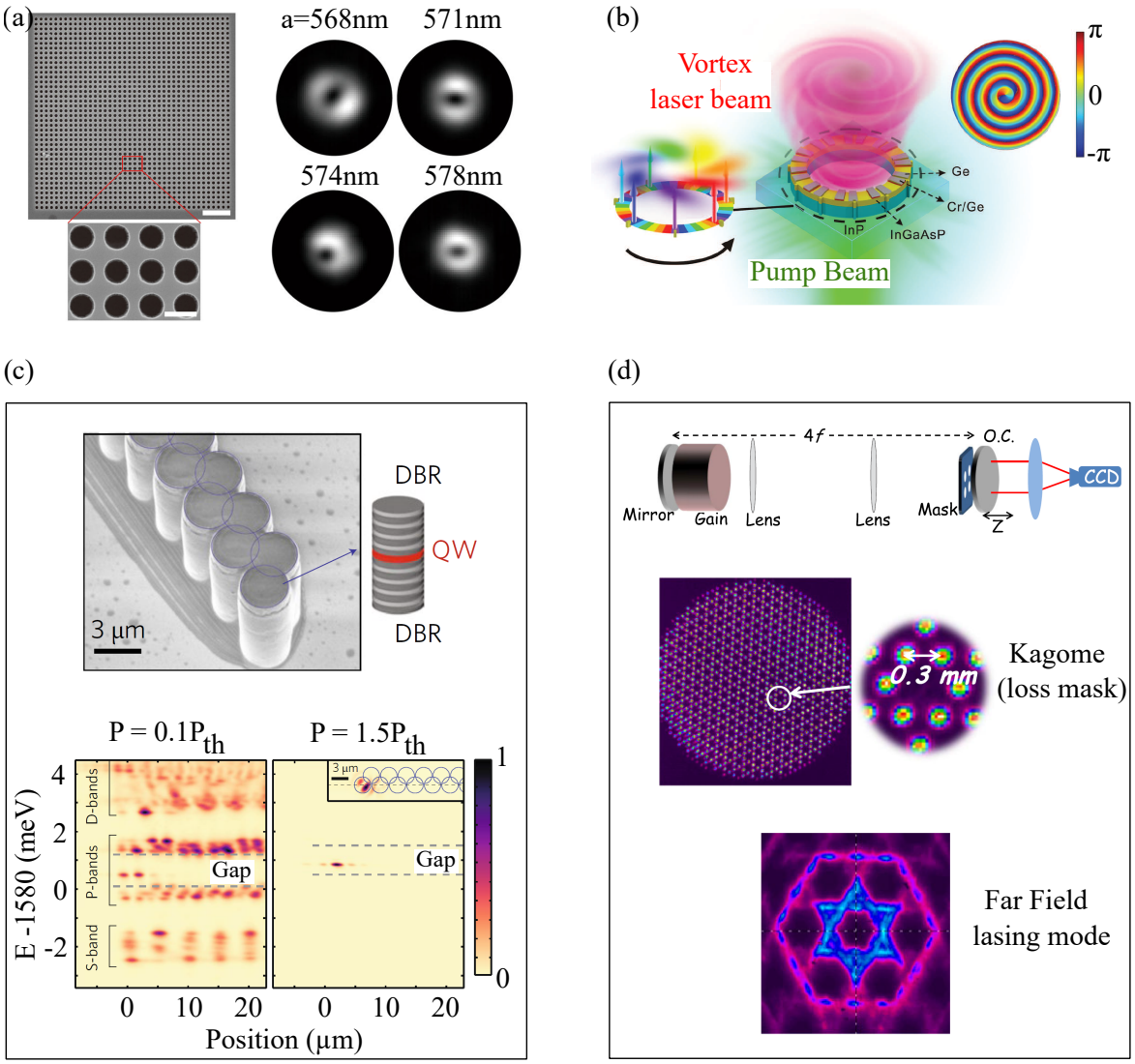

Figure 0.4: (a) SEM images of the BIC laser array ($a = 563\,\text{nm}$, 40×40 unit cells; scale bars $3\,\mu\text{m}$ and $500\,\text{nm}$) and measured far-field patterns of symmetry-protected BIC modes for different a. Taken from [53] (b) Schematic of the OAM microlaser on an InP substrate with simulated spiral phase of the emitted light (OAM charge $l = 1$). Taken from [54] (c) Topological micropillar laser based on a zigzag chain of coupled micropillars embedding QWs between DBRs, showing lasing from a topological edge mode in the bandgap. Taken from [55] (d) Degenerate cavity with a masked gain medium imaged onto a back mirror in a $4f$ telescope. A kagome-shaped loss mask selects $\sim$ 1500 coupled Gaussian beams forming a $2D$ kagome laser lattice. The far-field interference recorded on a CCD shows broad bow-tie features instead of sharp peaks, revealing frustrated phase locking and the absence of long-range phase order. Taken from [56].

Another key feature of driven–dissipative photonic lattices is their ability to lase into engineered spatial or topological modes. Because the gain can be spatially structured, lattice eigenmodes overlap with gain in different ways; together with mode-dependent losses and gain saturation, this leads to non-linear mode competition so that only selected modes reach the threshold. This mechanism has been exploited to achieve 1) robust single-mode lasing in photonic-crystal nanocavities protected by symmetry or topology based on bound states in the continuum, where symmetry protection strongly suppresses competing modes even in a multimode spectrum [53]; 2) vortex microlasers that emit light with a well-defined and tunable orbital angular momentum, where non-Hermitian engineering and controlled symmetry breaking select a chiral OAM lasing mode [54, 57]; and 3) topological lasers in which lasing occurs in edge modes protected by the band topology [55]. Few of these phenomena are shown in Fig. 0.4. Together, these capabilities position driven-dissipative lattices as a powerful system to study lasing through the interplay of gain and loss [56, 58].

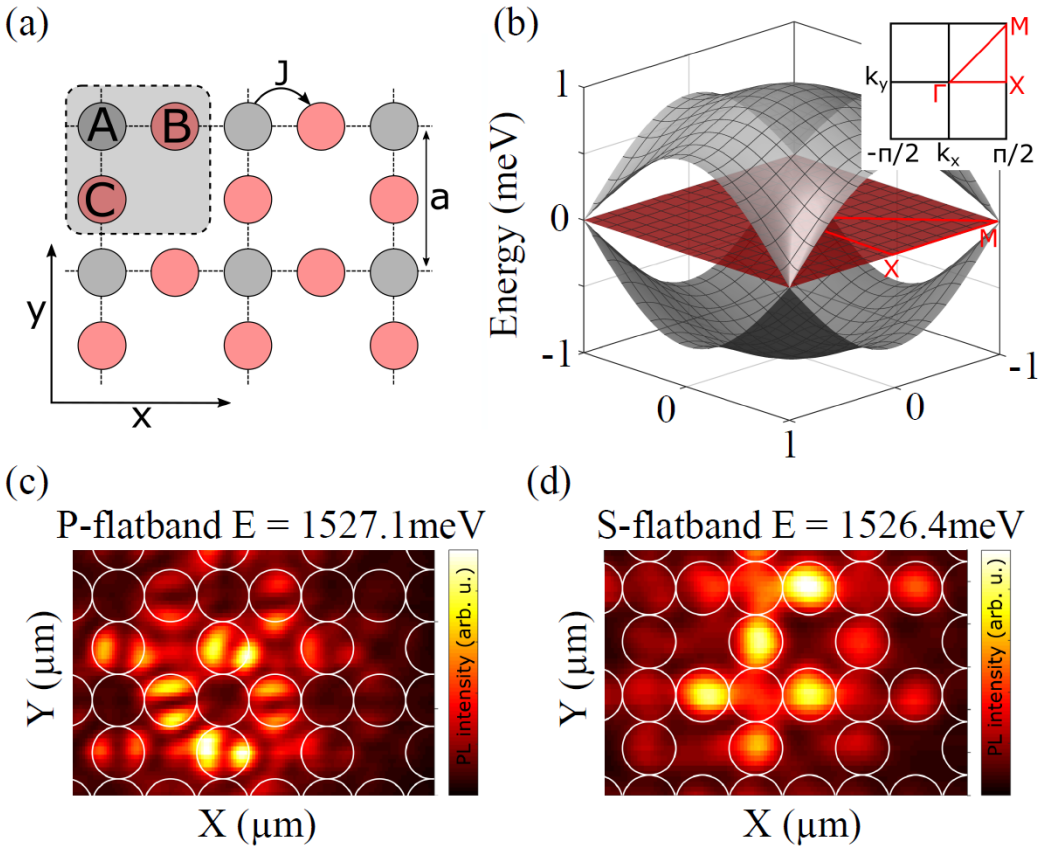

Figure 0.5: (a) Schematic of the two-dimensional Lieb lattice with A, B, and C sites (unit cell in gray box). (b) Tight-binding band structure showing a flatband (red) and Dirac-cone dispersions at the M points. (c) Real-space emission from the P-flatband condensate at $E = 1527.1meV$. (d) Real-space emission from the S-flatband condensate at $E = 1526.4meV$. Taken from [59].

In exciton-polariton lattices, polariton condensation in Lieb lattices has already been demonstrated in two key works of [59, 60] where they observed condensation into S and P flat-bands of a two-dimensional Lieb lattice of identical micropillars, and highlighted the role of orbital degrees of freedom and spin-orbit coupling in shaping the flat-band condensates. However, in both cases, the lasing modes are extended two-dimensional flat-band modes. Fig. 0.5(a,b) shows the Lieb lattice and its band dispersion, while panels (c,d) show lasing in the P- and S-flatbands, respectively.

In this work, we take a complementary perspective and ask whether band-structure engineering via orbital mixing can be used to generate quasi-1D line modes that lase along individual lines of a two-dimensional array, thus offering a route to densely packed independent lasing channels on a single chip.

Building on these foundations, the thesis explores two independent but complementary directions. This thesis focuses on two main themes: (1) conducting an experimental investigation into the effect of interference between external drives and lattice modes to study directional transport and non-linear localization in semiconductor micropillars arranged in a 1D chain and (2) Band-structure engineering by combining micropillars of different sizes to realize a Lieb sp lattice that combine different orbital modes, whose eigenmodes form quasi-1D line states. This allows for lasing in one-dimensional lines within the two-dimensional lattice. The investigation in this thesis aims to deepen the understanding of how external pumping, band engineering, and non-Hermitian physics shape light transport, non-linear localization and to have exotic lasing modes in driven-dissipative photonic lattices. The thesis is structured as follows:

Chapter 1 introduces exciton–polaritons in semiconductor microcavities and summarizes their key physical properties as hybrid light–matter quasiparticles. The microcavity platform, excitation schemes and driven–dissipative models used to describe them are briefly presented. The chapter ends by describing how structures from planar cavities to coupled micropillar arrays are fabricated, and how mode hybridization in these arrays leads to polaritonic bands.

Chapter 2 presents the experimental realization of a one-dimensional driven–dissipative lattice of coupled microresonators and shows how interference between external coherent drives and lattice eigenmodes can be used to control light transport. By tuning the relative phase of multiple resonant drives, optical switching and tunable directional propagation at the micron scale are demonstrated. An analytical model and numerical simulations are developed alongside the experiments to interpret and quantify these interference effects.

Chapter 3 investigates interference-induced localization in a one-dimensional driven–dissipative photonic lattice. In the linear regime under phase-controlled

driving, spatially confined steady states are characterized across the band. By increasing pump power, interference conditions for localization are altered at detunings where the linear system remains delocalized. Using a coupled exciton–photon model, the respective roles of saturation nonlinearity, disorder, and stray light that alters localization are unraveled.

Chapter 4 focuses on a driven–dissipative Lieb sp photonic lattice, where suitably band engineered orbital modes give rise to $1D$ line eigenmodes embedded in a $2D$ array. Using spatially structured non-resonant pumping, selective line lasing is demonstrated, and cross-shaped excitation produces two orthogonal line lasers that lock in energy, phase, and polarization. Finally, the interferometric measurements used to characterize this phase and polarization locking are outlined.

Chapter 5 develops a driven–dissipative lattice-lasing model to identify the minimal ingredients required for phase locking between orthogonal line modes and shows how orbital coupling and non-linear reservoir effects shape this locking behavior.

1

DRIVEN-DISSIPATIVE LATTICES OF COUPLED MICROPILLARS

The goal of this chapter is to introduce a unique composite particle that emerges in semiconductor environments when confined optical fields interact strongly with electronic resonances in low-dimensional systems. These quasiparticles, known as exciton polaritons, are formed through the interaction of photons trapped in engineered optical resonators and excitons confined within quantum wells. Unlike bare photons or excitons, polaritons embody characteristics of both light and matter. The photonic component facilitates low effective mass, rapid propagation, and strong spatial confinement governed by the geometry of the cavity, whereas the excitonic component introduces nonlinear interactions mediated by Coulomb forces. The finite lifetime of polaritons makes them dissipative, and it allows direct optical access to their energy, momentum, and spatial profiles through emitted photons, making them useful for experimental probing. The chapter begins by outlining the semiconductor microcavity system consisting of Distributed Bragg Reflectors and embedded quantum wells for the creation of polaritons. The experimental setup and excitation scheme are then presented in detail along with two distinct theoretical models to describe driven-dissipative polaritons based on the excitation schemes. Subsequently, the etching techniques employed in C2N to fabricate structures ranging from planar cavities to a single micropillar to extended pillar chains are explained. This transition from isolated to coupled pillars sets the stage for introducing how mode hybridization in coupled micropillar arrays leads to the formation of polaritonic bands.

1.1 Microcavity Exciton Polaritons

The pursuit of engineered quantum systems capable of simulating complex many-body Hamiltonians dates back to Feynman's foundational idea that controllable quantum platforms could emulate physical systems beyond the reach of classical computation [61]. This concept led to the field of quantum simulation, which has since evolved through platforms such as cold atoms in optical lattices [62], trapped ions [63], superconducting circuits [64], and photonic systems [65, 66]. These simulators enable exploration of key models in condensed matter physics, including the Bose Hubbard model, topological phases, and non-equilibrium dynamics.

Amid these developments, semiconductor microcavities emerged in the early 1990s as a solid-state architecture where strong coupling between quantum well excitons and cavity photons could be achieved. This was first demonstrated experimentally by Weisbuch et al. in a GaAs/AlAs cavity structure, where the clear observation of vacuum Rabi splitting marked the formation of new eigenstates termed exciton polaritons [39]. These quasiparticles inherit a low effective mass and spatial coherence from their photonic component, and nonlinear interaction from their excitonic part, offering a unique hybrid platform for optical analog simulation.

Unlike atomic systems, microcavities offer intrinsic scalability, lithographic patterning, and fast optical access, making them a suitable candidate for engineering artificial Hamiltonians in a driven-dissipative system [44, 67–69]. Therefore, from the perspective of photonic simulators, semiconductor microcavities with embedded quantum wells represent a versatile and tunable platform for exploring complex Hamiltonians. The ability to tailor both the spatial geometry and the underlying light–matter coupling opens the door to analog simulation of a broad class of Hamiltonians, from condensed matter models to out-of-equilibrium dynamics.

1.1.1 DBR Microcavity

With the motivation for Hamiltonian simulation established, it is essential to understand how semiconductor microcavities are engineered to create polaritons. Semiconductor microcavities are typically realized as planar Fabry–Pérot resonators, where light is confined between two high-reflectivity mirrors known as Distributed Bragg reflectors (DBRs), which rely on engineered interference rather than metallic reflection [70, 71]. A DBR is composed of multiple alternating layers with different refractive indices such as $Al_{0.10}Ga_{0.90}As$ ($n_1 = 3.44$) and $Al_{0.95}Ga_{0.05}As$ ($n_2 = 2.95$), as shown in Fig. 1.1(a). Each layer is chosen to have the same optical thickness, such that $n_1 L_1 = n_2 L_2 = \lambda_c/4$, where λ_c is the central Bragg wavelength at which maximum reflectivity is achieved. When light propagates through this

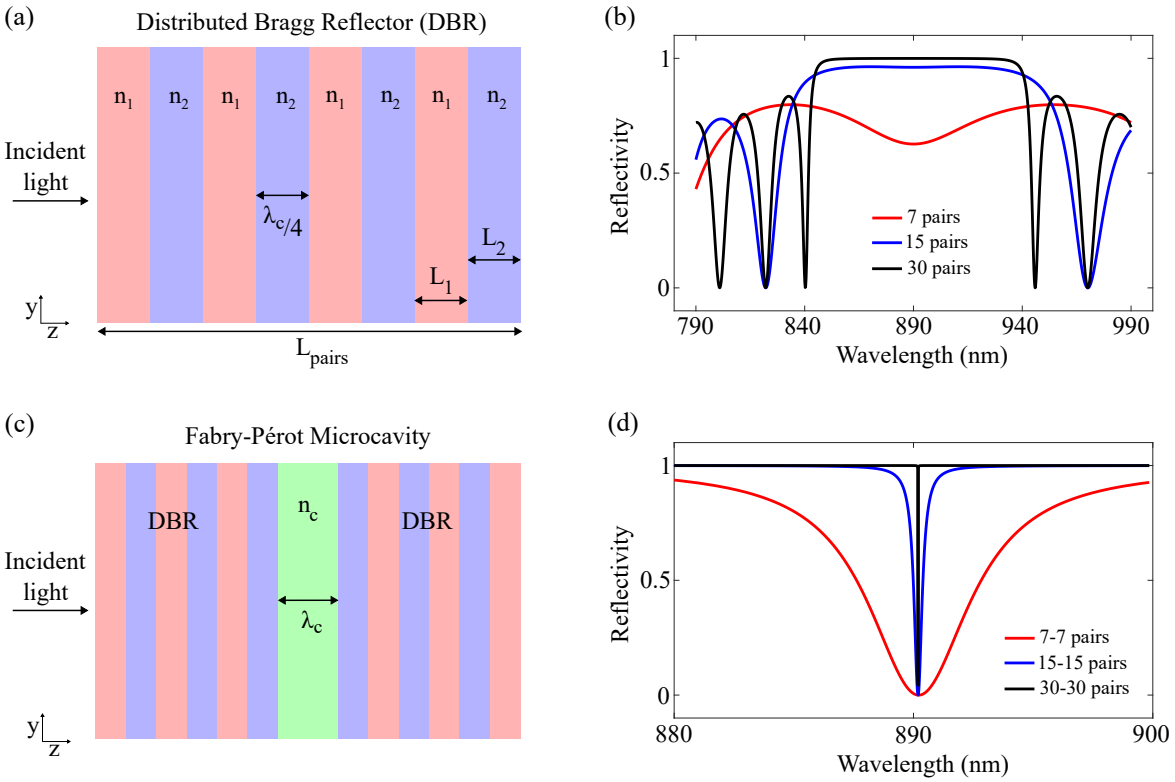

Figure 1.1: (a) Schematics of a single DBR composed of alternating layers of different refractive index (n_1, n_2) - $Al_{0.10}Ga_{0.90}As$ and $Al_{0.95}Ga_{0.05}As$, respectively. (b) Reflectivity spectrum of a DBR structure in 1.1(a), where a photonic stop band appears centered around 890nm. (c) Schematics of a planar microcavity formed by introducing a GaAs spacer (n_c) between two identical DBRs. (d) Reflectivity spectrum of the Fabry-Pérot Microcavity structure in 1(c), where a sharp dip within the stop band corresponding to the cavity mode.

multilayer structure, it undergoes multiple partial reflections at each interface as a result of refractive index mismatches. The transfer matrix method is a well established tool for modeling such systems, as it systematically computes the net reflectivity by accounting for interference and propagation effects across all layers [70, 72]. For normal incidence, the reflectivity (R) of a DBR consisting of L_{pairs} can be approximated by [70]:

$$R(\lambda_c) \approx 1 - 4 \cdot \frac{n_{\text{ext}}}{n_{\text{sub}}} \left(\frac{n_1}{n_2} \right)^{2L_{\text{pairs}}} \tag{1.1}$$

where n_{ext} and n_{sub} are the refractive index of the external medium and the substrate on which the structure is grown. As the number of pairs increases, the stop band becomes more pronounced and flatter, with reflectivity approaching unity. This trend is illustrated in Fig. 1.1(b), which shows the reflectivity spectra for DBRs with 7, 15, and 30 pairs. The reflectivity near $\lambda_c = 890\,\text{nm}$ (Bragg wavelength) reaches approximately 0.996, as confirmed by the transfer matrix simulation shown in panel (b).

Building on the reflective properties of DBRs, a planar microcavity can be constructed by placing a GaAs layer spacer with refractive index $n_c = 3.55$ and thickness of $L_c = 0.251\,\mu$m, chosen to satisfy the half-wavelength resonance condition $n_c \cdot L_c \approx \lambda_c/2$ as shown in Fig. 1.1(c). This enables the formation of a standing wave within the cavity, resulting in a resonant optical mode. In the reflectivity spectrum, this mode appears as a sharp dip within the high reflectivity stop band, signaling resonant transmission through the cavity. As shown in Fig. 1.1(d), the linewidth of the reflectivity dip is strongly influenced by the number of DBR pairs. In particular, the heterostructure with 30–30 pairs exhibits an extremely narrow dip compared to those with 7–7 and 15–15 pairs, reflecting a significantly higher cavity finesse. This high reflectivity leads to photon lifetimes on the order of tens of picoseconds and supports quality factors reaching $Q \sim 10^5$, depending on material absorption and fabrication precision.

An interesting thing to note is that because of confinement, the in-plane dispersion of the cavity mode acquires a parabolic dispersion near the resonance minimum, allowing for an effective photon mass several orders of magnitude smaller than that of free electrons ($m_c \sim 10^{-5} m_e$). Thus, the Fabry–Pérot microcavity provides a versatile passive platform for shaping the optical field. To enable active functionalities such as lasing or light–matter coupling, one can incorporate quantum well excitons, which will be the focus of the next section.

1.1.2 Confined excitons in Quantum wells

In semiconductor materials, the dimensional confinement in one, two, or all three spatial dimensions that form dots, wires, or quantum wells, respectively, offers a powerful approach to tailoring the properties of excitons (bound states of electrons and holes) [73–75]. In this work, we focus on the case of a quantum well, where the confinement of excitons is only along the growth direction (z), while it can move freely within the x–y plane perpendicular to z.

A quantum well is fabricated by sandwiching a thin semiconductor layer between two barrier layers with a wider band gap, as illustrated in Fig. 1.2. The resulting band discontinuities create potential wells that confine charge carriers (electrons and holes) along the growth direction. This confinement achieved through band gap engineering tailors the conduction and valence band offsets at the material interfaces. In this work, the quantum well is a $In_{0.05}Ga_{0.95}As$, a III–V semiconductor of refractive index 3.51 with a bandgap narrower than that of GaAs at an operating wavelength around 850nm (for more information, see Table A.1 and A.2 of the Appendix A). $\chi_e(z)$ ($\chi_h(z)$) denotes the ground-state solution of the one-dimensional Schrödinger equation for an electron (or a hole) in the potential

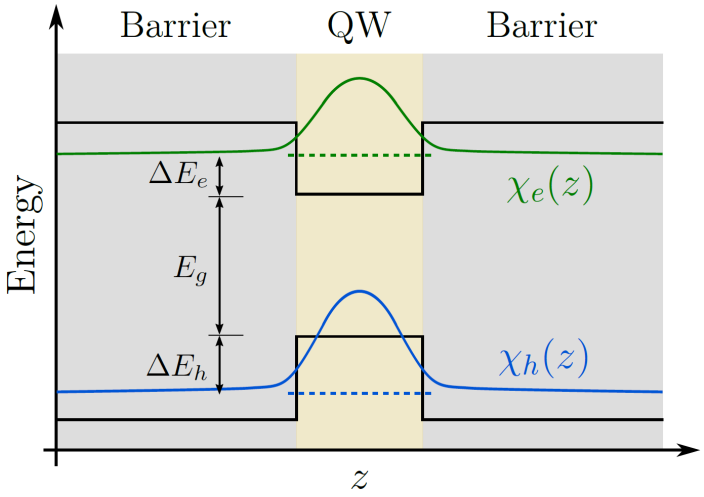

Figure 1.2: Schematic illustration of a quantum well embedded between two higher bandgap semiconductor layers. The potential barriers are shown as solid black lines, while the envelope wavefunctions of the confined electron and hole states, χ_e and χ_h, are also depicted. Taken from [76].

$V_e(z)$ ($V_h(z)$) in Fig. 1.2, with the corresponding confinement energy E_e (E_h) for the electron (hole). The energy dispersion for a confined exciton is given as [77]:

$$E_{\mathrm{X,n}}(\vec{k}) = E_g + E_e + E_h + \frac{\hbar^2|\vec{K}|^2}{2m_{x,eff}} - \frac{R^*}{\left(n-\frac{1}{2}\right)^2} \tag{1.2}$$

where E_g is the band gap energy, $\vec{K}$ is the wave-vector of the center of mass motion, n is the principal quantum number and $m_{\mathrm{x,eff}} = m_{e,\mathrm{eff}} + m_{h,\mathrm{eff}}$ represents the total exciton effective mass, given by the sum of the effective electron and hole masses. $R^* = \frac{\hbar^2}{2\mu a_B^2}$ is the Rydberg energy of the exciton, representing its binding energy ($\sim 5meV$), and $a_B = \frac{4\pi\varepsilon\hbar^2}{\mu e^2}$ is the exciton Bohr radius ($\sim 15nm$) where ε is the dielectric constant and μ is the reduced mass. As a consequence of the reduced dimensionality, confinement in the quantum well leads to a binding energy that is no longer the usual $1/n^2$ dependence as in the bulk but instead scales as $1/(n-1/2)^2$. Theoretical studies also predict how this binding energy evolves as a function of the width of the quantum well [78]. Given that the binding energy is only a few meV, the excitons are thermally ionized at room temperature, unless the thermal energy is much smaller than the binding energy ($k_BT \ll R^*$). For this reason, excitonic resonances in the quantum well studied here are observable only at cryogenic temperatures. Therefore, all experiments reported in this thesis were carried out with the samples cooled to a low temperature.

1.1.3 Light matter interaction

The two building blocks, cavity photons and quantum well excitons have been introduced, and now we proceed to combine them by embedding the quantum well within the optical microcavity enabling the study of light–matter interaction. The excitons described in the previous section can be electrically injected or optically generated. It is important that the energy and the total angular momentum are conserved along the growth axis (z-axis), which is the direction where the system breaks the translational symmetry. As a result, only excitonic states that preserve the angular momentum of the incident photon along z can participate in the interaction. In typical III–V quantum wells, at the Γ point, the conduction band consists primarily of s-like ($l = 0$) Bloch states. Because $l = 0$, these states do not contribute an orbital angular momentum, so conduction electrons are characterized solely by their spin projection $m_s = \pm\frac{1}{2}$. In contrast, the valence band is built from p-like ($l = 1$) Bloch states. Here, strong spin–orbit coupling combines orbital ($l = 1$) and spin ($s = \frac{1}{2}$) to yield total angular momentum $j = 3/2$, with the heavy-hole subband corresponding to projections $m_j = \pm\frac{3}{2}$. When a conduction electron ($m_s = \pm\frac{1}{2}$) binds to a heavy hole ($m_j = \mp\frac{3}{2}$), the resulting excitons possess total angular momentum projections of $J_z = \pm 1$ and ± 2. According to the electric dipole selection rule, only optical transitions with a change in the angular momentum projection of $\Delta m = m_s(\pm\frac{1}{2}) + m_j(\mp\frac{3}{2}) = \mp 1$ are allowed, because left-handed (σ^-) and right-handed (σ^+) circularly polarized photons carry spin angular momentum projections of -1 and $+1$, respectively. Therefore, $J_z = \pm 1$ excitons are coupled directly to the $\sigma^\pm$ photons [39, 73, 79] and are referred to as "bright" excitons. In contrast, excitons with $J_z = 0, \pm 2, ...$ remain uncoupled to the photon and are called dark excitons. Linearly polarized light, being a coherent superposition of σ^+ and σ^-, can therefore excite both $J_z = +1$ and $J_z = -1$ states simultaneously. Therefore, the angular momentum selection rule fundamentally constrains the subset of excitons that contribute to light–matter interaction in the cavity.

When an exciton is created in a quantum well, it decays through several pathways. In a radiative process, the exciton recombines and emits a photon [80]. In a non-radiative process, its energy may instead be dissipated through phonon interactions, defects, or Auger scattering [81]. When the quantum well is embedded in an optical microcavity, the radiative decay is modified by the presence of confined cavity modes [82], which can be described using the semi-classical Lorentz oscillator model [83]. To enhance light–matter coupling, the quantum well is typically placed at the antinodes of the cavity electric field, where the photon mode has maximum amplitude, thus maximizing the overlap between the excitonic dipole and the cavity field [39]. Under these conditions, the system can enter the weak or strong coupling regime, depending on the exciton photon coupling strength and their respective decay rates [84].

1.1.3.1 *Weak coupling*

In the weak coupling regime, the exciton acts as a passive emitter, and there is no coherent energy exchange between exciton and photon, retaining their individual identities with no formation of new eigenstates. The system behaves like a lossy emitter in a resonant cavity, and its spectroscopic signature shows a broadened or slightly deformed cavity resonance without leading to mode splitting. In this regime, radiative decay is enhanced as a result of the Purcell effect, which increases the spontaneous emission rate in the cavity mode [85–87]. However, non-radiative decay such as defect recombination or phonon scattering still contribute to the exciton linewidth and act as competing loss mechanisms. Weak coupling occurs when the light–matter coupling strength (g) is smaller than the average of the cavity and exciton linewidths: $g < \frac{1}{4}(\gamma_{\text{cav}} + \gamma_{\text{exc}})$, where γ_{cav} and γ_{exc} are the linewidths of the cavity and exciton, respectively.

1.1.3.2 *Strong coupling*

In contrast, the strong coupling regime emerges when the exciton and photon exchange energy coherently multiple times before either decays. This coherent interaction leads to the formation of hybrid quasiparticles called exciton polaritons, which are new eigenstates of the coupled system. The hallmark of strong coupling is the appearance of Rabi splitting in the reflectivity or transmission spectrum, where the single cavity resonance is split into two branches: the upper and lower polariton modes. Strong coupling is achieved when the coupling strength exceeds the dissipation rates: $g > \frac{1}{4}(\gamma_{\text{cav}} + \gamma_{\text{exc}})$.

The concept of strong coupling between light and matter in solid-state systems traces back to the foundational work by Hopfield in the late 1950s [88], where the theoretical framework for exciton-photon hybridization was first developed. This theoretical idea was brought into experimental reality in the early 1990s, led by [39] revealing a Rabi splitting in the optical spectrum that served as conclusive evidence of coherent exciton–photon hybridization in semiconductor microcavities containing quantum wells.

1.1.4 Hopfield coefficients

To describe the coherent interaction between cavity photons and excitons in the strong coupling regime, it is convenient to adopt a second-quantized formalism. In this framework, both excitons and photons are treated as bosonic quasiparticles, with corresponding creation and annihilation operators. Specifically, $a^\dagger_{\mathbf{k}}, a_{\mathbf{k}}$ denote the creation and annihilation operators for photons, while $b^\dagger_{\mathbf{k}}, b_{\mathbf{k}}$ represent those for excitons, where $\mathbf{k}$ is the in-plane wavevector of the excitonic transition and quasi-resonant optical mode. These operators satisfy the bosonic commutation re-

lations: $[a_{\mathbf{k}}, a^{\dagger}_{\mathbf{k}'}] = \delta_{\mathbf{k},\mathbf{k}'}$ and $[b_{\mathbf{k}}, b^{\dagger}_{\mathbf{k}'}] = \delta_{\mathbf{k},\mathbf{k}'}$. This formalism allows us to write the Hamiltonian for the coupled exciton-photon system as [67, 88]:

$$H_k = E_X(\mathbf{k})\, b^{\dagger}_{\mathbf{k}} b_{\mathbf{k}} + E_C(\mathbf{k})\, a^{\dagger}_{\mathbf{k}} a_{\mathbf{k}} + \underbrace{\frac{\hbar\Omega_R}{2}\left(a^{\dagger}_{\mathbf{k}} b_{\mathbf{k}} + b^{\dagger}_{\mathbf{k}} a_{\mathbf{k}}\right)}_{\text{light–matter interaction}} \tag{1.3}$$

$$E_C(\mathbf{k}) \simeq \frac{\hbar^2 \mathbf{k}^2}{2m_c} + \frac{\hbar c \pi}{L_{eff} n_c} \tag{1.4}$$

$$\Omega_R = 2g = 2\sqrt{\frac{2c\Gamma_0}{n_c L_{\text{eff}}}} \propto \sqrt{\frac{f_{\text{osc}}}{L_{\text{eff}}}} \tag{1.5}$$

Here Γ_0 is the radiative lifetime of excitons at $\mathbf{k} = 0$ in free space, and f_{osc} is the exciton oscillator strength that can be calculated using a perturbative approach [89]. The effective length (L_{eff}) incorporates the penetration depth of the electromagnetic field into the DBRs such that $L_{\text{eff}} = L_c + L_{\text{DBR}}$. $E_X(\mathbf{k})$ is the exciton dispersion 1.2, $E_C(\mathbf{k})$ is the cavity dispersion 1.4, $\hbar\Omega_R$ is the Rabi splitting 1.5 and $\frac{\hbar\Omega_R}{2}$ is the coupling strength (g). The coupling strength, characterized by Rabi splitting ($\hbar\Omega_R$), is mainly influenced by two key factors. Firstly, it depends on the excitonic oscillator strength, which is significantly enhanced in quantum wells because of the strong spatial overlap between electron and hole wavefunctions. This enhancement results from the quantum confinement effect, which increases the probability of recombination and strengthens the exciton-photon interaction [90]. Secondly, the coupling is also determined by the effective optical mode volume (the spatial region where the electromagnetic field is confined). In semiconductor microcavities, this volume is exceptionally small, thus amplifying the field intensity and improving the coupling efficiency [86].

These combined effects enable the realization of a strong coupling regime even with a single quantum well. For example, typical Rabi splittings of approximately 3.5 meV have been observed in GaAs-based microcavities with one embedded quantum well [39]. Higher values can be achieved in materials with larger exciton binding energies and oscillator strengths, such as CdTe and GaN, which make them particularly attractive for room temperature polaritonic devices [91].

The Hamiltonian in 1.3 can be diagonalized as follows:

$$H_{\mathbf{k}} = E_{\text{UP}}(k)\, p^{(\text{UP})\dagger}_{\mathbf{k}}\, p^{(\text{UP})}_{\mathbf{k}} + E_{\text{LP}}(k)\, p^{(\text{LP})\dagger}_{\mathbf{k}}\, p^{(\text{LP})}_{\mathbf{k}} \tag{1.6}$$

where the operators p_k are obtained from the photon and exciton operators a_k and b_k via a unitary transformation:

$$\begin{pmatrix} p^{(\text{LP})}_{\mathbf{k}} \\ p^{(\text{UP})}_{\mathbf{k}} \end{pmatrix} = \begin{pmatrix} -C_k & X_k \\ X_k & C_k \end{pmatrix} \begin{pmatrix} a_k \\ b_k \end{pmatrix} \tag{1.7}$$

The Hopfield coefficients X_k and C_k are defined by:

$$X_k^2 = \frac{1}{2}\left(1 + \frac{\delta_k}{\sqrt{4\hbar^2\Omega_R^2 + \delta_k^2}}\right) \tag{1.8}$$

$$C_k^2 = \frac{1}{2}\left(1 - \frac{\delta_k}{\sqrt{4\hbar^2\Omega_R^2 + \delta_k^2}}\right) \tag{1.9}$$

where the cavity-exciton detuning (δ_k) is defined as $\delta_k = E_C(k) - E_X(k)$. The Hopfield coefficients satisfy the normalization condition: $X_k^2 + C_k^2 = 1$. The new eigenstates of the coupled exciton-photon system are referred to as exciton-polaritons, and they form two distinct energy branches: the upper polariton (UP) and the lower polariton (LP), as defined by the transformation in 1.7. These polaritons are superpositions of photon and exciton states, characterized by a photonic fraction C_k^2 and an excitonic fraction X_k^2.

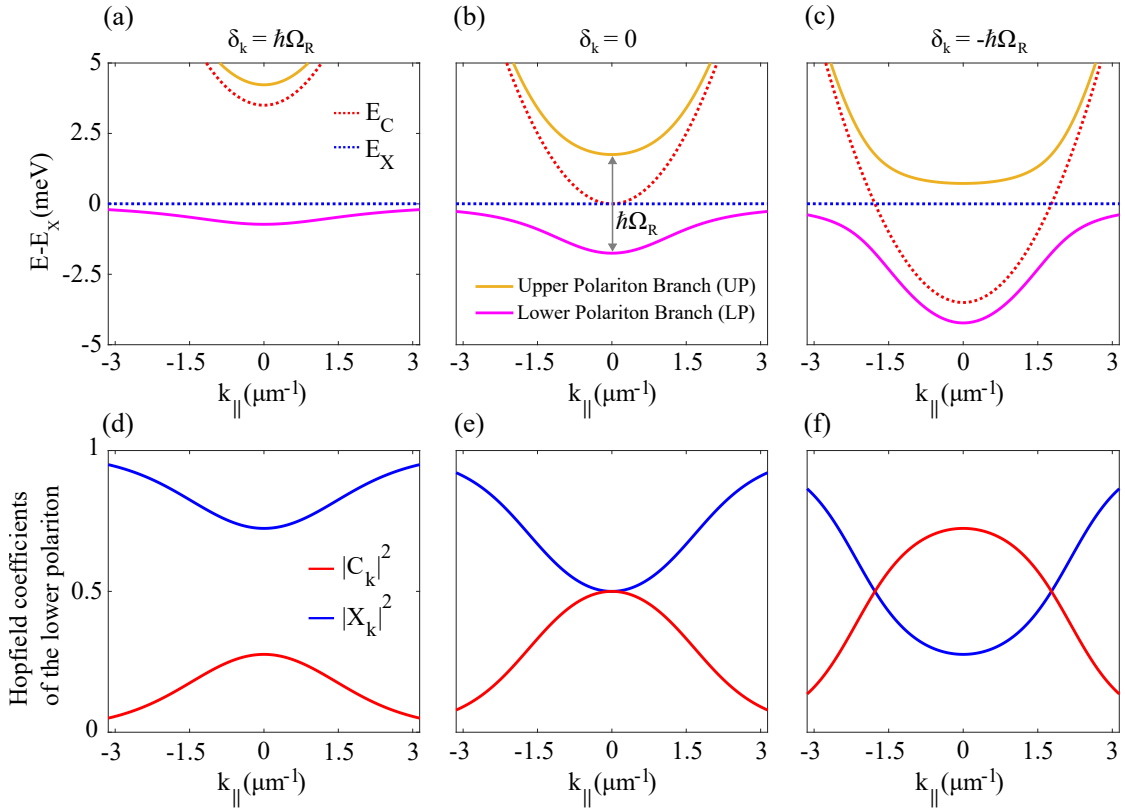

Figure 1.3: Panels (a)-(c) show the upper (E_{UP}) and lower (E_{LP}) polariton branches as a function of the in-plane wavevector k for three different cavity-exciton detunings: (a) $\delta(0) = +\hbar\Omega_R$, (b) $\delta(0) = 0$, and (c) $\delta(0) = -\hbar\Omega_R$. The uncoupled cavity-photon and quantum well exciton dispersions are shown as colored dashed lines for reference. Panels (d)-(f) present the Hopfield coefficients, $|X_k|^2$ (exciton fraction) and $|C_k|^2$ (photon fraction), plotted as functions of k with solid lines for the lower polariton branch.

The energy dispersion relations for the upper and lower polaritons are given by:

$$E_{\mathrm{UP,LP}}(k) = \frac{1}{2}\left(E_{\mathrm{X}}(k) + E_{\mathrm{C}}(k) \pm \sqrt{\delta_k^2 + \hbar^2\Omega_R^2}\right) \tag{1.10}$$

The upper (+) and lower (−) signs in 1.10 refer to the upper polariton (UP) and lower polariton (LP) branches, respectively. Fig. 1.3 presents the polariton energy dispersions and corresponding Hopfield coefficients for three different photon-exciton detunings at $k_{||} = 0$: $\delta(0) = +\hbar\Omega_R$ (positive detuning), 0 (zero detuning), and $-\hbar\Omega_R$ (negative detuning), where $\hbar\Omega_R$ = 3.5 meV. The bare-photon and exciton dispersions are plotted as dashed reference curves in the Fig. 1.3 panels (a)-(c). Because of the large difference between the effective masses of photons and excitons, the exciton dispersion appears nearly flat, while the cavity mode exhibits parabolic curvature. At zero detuning, a clear anti-crossing between the UP and LP branches is observed near $k = 0$, with an energy gap equal to the Rabi splitting $\hbar\Omega_R$, as shown in Fig. 1.3(b). This anti-crossing is the hallmark of the strong coupling regime.

The lower polariton (LP) branch exhibits a mixed photonic-excitonic character that evolves as a function of both in-plane momentum and detuning. For example, in the case of negative detuning, LP is more photon-like, whereas in positive detuning, it becomes more exciton-like. As k increases (i.e., for large in-plane wavevector), polaritons become increasingly excitonic across all detunings due to the rising energy of the cavity mode. These trends are directly visualized in the Hopfield coefficient plots of Fig. 1.3 panels (d)-(f), where $|X_k|^2$ and $|C_k|^2$ quantify the exciton and photon contributions to the polariton wavefunction.

1.1.4.1 *Polaritons Characteristics*

Polaritons exhibit a unique combination of light and matter properties, with two of their most critical characteristics being their effective mass and finite lifetime. These two characteristics are connected to the exciton-photon mixing encoded in the Hopfield coefficients. At near zero in-plane wavevector ($k_{||} \approx 0$), the lower polariton branch (LP) acquires an effective mass that results from the hybridization of the bare exciton and photon modes. This mass can be expressed in terms of the Hopfield coefficients $|X_0|^2$ and $|C_0|^2$ as [86]:

$$\frac{1}{m_{\mathrm{LP}}} = \frac{|X_0|^2}{m_{x,eff}} + \frac{|C_0|^2}{m_{\mathrm{c}}} \tag{1.11}$$

where $m_{x,eff}$ and m_{c} denote the effective masses of the exciton and cavity photon, respectively. Since $m_{x,eff} \gg m_{\mathrm{c}}$, the effective mass of LP can be approximated by the photonic fraction. This results in a polariton mass up to four orders of magnitude lighter than the electron rest mass, which is critical to observe phenomena such as Bose–Einstein condensation and ballistic propagation [92, 93].

Polaritons are not indefinitely stable due to photon leakage from the cavity mirrors and exciton recombination; they have finite lifetimes, typically in the range of 1–100 ps. These lifetimes are manifested as a homogeneous linewidth in the energy spectrum. To capture this effect, the exciton and photon modes are described by complex energies, written as $E_X - i\gamma_X$ and $E_C - i\gamma_C$, where γ_X and γ_C represent their respective linewidths. The system enters the strong coupling regime only when the coupling strength (g) exceeds the individual photon and exciton decay rates [77]. By transforming the complex energies into the polariton basis, two well-defined eigenstates are obtained, each characterized by its own linewidth:

$$\gamma_{LP}(k) = |X_k|^2 \gamma_X(k) + |C_k|^2 \gamma_C(k) \tag{1.12}$$

$$\gamma_{UP}(k) = |C_k|^2 \gamma_X(k) + |X_k|^2 \gamma_C(k) \tag{1.13}$$

where γ_X and γ_C are the linewidths of the exciton and photon modes, respectively. Since $\gamma_X \ll \gamma_C$, the LP linewidth is primarily determined by the photon losses, and the lifetime scales as $\tau_{LP} \approx \tau_C/|C_0|^2$. This short lifetime makes polaritons an inherently out-of-equilibrium quasiparticle that continuously decays and must be optically replenished. Interestingly, this decay provides a major experimental advantage. Because photons escape the cavity conserving both energy and in-plane momentum, each emitted photon uniquely maps to a polariton state inside the cavity. Therefore, one can directly access the polariton dispersion via angle- and energy-resolved emission, meanwhile spatially resolved measurements allow for reconstruction of the polariton wavefunction in real space.

Exciton-polariton systems exhibit a variety of interaction mechanisms originating primarily from their excitonic component. These include polariton–polariton [41], exciton–exciton [40], and mixed exciton–polariton interactions [94], all of which are predominantly repulsive and are mediated by the Coulombic interaction. A key feature of these interactions is their strong dependence on the pseudospin configuration. Polaritons with parallel pseudospin can interact resonantly, while those with antiparallel pseudospin interact more weakly, often requiring virtual transitions through dark exciton states. The strength of these interactions can be actively driven by an external optical driving field. Depending on whether the system is excited resonantly or non-resonantly, the interaction landscape and resulting nonlinear behavior can differ significantly.

1.2 Mean Field Description of Driven-Dissipative Polaritons

In the previous section, the exciton–polariton system was described using the second-quantized formalism. We now transition to a mean-field approach, which is more suitable for modeling macroscopic polariton dynamics, particularly in the

presence of interactions and nonlinear effects. This approximation is valid when polariton modes are macroscopically occupied, allowing coherent behavior to dominate over quantum fluctuations. Therefore, quantum operators can be replaced by classical complex fields. The mean-field framework captures the essential features of driven-dissipative polariton systems, including interactions, decay, and external pumping. In what follows, two different formulations are introduced: exciton–photon coupled model, relevant for resonant excitation pumping for directional transport in the Chapter 2 and nonlinear localization in the Chapter 3, and a reduced Gross–Pitaevskii equation to describe non-resonant pumping for line lasing in Chapter 5.

1.2.1 Two Component Model: Coupled Exciton-Photon

1.2.1.1 *Resonant excitation*

In the case of resonant pumping, a monochromatic pump laser is coherently driven at or near the energy of a particular polariton branch. Under this condition, the polariton population remains coherent with the external driving field. This dynamics can be captured by a coupled two-component model, where the exciton and photon fields are treated explicitly and evolve under coherent coupling, external drive, and dissipation. The two-coupled Hamiltonian for the exciton-photon system is given as:

$$H(\mathbf{k}) = \begin{bmatrix} E_X & \frac{\hbar\Omega_R}{2} \\ \frac{\hbar\Omega_R}{2} & E_C(k_{||}) \end{bmatrix} \tag{1.14}$$

where E_X is the exciton dispersion, $\hbar\Omega_R$ is the Rabi splitting, and $E_C(k_{||})$ is the dispersion of the cavity photon as a function of the in-plane wavevector $k_{||}$. The exciton dispersion is assumed to be independent of $\mathbf{k}$ due to the large effective mass of the exciton compared to that of the photon. The time evolution of the coupled exciton–photon system is governed by the following differential equations without taking spin into account [95, 96]:

$$i\hbar\frac{d}{dt}\psi_C = \left(\delta_C - i\frac{\gamma_C}{2}\right)\psi_C + \left(\frac{\hbar\Omega_R}{2} - \frac{1}{2}g_{sat}|\psi_X|^2\right)\psi_X + i\sqrt{\frac{\gamma_C}{2}}E_{inc} \tag{1.15}$$

$$i\hbar\frac{d}{dt}\psi_X = \left(\delta_X - i\frac{\gamma_X}{2} + g_X|\psi_X|^2\right)\psi_X + \left(\frac{\hbar\Omega_R}{2} - g_{sat}|\psi_X|^2\right)\psi_C - \frac{1}{2}g_{sat}\psi_X^2\psi_C^* \tag{1.16}$$

The pump field E_{inc} is typically modeled as a Gaussian in space and time as:

$$E_{\text{inc}}(x,t) = E_0 \exp\left(-\frac{x^2}{2\sigma^2}\right)\exp\left(-i\frac{E_p t}{\hbar}\right) \tag{1.17}$$

where E_0 is the peak amplitude, σ is the spatial width of the Gaussian beam, and E_p is the pump energy. The parameters used in the coupled equations for the cavity photon field (ψ_C) in 1.15 and the exciton field (ψ_X) in 1.16 are defined as follows: The photon detuning is given by $\delta_C = E_p - E_C^0$, and the exciton detuning is $\delta_X = E_p - E_X$, E_C^0 is the bare cavity photon energy at $\mathbf{k} = 0$, and E_X is the exciton energy. The decay rates of the photon and exciton are denoted by γ_C and γ_X, respectively. The term $\hbar\Omega_R$ represents the Rabi splitting between the exciton and photon modes. The nonlinear interaction between excitons is described by the term $g_X|\psi_X|^2\psi_X$, where g_X is the exciton-exciton interaction strength. The coefficient g_{sat} accounts for exciton saturation effects because phase space filling limits the interaction strength as exciton density increases [95], reflecting the composite nature of excitons as bound states of two fermions.

1.2.2 Gross Pitaevskii Formalism

1.2.2.1 *Non Resonant excitation*

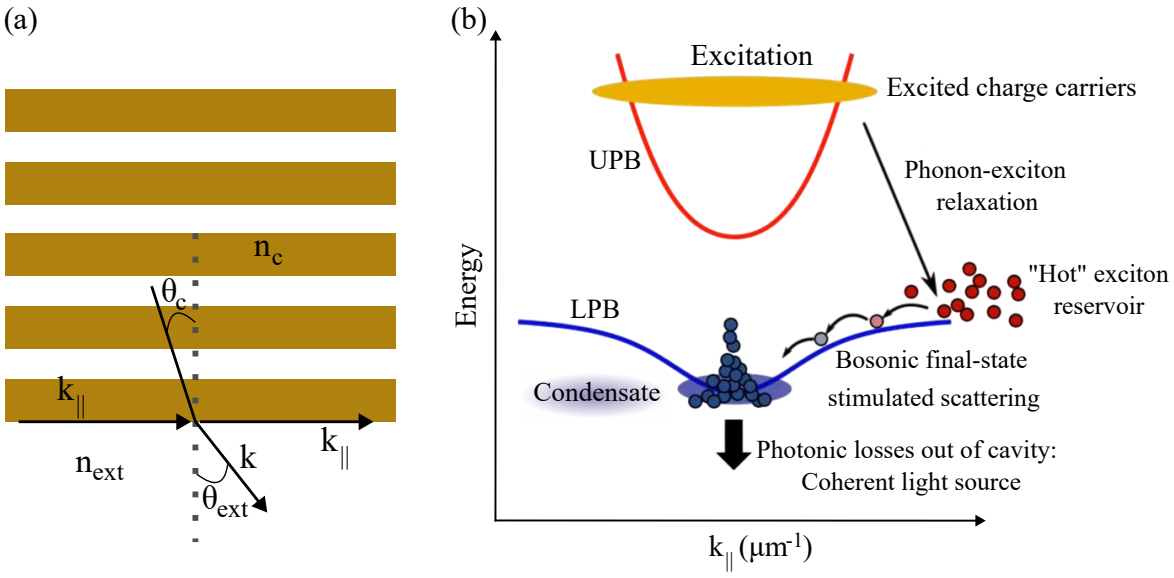

Figure 1.4: (a) Schematic of photon emission from the cavity, illustrating that the in-plane momentum is conserved during the emission process. Taken from [97]. (b) Illustration of the non-resonant excitation scheme.

In non-resonant excitation, the pump laser is tuned far above the polariton resonances, typically by about 100 meV or more, injecting high-energy photons well above the semiconductor bandgap. This results in the generation of free electron-hole pairs, which rapidly relax through phonon emission. A fraction of these carriers bind to form quantum well excitons, which can be either radiative (able to couple with cavity photons) and form polaritons or non-radiative, contributing to the formation of a long-lived exciton reservoir. This exciton reservoir interacts with polaritons through their excitonic component, giving rise to a nonlinear blue-

shift of the polariton energy [98]. A schematic representation of the exciton reservoir and its interaction with the polariton field is shown in Fig. 1.4(b). When the particle density becomes significant, this interaction modifies the system dynamics and must be included in the model. The polariton field can then be described using a Gross-Pitaevskii (GP) equation for the lower polariton field $\psi(\vec{r},t)$, coupled to a rate equation describing the evolution of the exciton reservoir density $n_R(\vec{r},t)$. The equations take the form [96, 99]:

$$i\hbar\frac{\partial\psi(\vec{r},t)}{\partial t} = \left[-\frac{\hbar^2\nabla^2}{2m_p} + V_{\text{ext}}(\vec{r}) + g|\psi|^2 + g_R n_R(\vec{r},t) + iRn_R(\vec{r},t) - i\frac{\gamma_c}{2}\right]\psi(\vec{r},t) \tag{1.18}$$

$$\frac{\partial n_R(\vec{r},t)}{\partial t} = P(\vec{r}) - \left(\gamma_R + R|\psi(\vec{r},t)|^2\right)n_R(\vec{r},t) \tag{1.19}$$

where m_p is the effective polariton mass, $V_{\text{ext}}(\vec{r})$ is an external potential, g is the polariton-polariton interaction strength, g_R quantifies the polariton exciton reservoir interaction and γ_c is the photon decay rate from the cavity. The term Rn_R describes stimulated scattering from the reservoir into the condensate, while $P(\vec{r})$ is the spatially dependent pump rate and γ_R accounts for losses within the reservoir.

The emitted photons carry direct information about the energy, in-plane momentum, and spatial distribution of the polariton population. Due to conservation of momentum, the in-plane wavevector ($k_{\|}$) of a polariton is related to the angle (θ_{ext}) at which the corresponding photon exits the microcavity via the relation: $|k_{\|}| = \frac{n_{ext}E}{\hbar c}\sin(\theta_{ext})$ as depicted in Fig. 1.4(a), where E is the photon energy and c is the speed of light in vacuum. As a result, the angular emission profile encodes the polariton momentum distribution. The experimental setup used to perform these measurements is described in the following section.

1.3 Experimental setup

The photoluminescence experiments presented in this thesis work are conducted using a setup schematically illustrated in Fig. 1.5. The sample is mounted on the closed-cycle He cryostat, fixed to a motorized translation stage that enables precise alignment with the optical path. The cooling is provided by a continuous flow of liquid helium, stabilizing the temperature at 4K. To prevent thermal losses, the cryostat chamber is kept under high vacuum (10^{-7} - 10^{-6} mbar). This cryogenic environment allows stable, low-temperature measurements for the optical excitation and detection schemes described in the following section.

All optical measurements in this work employ a continuous-wave single-mode M Squared Ti:Sapphire laser, tunable between 750 and 880nm with a linewidth

below $10MHz$ ($40neV$), whose output is coupled into a polarization-maintaining single-mode fiber to ensure a clean Gaussian spatial profile. Power control is achieved using a half-wave plate ($\lambda/2$) and a polarizing beam splitter (PBS), allowing for adjustment of the incident laser power while maintaining a well-defined polarization. The beam is then focused on the sample using an aspherical lens with a focal length of $8mm$ (f_{exc}) and a numerical aperture of 0.5 as illustrated in Fig. 1.5(a). All photoluminescence (PL) measurements in this work are performed in a transmission geometry, detecting the emission from the side opposite to the excitation. At the operating wavelengths, the GaAs substrate is transparent, allowing the emitted photons to pass through without significant attenuation.

Two imaging configurations are used for PL measurements on the collection side: Near field (real-space imaging) as shown in Fig. 1.5(b) and Far field (fourier-space imaging) as shown in Fig. 1.5(c). In both cases, the collected PL is magnified through a telescope system composed of the collection lens (f_{col}) and additional lenses (f_1, f_2 and f_4) before entering the spectrometer. The entrance slit of the spectrometer, in combination with a scanning lens (f_4) mounted on a motorized translation stage, allows spatial selection of a vertical slice of the emission. The emission spectrum is recorded using a Teledyne Princeton Instrument spectrometer with a spectral resolution of $0.06nm$ (around $100\mu eV$). The slit width of 32.5 μm corresponds to $\sim$ 0.3 μm in the sample after accounting for the optical magnification [100]. This selected slice is then spectrally dispersed by the $1200g/mm$ grating spectrometer and projected onto a CCD camera.

Angle-resolved photoluminescence measurements are performed using a modified detection path designed to image the momentum space of the emitted photons, as depicted in Fig. 1.5(c). Photons emitted from the sample with a given angle (θ) focus on a single point in the back focal plane (Fourier plane) of the collection lens (f_{col}). This plane provides a direct mapping of the in-plane polariton momentum, effectively reconstructing the two-dimensional momentum distribution of the system. To record this information, an additional Fourier lens (f_3) is placed so that the optical system composed of f_1-f_2 and f_3-f_4 images the Fourier plane of the collection lens (f_{col}) onto the spectrometer entrance slit. Once the two-dimensional Fourier image is projected onto the slit, any desired momentum-space direction can be selected by translating the scanning lens (f_4) perpendicular to the slit. The selected cut through momentum space is then spectrally dispersed by the monochromator and detected on a CCD, producing E–k dispersion relations. Scanning across different momentum-space directions, it is possible to reconstruct a complete three-dimensional intensity signal $I(k_x, k_y, E)$, where each point contains the intensity of the emission at a given in-plane momentum (k_x, k_y) and energy E thus characterizing both the polariton dispersion and the corresponding intensity distribution in the momentum space.

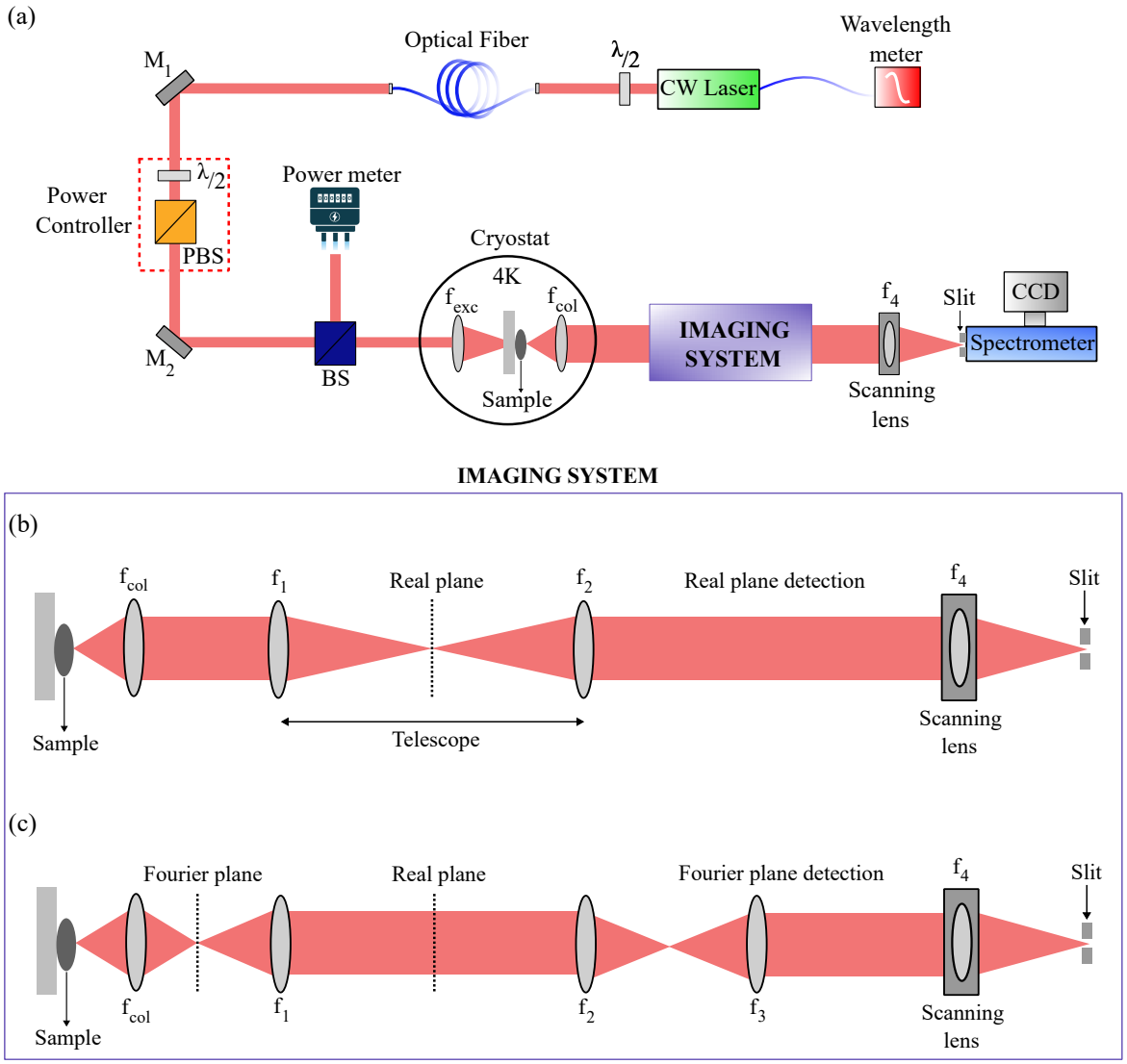

Figure 1.5: (a) Schematic of the experimental setup. The two lower panels illustrate the possible configurations of the imaging system. (b) Near-field (Real-space) imaging, where the sample plane is imaged onto the camera. (c) Far-field (Fourier-space) imaging, where the angular distribution of the emitted light is imaged onto the camera. The red line represents the optical beam path. Abbreviations: $\lambda/2$ - half-wave plate, PBS - polarizing beam splitter, BS -beam splitter. Lenses used in the setup have the following focal lengths: $f_{col} = 8$ mm, $f_1 = 300$ mm, $f_2 = 150$ mm, $f_3 = 200$ mm (Fourier lens), and $f_4 = 500$ mm.

1.4 Engineering Polariton Hamiltonians

In the previous section, the fundamental characteristics of microcavity polaritons were outlined together with their unique advantages as hybrid light–matter quasiparticles. One of the most powerful capabilities of these systems lies in the controlled engineering of their potential energy landscape. By introducing lateral confinement, it becomes possible to steer the polariton propagation, tune their interaction strength, and modify their band dispersion. This control enables the creation of customized environments, from periodic lattices to localized traps, and

even platforms for implementing synthetic gauge fields, greatly broadening the scope of accessible physical phenomena. A comprehensive overview of the various confinement strategies reported in the literature can be found in [101]. In what follows, a general discussion of excitonic and photonic potentials acting on the matter-like and light-like components of the polariton is presented before focusing on the specific approach adopted to fabricate the sample in our team.

1.4.1 Excitonic confining potentials

Excitonic confinement is achieved by locally modifying the exciton resonance energy $E_X(\mathbf{r})$ within the quantum well plane, thus creating an effective potential acting on the matter fraction of the polariton, $V_X(\mathbf{r}) \simeq |X|^2 \Delta E_X(\mathbf{r})$, where $|X|^2$ is the excitonic Hopfield coefficient. Because excitons are much more spatially localized than photons, such confinement can produce sharp lateral features that enhance nonlinear effects (scaling of the polariton–polariton interaction strength with the excitonic fraction) [102]. Some of the techniques for implementing excitonic confinement are the following;

• **Strain-induced confinement**: A static excitonic potential can be created through strain-induced band gap shifts [103]. The application of local mechanical stress modifies the semiconductor lattice constant and hence the quantum well bandgap, shifting E_X in a controlled region. Regions with $\Delta E_X > 0$ (locally higher exciton energy) act as repulsive barriers, while $\Delta E_X < 0$ form attractive traps that localize polaritons. While effective, this approach is static and subject to inhomogeneous broadening from strain non-uniformities.

• **Surface acoustic waves (SAWs)**: SAWs were initially employed in the group of P. Santos, offering the possibility to engineer polariton lattices. SAWs periodically strain the crystal lattice as they propagate, producing a spatially and temporally varying shift in E_X. This creates a moving periodic potential for polaritons with a tunable amplitude and wavelength determined by acoustic drive [104, 105]. A single SAW transducer generates a one-dimensional ($1D$) periodic potential along its propagation direction. Launching two SAWs in opposite directions along the same axis produces a stationary spatial modulation, while driving SAWs along two perpendicular directions creates a two-dimensional ($2D$) grid of potential wells and barriers allowing lattice confinement in both spatial dimensions [106]. Unlike static strain patterns, SAW-induced potentials can be switched on and off and their propagation direction can be controlled. When combined with optical pumping, they allow the creation of moving lattices and reconfigurable traps for polaritons. However, achievable confinement depths are typically limited by the maximum strain that can be applied without degrading the crystal.

• **Optically induced exciton reservoir**: A fully reconfigurable excitonic potential can be created by optically injecting a localized exciton reservoir using a non-resonant pump beam, as discussed in Eqns. 1.18 and 1.19. The repulsive exciton-exciton interaction induces a local blueshift of the exciton resonance, forming a tunable potential barrier for polaritons. This approach has been used to confine polaritons in $1D$ configurations [107] and also in $2D$ lattices [108–110] by shaping the pump beam profile with spatial light modulators (SLM) to generate complex potential landscapes. This all-optical method offers high flexibility but non-resonant excitation populates multiple polariton states within the pumped area, which can limit coherence and mode selectivity.

1.4.2 Photonic confining potentials

Photonic confinement is realized by creating spatial variations in the cavity photon resonance energy $E_C(\mathbf{r})$, thus producing an effective potential that acts on the photonic fraction of the polariton, $V_C(\mathbf{r}) \simeq |C|^2 \Delta E_C(\mathbf{r})$, where $|C|^2$ is the photonic Hopfield coefficient. This can be achieved by locally modifying the dielectric environment or the optical path length of the cavity. Compared with excitonic confinement, the smoother spatial profile of photonic potentials stems from the delocalized nature of the photon mode. Some of the techniques for implementing photonic confinement are the following;

• **Patterned metallic deposition**: Depositing a thin metallic layer (e.g. Au/Ti) with a defined pattern on the top surface modifies the electromagnetic boundary conditions at the cavity interface. This alters the local cavity mode energy by $0.1 - 1$ meV, sufficient to form effective potentials for polaritons. The technique is straightforward and has been used to realize 1D and 2D lattices such as triangular [111] and kagome geometries [112]. Its main limitation is the relatively shallow potential depth, which constrains the degree of confinement achievable.

• **Etch-and-overgrowth**: In this approach, the bottom DBR, the cavity spacer, and the quantum wells are first grown. The cavity spacer is then selectively thinned only in its upper portion, leaving the quantum wells untouched to preserve their excitonic optical quality. This partial etching locally changes the cavity length, shifting the cavity mode energy by a few meV. Afterward, the top DBR is regrown, creating a "mesa" that can act as $0D$ polariton traps [113–115]. Initially used for isolated traps, this technique has since been extended to create $2D$ lattices by patterning the etch geometry [116].

• **Post-growth etching**: Fabrication approach in which the microcavity is patterned after complete epitaxial growth.

- *Full etch down to the substrate*: This approach removes material from the top DBR through the cavity spacer and the lower DBR, stopping at the substrate.

The resulting high refractive index contrast between the vacuum and the semiconductor cavity provides photonic confinement. In its original demonstrations, it was implemented in the weak-coupling regime [117].

- *Partial top-mirror etch*: In this less invasive variant, only the upper DBR is etched, leaving the quantum wells intact and avoids exciton linewidth degradation from surface recombination. Despite the reduced modification depth, the index contrast is sufficient to confine the photonic mode, enabling the fabrication of extended polariton lattices in the strong-coupling regime [43, 118].

In summary, potential landscapes can be implemented through several routes; in what follows, we concentrate on the C2N variant of post-growth etching to the substrate, which underpins all samples used in this thesis.

1.4.3 C2N Etching technique - planar cavity to micropillar

The GaAs-based microcavity samples mentioned in this thesis are fabricated at the Centre de Nanosciences et de Nanotechnologies (C2N) in Palaiseau. The design, growth and etching of the sample are coordinated by J. Bloch and S. Ravets. The heterostructures are grown layer by layer by the group of Aristide Lemaître using molecular beam epitaxy (MBE) on an epitaxially ready GaAs substrate. This process yields a planar cavity consisting of a cavity spacer with embedded quantum wells sandwiched between top and bottom distributed Bragg reflectors (DBRs). During growth, the molecular beams emitted in the MBE system are not perfectly parallel (non-collimated). As a result, the incident flux varies slightly across the wafer surface, leading to a gradual variation in the thickness of the deposited layer. This thickness gradient, often referred to as a wedge, translates into a spatial shift of the cavity resonance energy across the sample. Controlled substrate rotation can reduce this gradient, allowing precise tuning of the photon–exciton detuning range available on a single wafer. After growth, room-temperature reflectivity mapping is performed to determine the spatial variation of the cavity mode energy by the group of J. Bloch and S. Ravets.

Transformation from a planar cavity to laterally confined structures is carried out by the C2N nanofabrication team (Luc le Gratiet, Abdelmounaim Harouri, and Isabelle Sagnes). First, the desired pattern is defined by spin-coating a resist and writing it via electron-beam lithography. The pattern is then transferred to the GaAs microcavity stack using inductively coupled plasma (ICP) dry etching. In the post-growth full-etch process employed here, material is removed from the top DBR through the cavity spacer and the bottom DBR, stopping at the GaAs substrate. This deep etch isolates the etched regions from their surround-

ings, providing strong in-plane photonic confinement via total internal reflection at the air-semiconductor interface. By properly designing the lithographic mask, a wide range of geometries can be realized, including single micropillars ($0D$) [119], coupled pillar chains ($1D$) [120], and periodic pillar arrays ($2D$ lattices) [43, 121].

1.5 Micropillar as an artificial photonic atom

In many areas of condensed matter and quantum optics, the underlying physics can be captured by relatively simple model Hamiltonians, such as tight binding lattices, Jaynes-Cummings interactions, or driven-dissipative Bose-Hubbard models [67, 122]. To study such Hamiltonians in a controlled setting, one requires a platform with well-defined, tunable discrete modes and controllable coupling between them. With the fabrication methods developed at C2N, semiconductor micropillars offer precisely these capabilities. By etching a planar microcavity into a pillar geometry, the photonic mode becomes laterally confined, yielding a discrete set of polariton states with energies and symmetries determined by the shape and size of the pillar [123]. These quantized modes act as the "orbitals" of the Hamiltonian, with lithographic control that enables the coupling between the pillars to emulate hopping and the resulting hybridization of orbitals [43, 124]. Understanding the properties of an isolated (single) micropillar and a coupled (dimer) pillar forms the essential foundation for building more complex coupled lattices aimed at Hamiltonian engineering.

1.5.1 Single micropillar

The optical confinement in a micropillar microcavity is three-dimensional: Along the growth axis, the mode is quantized vertically by the cavity spacer bounded by the distributed Bragg reflectors (DBRs). In the plane of the cavity, the lateral confinement is imposed by the refractive index contrast between the etched pillar and the surrounding air, quantizing the in-plane polariton momentum (k_x and k_y) to take discrete values. Figure 1.6(a) shows a scanning electron microscope (SEM) image of a cylindrical micropillar fabricated by deep etching from a planar microcavity heterostructure. The resulting transverse confinement can be modeled as a particle of effective mass m_{eff} in a two-dimensional cylindrical potential well of radius R. In the paraxial approximation, the Helmholtz equation reduces to a Schrödinger-like form with eigenfunctions given by cylindrical Bessel functions $J_\ell(r)$, characterized by radial and angular momentum quantum numbers n and ℓ. The corresponding allowed eigenenergies are given by

$$E_{n,\ell} = \frac{\hbar^2 z_{\ell,n}^2}{2m_{\text{eff}}R^2} \tag{1.20}$$

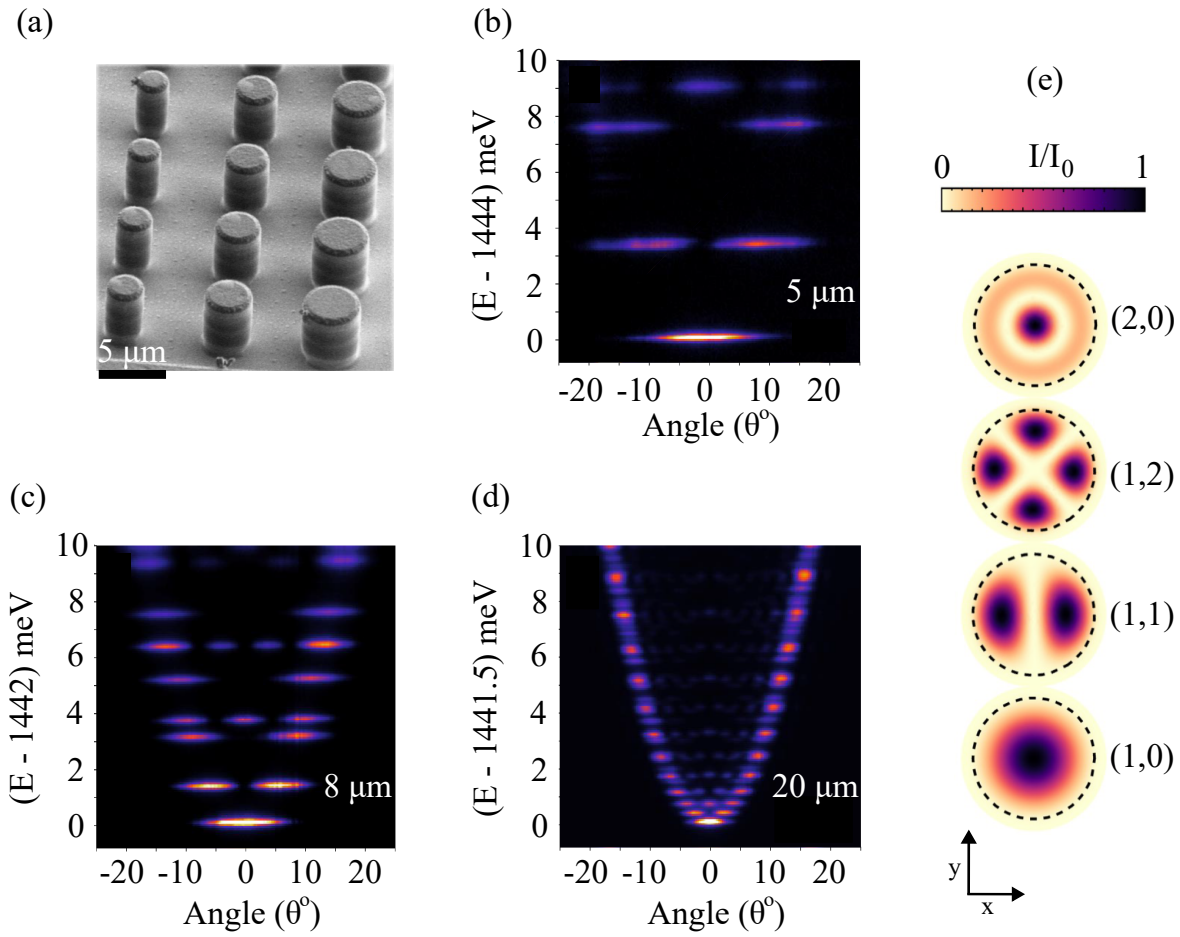

Figure 1.6: (a) SEM image of cylindrical microcavities (micropillars) fabricated by deep etching from a planar microcavity heterostructure. Taken from [125]. (b-d) Energy spectrum of three different cylindrical micropillar diameters: $5\mu m$, $8\mu m$ and $20\mu m$, respectively. Taken from [97]. (e) Calculated intensity profiles of the micropillar eigenmodes, indexed by their principal (n) and angular (l) quantum numbers. The lowest-energy state corresponds to the s orbital like mode, followed by the first excited p orbital like mode, with higher-order modes occupying progressively larger energies. Taken from [125].

where $z_{\ell,n}$ are the roots of the cylindrical Bessel function of order ℓ, defined by the condition $J_\ell(z_{\ell,n}) = 0$. The lowest energy mode $(n = 1, l = 0)$ is s-like, while the first excited pair $(n = 1, l = \pm 1)$ is p-like with orthogonal lobes. Fig. 1.6(e) shows the calculated intensity profiles for these eigenmodes, illustrating the mode symmetries predicted by the model. In chapter 4, we will focus primarily on these two lowest energy states to do band engineering.

Under non-resonant excitation, these confined modes appear as discrete spectral modes in the photoluminescence (PL) spectrum as shown in Fig. 1.6(b–d) for pillars of three different diameters ($5\mu m$, $8\mu m$ and $20\mu m$) respectively, revealing the s mode and the p_x mode confirming the interpretation of Eqn. 1.20. As the diameter decreases, the energy spacing between modes increases, reflecting stronger lateral confinement and the scaling of the energy levels ($1/R^2$). This tunability of

the photonic eigenmodes by adjusting the pillar size provides a powerful means of engineering orbital energies. In particular, as will be discussed in Chapter 4, this approach allows different orbital states to be brought into resonance and hybridized. For this reason, micropillars can be viewed as "artificial atoms" whose quantized photonic orbitals can be tuned lithographically. However, it should be emphasized that this confinement acts only on the photonic part of the polariton: the excitonic component remains unaffected because the exciton Bohr radius is much smaller than the lateral dimensions of the pillars.

1.5.2 Diatomic molecule - coupled micropillar

Having established the discrete orbital structure of a single micropillar, the next step is to consider what happens when two identical pillars are brought close enough for their photonic wavefunctions to overlap. In this configuration as shown in the SEM image of Fig. 1.7(a), often referred to as a micropillar dimer, the individual s- and p-like orbitals of each pillar with radius R and center to center distance a hybridize through evanescent coupling across the etched gap. When the separation is small enough, their confined modes overlap such that the eigenstates of the system can no longer be described as those of isolated pillars.

In the micropillar systems, as discussed previously, the relevant orbital states are localized around discrete sites. The tight-binding model provides a framework for describing such systems: starting from a set of localized orbitals $\{|m\rangle\}$ to including both the onsite energies and the possibility of tunneling between sites. Although the exact solution of the coupled two-well problem is not analytical, it can be well approximated by constructing linear combinations of the single-pillar eigenstates. For example, focusing on the lowest orbital case, only the s-modes of each pillar ($|s,A\rangle$ and $|s,B\rangle$) are retained. These hybridize to form new eigenstates given by the symmetric (bonding) $|\psi_+\rangle$ and antisymmetric (antibonding) superpositions $|\psi_-\rangle$ as $|\psi_\pm\rangle = \frac{1}{\sqrt{2}}\Big(|s,A\rangle \pm |s,B\rangle\Big)$, with the corresponding energies $E = E_0 \pm t$. Here, E_0 is the isolated pillar energy and t denotes the coupling strength (hopping amplitude) between the two pillars, which is determined by the spatial overlap of their wavefunctions and can be tuned lithographically via the inter-pillar spacing. This simple two-site system is captured by a tight binding Hamiltonian as;

$$H = \begin{bmatrix} E_0 & -t \\ -t & E_0 \end{bmatrix} \tag{1.21}$$

Fig. 1.7(b) shows the spatially resolved photoluminescence spectrum of a micropillar dimer, each of radius ($R = 2\mu m$) and center to center separation ($a = 3.6\mu m$) as referenced in [125]. The spectrum consists of discrete modes, with the two lowest energy peaks corresponding to the hybridization of the fundamental

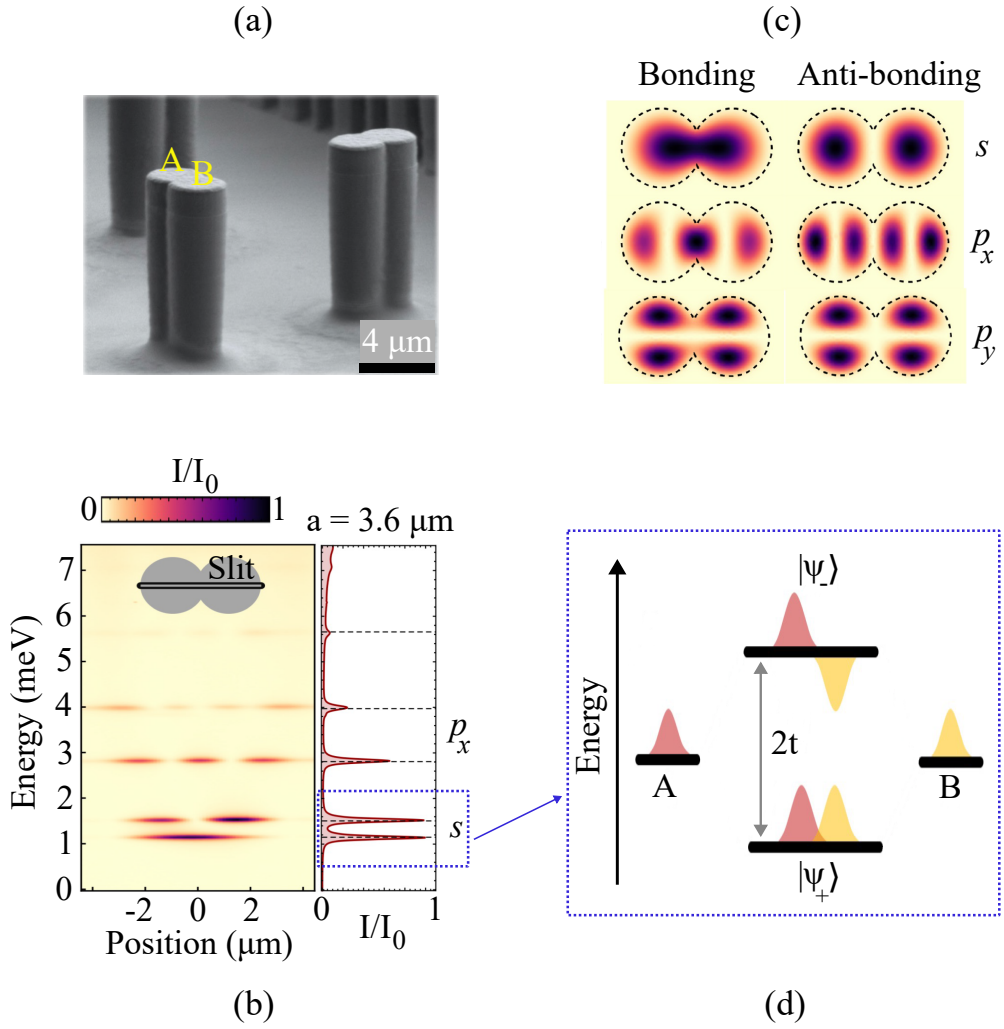

Figure 1.7: (a) SEM image showing two etched micropillars brought close together to form a dimer. (b) Spatially resolved photoluminescence spectrum measured from a dimer with radius $R = 2\mu m$ and separation $a = 3.6\mu m$. The inset indicates the position of the spectrometer slit, and the dashed line corresponds to finite-element calculations for the same geometry. (c) Intensity patterns of the six lowest eigenmodes for $a = 3.6\mu m$, arranged according to their single-pillar orbital type and their bonding or antibonding character. (d) Sketch illustrating how the two lowest s-modes hybridize into bonding ($|\psi_+\rangle$) and antibonding ($|\psi_-\rangle$) states. All the images in this figure was taken from [125].

s orbitals of the individual pillars. Their splitting directly reflects the coupling strength (t) of the inter-pillars A and B. This is illustrated in Fig. 1.7(d), where the bonding ($|\psi_+\rangle$) and antibonding ($|\psi_-\rangle$) states arise from the bare s mode of the A and B sites. The spatial intensity distributions of the six lowest eigenmodes are presented in Fig. 1.7(c) in which the modes are classified according to single-pillar orbital symmetry (s, p_x, p_y) and the hybridization character (bonding or antibonding), thus providing a direct experimental visualization of the orbital structure of the dimer. Together, Figure 1.7 shows that the micropillar dimer behaves as an optical analogue of a diatomic molecule, with well-defined molecular orbitals emerging from the hybridization of individual pillar modes.

A key feature to be observed is that the center-to-center distance a controls the coupling strength t: smaller separations increase the mode overlap and increase the bonding to the antibonding energy splitting, while larger separations decrease it [126]. The ability to control the coupling in dimers forms the basis for complex lattice Hamiltonians. For instance, when micropillars are arranged into a one-dimensional chain, the hybridization of neighboring orbitals leads to the emergence of bands, transitioning from artificial molecules to engineered lattices.

1.6 Tight binding model for lattices

The same approach can be extended to larger arrays of coupled pillars, where the Hamiltonian takes the general form

$$H = \sum_m E_0 \left|m\right\rangle \left\langle m\right| - \sum_{m,m'} \left(t_{m,m'} \left|m'\right\rangle \left\langle m\right| + \text{h.c.} \right) \tag{1.22}$$

where E_0 denotes the onsite energy of site m and $t_{m,m'}$ is the hopping amplitude from m to m'. In periodic structures, diagonalization of Eq. 1.22 yields energy bands, establishing a direct route from discrete localized sites to extended Bloch states in polariton lattices. The one-dimensional chain, discussed in the next subsection, is the simplest illustrative example of this general framework to show the emergence of bands.

1.6.1 Theoretical model of a 1D chain

To neglect edge effects, an infinite one-dimensional chain of equally spaced sites is considered at positions $x_m = ma$, where a is the lattice spacing as shown in Fig. 1.8(a). Each site hosts a single localized orbital $\left|m\right\rangle$ with onsite energy E_0, which defines the lattice geometry and the eigen state basis. The coupling between sites is included through a nearest-neighbour tunneling amplitude $t > 0$, representing orbital overlap between adjacent sites. Restricting to nearest-neighbour hopping is a standard approximation that captures the essential physics while keeping the model analytically tractable. With these assumptions, the tight-binding Hamiltonian is written as

$$H = \sum_m E_0 \left|m\right\rangle \left\langle m\right| - t \sum_m \left(\left|m{+}1\right\rangle \left\langle m\right| + \left|m\right\rangle \left\langle m{+}1\right| \right) \tag{1.23}$$

Since the chain is infinite and translationally invariant, we can look for stationary states of the form $\left|\psi\right\rangle = \sum_m \psi_m \left|m\right\rangle$, which satisfy the eigenvalue equation $H\left|\psi\right\rangle = E\left|\psi\right\rangle$. Expanding this on the eigen state basis and projecting onto $\left\langle m\right|$ yields a recurrence relation for the amplitudes ψ_m:

$$E\psi_m = E_0\psi_m - t\left(\psi_{m+1} + \psi_{m-1}\right) \tag{1.24}$$

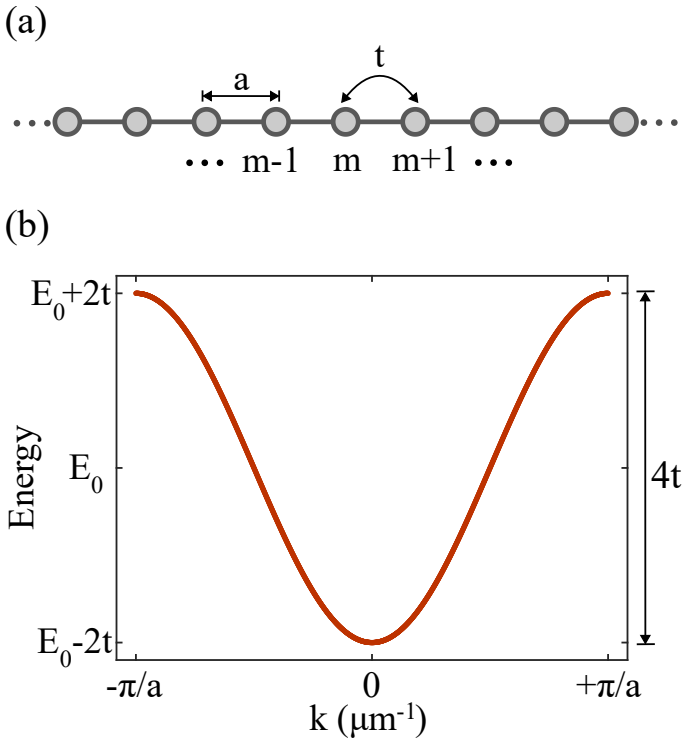

Figure 1.8: (a) Schematic of the one-dimensional tight-binding chain, where each site at position $x_m = ma$ hosts a localized orbital and hopping between nearest neighbours with amplitude t. (b) Corresponding dispersion relation for parameters $a = 1$, $E_0 = 0$, and $t = 1$, showing the cosine band $E(k) = E_0 - 2\cos(ka)$ extending from $-2t$ to $+2t$ with bandwidth of $4t$.

Equation 1.24 is the discrete Schrödinger equation for the one-dimensional lattice. It is a linear recurrence relation that couples each site amplitude with its nearest neighbours. Because the coefficients in Eq. 1.24 are independent of m, the equation is translation-invariant. This suggests trying an exponential ansatz, $\psi_m = \lambda^m$, where $\lambda \neq 0$ which substitutes the unknown sequence $\{\psi_m\}$ by the powers of a single complex parameter λ. Inserting this ansatz into Eq. 1.24 gives the characteristic equation

$$t\lambda^2 - (E_0 - E)\lambda + t = 0, \tag{1.25}$$

which is quadratic in λ. The characteristic polynomial 1.25 determines the spatial behaviour of the eigenstates. For energies inside the band, $|E - E_0| < 2t$, the discriminant is negative and the two roots lie on the unit circle, $\lambda = e^{\pm i\theta}$, $\theta \in \mathbb{R}$. Such oscillatory solutions correspond to extended Bloch states. Substituting $\lambda = e^{i\theta}$ into Eq. 1.24 gives $E = E_0 - 2t\cos\theta$. The phase accumulated when hopping with one lattice spacing in the recurrence relation is θ. In Bloch form, the state amplitudes are written as $\psi_m \propto e^{ikm}$, so the phase per site step is precisely ka. Therefore, $\theta = ka$ leads to the dispersion relation of the infinite chain as plotted in Fig. 1.8(b) is given by

$$E(k) = E_0 - 2t\cos(ka); \qquad k \in \left[-\frac{\pi}{a}, \frac{\pi}{a}\right) \tag{1.26}$$

where the Brillouin-zone interval follows from lattice periodicity. The band extends from $E_{\min} = E_0 - 2t \quad (k = 0)$ to $E_{\max} = E_0 + 2t \quad (k = \pi/a)$ with a total bandwidth of $4t$, obtained by evaluating cosine at its extrema. The sign of the hopping amplitude t determines the location of the band minimum: for $t > 0$ the minimum is located at $k = 0$, while for $t < 0$ it shifts to $k = \pi/a$.

From the dispersion 1.26, the group velocity can be calculated as

$$v_g(k) = \frac{1}{\hbar}\frac{dE}{dk} = \frac{2ta}{\hbar}\sin(ka) \tag{1.27}$$

which governs the motion of wave packets along the chain. Near the band bottom ($k \approx 0$), a Taylor expansion $\cos(ka) \approx 1 - (ka)^2/2$ gives $E(k) \approx (E_0 - 2t) + t(ka)^2$ showing a parabolic dispersion. The corresponding effective mass is given by

$$m_{\text{eff}} = \left[\frac{1}{\hbar^2}\frac{d^2E}{dk^2}\right]^{-1}_{k=0} = \frac{\hbar^2}{2ta^2} \tag{1.28}$$

Thus, the lattice near its band minimum can be assigned to a continuum particle with effective mass m_{eff}. For energies outside the band ($|E - E_0| > 2t$), the characteristic equation 1.25 yields real reciprocal roots $\lambda_\pm$, one decaying and the other growing with m. These correspond to evanescent modes, which are relevant only near surfaces or defects in a finite lattice system. The onsite energy E_0 simply offsets the entire band and has no effect on velocities or effective mass, since only energy differences matter in this model.

1.7 Summary

In this chapter, we introduced the basic framework for exciton–polaritons in GaAs/DBR microcavities, where quantum wells provide the excitonic component and distributed Bragg reflectors confine the photonic mode, leading to the strong light–matter coupling described by the Hopfield model. Two different mean-field approaches were outlined: a coupled-mode model in which exciton and photon fields are treated explicitly but coupled through the Rabi interaction, and a Gross–Pitaevskii description in which the polariton is treated as a single effective field. We then described the experimental setup used for resonant and non-resonant excitation, as well as the fabrication of high quality samples at C2N via molecular beam epitaxy and post-growth etching. Having established the system, we examined polariton confinement in single micropillars, which behave as artificial atoms with discrete s- and p-like orbitals, and in dimers where mode hybridization yields bonding and antibonding states. Finally, we extended this picture to one-dimensional chains of coupled pillars, where the tight-binding formalism naturally explains the emergence of bands, setting the stage for engineering lattice Hamiltonians in the upcoming chapters.

2

DIRECTIONAL TRANSPORT IN A 1D DRIVEN-DISSIPATIVE LATTICE

In the previous chapter, we developed the theoretical description of a one-dimensional lattice and showed how their coupled modes give rise to band structures. In this chapter, we extend this framework to the experimental realization of a one-dimensional driven dissipative lattice of coupled microresonators, focusing on how interference between external coherent drives and the eigenmodes of the lattice can be exploited to manipulate light transport. By resonantly driving the lattice with a coherent field of controlled phase, one gains access to an additional degree of control, enabling precise manipulation of interference effects at micron scale. The goal of this chapter is to demonstrate how this relative phase of multiple external drives can be used to design light transport to realize optical switching and enforce tunable directional propagation within the lattice. In addition, we employ analytical derivation together with numerical simulations to gain a better understanding and to have a direct comparison of the interference effects observed experimentally.

2.1 Characterization of 1D lattice

Having established the theoretical framework for a one-dimensional lattice in the final section of Chapter 1, we now turn to their experimental characterization. In our experiment, the schematics of the sample as shown in Fig. 2.1 (a) consists of 31 micropillars with a diameter of 3 μm and a center-to-center separation of $a = 2.5\,\mu$m. The micropillars are laterally etched from a λ GaAs planar microcavity consisting of two distributed Bragg reflectors of 32 and 36 pairs of $\lambda/4$ layers of $Ga_{0.05}Al_{0.95}As/Ga_{0.90}Al_{0.10}As$, where λ is the design wavelength of the cavity at about 858nm. A single InGaAs quantum well is grown at the center of the cavity (details of the nominal growth parameters for the semiconductor microcavity can be found in the Table A.1 of Appendix A). At the cryogenic temperature of the experiments (5K), cavity photons and quantum well excitons enter the strong-coupling regime, giving rise to exciton polaritons with a measured Rabi splitting of 3.5 meV.

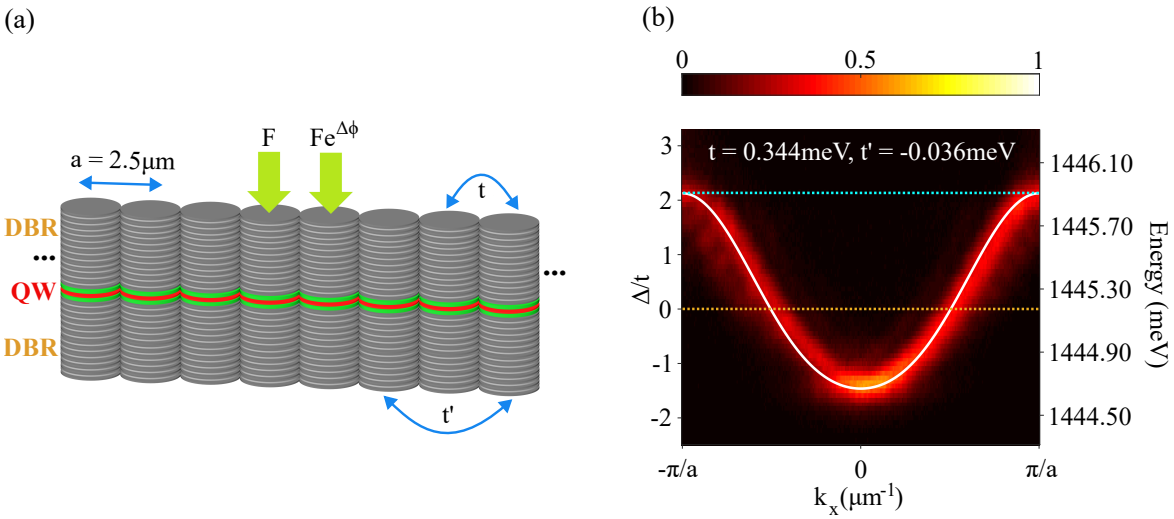

Figure 2.1: a) Schematic representation of the one-dimensional lattice consisting of 31 micropillars with a center-to-center separation of $a = 2.5\,\mu$m. The excitation spots are placed on adjacent pillars, with equal amplitudes F and a phase difference $\Delta\phi$. (b) Angle-resolved photoluminescence measurement of the 1D lattice with one pump spot, showing the energy bands as a function of the in-plane momentum k_x, with $\Delta = E_p - E_0$, where $E_0 = 1445.13$ meV. The white line represents the fitted two coupled exciton-photon model. The blue and orange dashed lines indicate the laser energy pumped at the top of the band ($\Delta/t = 1.87$) and at zero energy ($\Delta/t = 0$), respectively.

Each micropillar undergoes radiative losses to the environment and can be driven by an external laser, forming a driven-dissipative system [127]. The experiment is conducted in a transmission geometry with linearly polarized excitation parallel to the lattice direction. Photoluminescence or transmission measurements are performed filtering the linear polarization parallel to the lattice and using an imaging set-up with a lens of 0.5 numerical aperture and a CCD camera (Fig.

1.5). Angle-resolved photoluminescence with a non-resonant laser excitation at 1585.48 meV focused on a 1 μm spot (full width at half maximum) centered on top of a micropillar reveals the dispersion relation as displayed in Fig. 2.1 (b). The lowest band (s-band) follows a cosine-like dispersion, a typical feature of $1D$ lattices.

2.1.1 Numerical fitting - 1D lattice dispersion

The experimentally observed dispersion provides direct evidence for the formation of energy bands in the $1D$ chain lattice. To quantitatively analyze these bands, it is necessary to extract the underlying parameters of the system. Therefore, the measured band structure is fitted (with a white line in Fig. 2.1(b)) to a coupled Hamiltonian for the photon-exciton system:

$$H_k = \begin{bmatrix} E_X & \frac{\hbar\Omega_R}{2} \\ \frac{\hbar\Omega_R}{2} & E_C(k_x) \end{bmatrix} \tag{2.1}$$

where E_X represents the exciton energy, $\hbar\Omega_R$ is the Rabi splitting indicating the coupling strength between the photon and exciton modes, and $E_C(k_x)$ is the cavity photon energy. We assume that the exciton energy is independent of k due to its large mass of ~ 0.5 m_0 compared to the photon mass in the cavity of $\sim 10^{-5}$ m_0, with m_0 being the mass of free electron. The photon dispersion $E_C(k_x)$ of the lowest energy lattice band in Eq. 2.1 is obtained from a tight-binding description in which photons hop between adjacent micropillars is given by:

$$E_C(k_x) = E_C^0 - 2t\cos(k_x) - 2t'\cos(2k_x) \tag{2.2}$$

where t denotes the nearest-neighbor hopping, t' the next-nearest-neighbor hopping, and E_C^0 the bare photon energy of an individual micropillar. Equation 2.2 provides the minimal model for describing the cosine-like band observed in Fig. 2.1(b). The inclusion of t' accounts for an effective next-nearest-neighbor coupling mediated by hybridization between s and p modes, a coupling mechanism previously reported in photonic lattices and polaritonic systems [128].

To extract the photon dispersion parameters in Eq. 2.2 (E_C^0, t and t') from the experimentally measured band structure, we performed a numerical optimization using the `fmincon` function in MATLAB. This routine solves constrained optimization problems by minimizing a cost function, which in our case is the difference between the measured dispersion and the model of Eq. 2.1. By iterative adjustment of E_C^0, t and t', the algorithm finds the parameter set that best fits the experimental dispersion. In this fitting procedure, the exciton energy is fixed to $E_X = 1450.49$ meV and the Rabi splitting to $\hbar\Omega_R = 3.5$ meV, values independently obtained from the photoluminescence spectra. The optimization yields

$E_C^0 = 1445.68$ meV, $t = 0.35 \pm 0.01$ meV, and $t' = -0.03 \pm 0.01$ meV. We operate at a photon-exciton detuning of -5.45 meV, ensuring that the polaritons are 92% photonic and 8% excitonic.

2.2 Interference between external drives and lattice modes

The geometric arrangement of photonic lattices defines the periodic potential experienced by light waves and determines the allowed and forbidden frequency ranges [6, 7] while hopping or coupling interactions between neighboring sites allow for band structure engineering [44, 129–131]. Photonic band engineering therefore provides a route to shape dispersion relations in lossless photonic lattices [132, 133], however, its tunability remains inherently limited by the static nature of the system geometry. Beyond lattice design, interference effects arising from multiple hopping paths in the tight-binding limit and wave superposition can critically shape light transport in photonic lattices. One of the promising directions is to explore whether wave transport can be controlled through external driving and dissipation. In driven-dissipative systems, an external drive, typically a laser, injects light at a given frequency, phase and intensity distribution in the lattice. The system evolves toward a steady state dictated by the balance between drive, propagation in the lattice and losses. This situation offers a framework in which the response is determined not only by the lattice geometry but also by the driving conditions. In particular, when dissipative lattices are driven at resonance, the amplitude and phase of the external driving laser act as tunable parameters that, when tailored to interact with intrinsic lattice modes, can engineer novel transport mechanisms. In the following sections, we make use of this interference effect between multiple external drives and the intrinsic lattice modes to experimentally demonstrate optical switching and directional transport by resonantly exciting the lattice with a phase-controlled coherent field.

2.2.1 Optical switching

As a first step to study the interference between the eigenmodes of the lattice and multiple external drives, we pump two adjacent sites (m and $m+1$), as shown in Fig. 2.1(a), with equal amplitude at a photon energy corresponding to $\Delta/t = 1.87$ (top of the band). The laser detuning is defined by $\Delta = E_p - E_0$ such that $\Delta = 0$ is reached when the pump energy E_p is resonant with $E_0 = 1445.13$ meV, an energy reference close to the middle of the band. The phase difference $\Delta\phi$ between the two spots is experimentally set using a piezo-controlled mirror, which adjusts the path length of one beam relative to the other. When the two sites are pumped with zero phase difference ($\Delta\phi = 0$), the system exhibits a non-emissive ("OFF") response, as shown in Fig. 2.2(a): only a small amount of light is observed at the

pumped sites, while the rest of the lattice remains dark. The dark response of this driving profile can be understood by considering the spatial antisymmetric shape of the antibonding lattice eigenmode at the top of the band. The two laser spots excite coherently and in phase the top band mode at adjacent micropillars. Due to the phase difference of π between adjacent sites in the top band mode, the injected fields interfere destructively, resulting in a dark response. The residual transmission observed at the pumped sites (green arrows in Fig. 2.2(a)) arises from slight misalignment of the excitation beams.

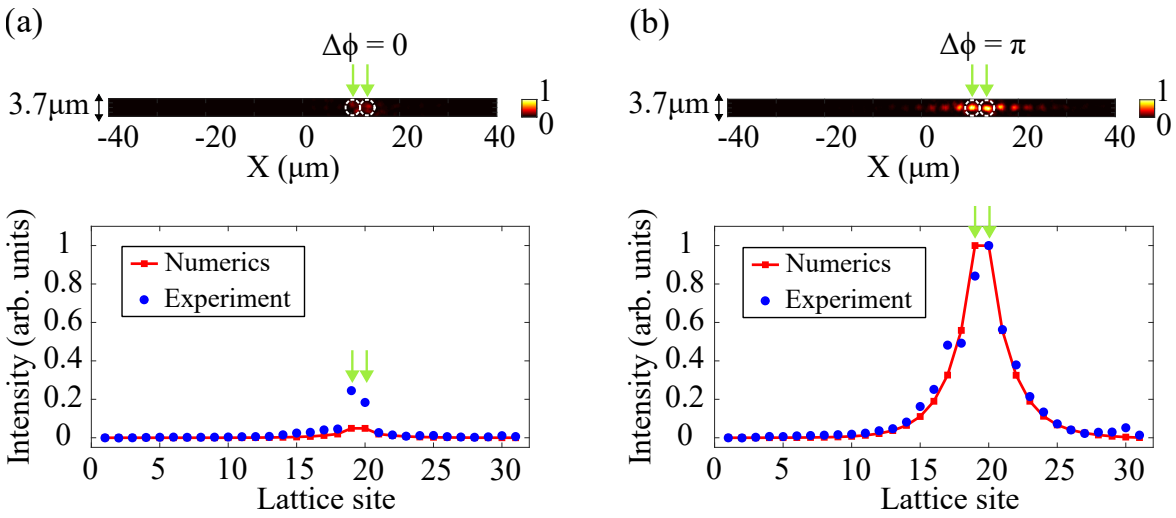

Figure 2.2: (a, b) Real-space light distribution and corresponding site-integrated intensity distribution for the OFF ($\Delta\phi = 0$) and ON state ($\Delta\phi = \pi$), both with excitation at the top of the band ($\Delta/t = 0.87$).

Efficient excitation of the lattice mode at the top of the band requires a relative phase of π between neighboring sites. In this case, shown in Fig. 2.2(b), the field injected by the two laser spots interferes constructively and gives rise to a highly emissive ("ON") state that propagates away from the pump spots. If instead of the modes on the top of the band (antisymmetric nature), we had addressed the symmetric modes of the bottom of the band, we would expect the drive phase pattern of the "ON" and "OFF" response to be reversed. It is important to note that, although the y-axis of Fig. 2.2(a,b) is expressed in arbitrary units, the same scale is used in each case, thereby highlighting the contrast between destructive interference on left panel (a) and constructive interference on the right panel (b).

The observed decay of the emitted intensity away from the pumped sites in Fig. 2.2(b) arises from the continuous escape of photons as they propagate in the lattice. Note that in these experiments, under resonant injection, energy relaxation of the injected photons is negligible. The measured output field is emitted at the exact same frequency as the driving laser. Optical switching thus represents one manifestation of this interference-driven control, while in the following section we show how the same mechanism can be harnessed to achieve directional transport.

Note that all numerical results (shown as red squares) are plotted alongside the experimental data for comparison in this section, whereas the details of the numerical modeling section will be discussed later in this chapter.

2.3 Directional propagation

Another striking phenomenon that arises from the interference between the drive and lattice modes is the directional propagation of light [50]. This phenomenon has been thoroughly studied in the context of quantum emitters coupled to waveguides and lattices [134–138]. This situation can be observed when setting the drive photon energy to $\Delta/t = 0$ ($E_p = E_0$) and properly adjusting the phase between two adjacent pump spots. Figure 2.3(a, b) displays this directional transport phenomenon for phase differences of $-\frac{\pi}{2}$ and $\frac{\pi}{2}$ between the excitation spots. When $\Delta\phi = \frac{\pi}{2}$ (panel (a)), the phase gradient introduced by the pump matches the symmetry of modes with positive group velocity at $\Delta/t = 0$, which propagate to the right. Conversely, for $\Delta\phi = -\frac{\pi}{2}$ (panel (b)), the reversed phase gradient favors coupling to modes with group velocity directed to the left.

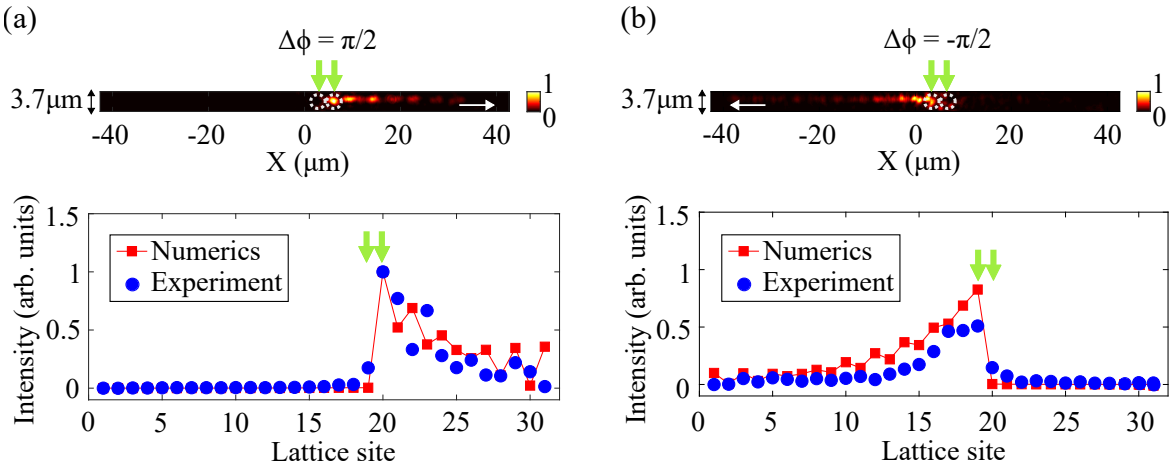

Figure 2.3: (a, b) Real-space emission and corresponding line profiles showing rightward propagation ($\Delta\phi = \pi/2$) and leftward propagation ($\Delta\phi = -\pi/2$), both with excitation at $\Delta/t = 0$.

In Fig. 2.3(a), the decaying intensity to the right of the pump spots displays an oscillating behavior. The reason is that the pump spots ($m = 19, 20$) are positioned relatively near the edge of the lattice ($m = 31$), and the field propagating in the lattice is reflected at the boundary resulting in an interference. In Fig. 2.3(b) this effect is less prominent because the edge $m = 1$ is located farther from the pumping sites. Similar results are found with any other choice of pair of pumped sites as long as they are sufficiently far from the edges.

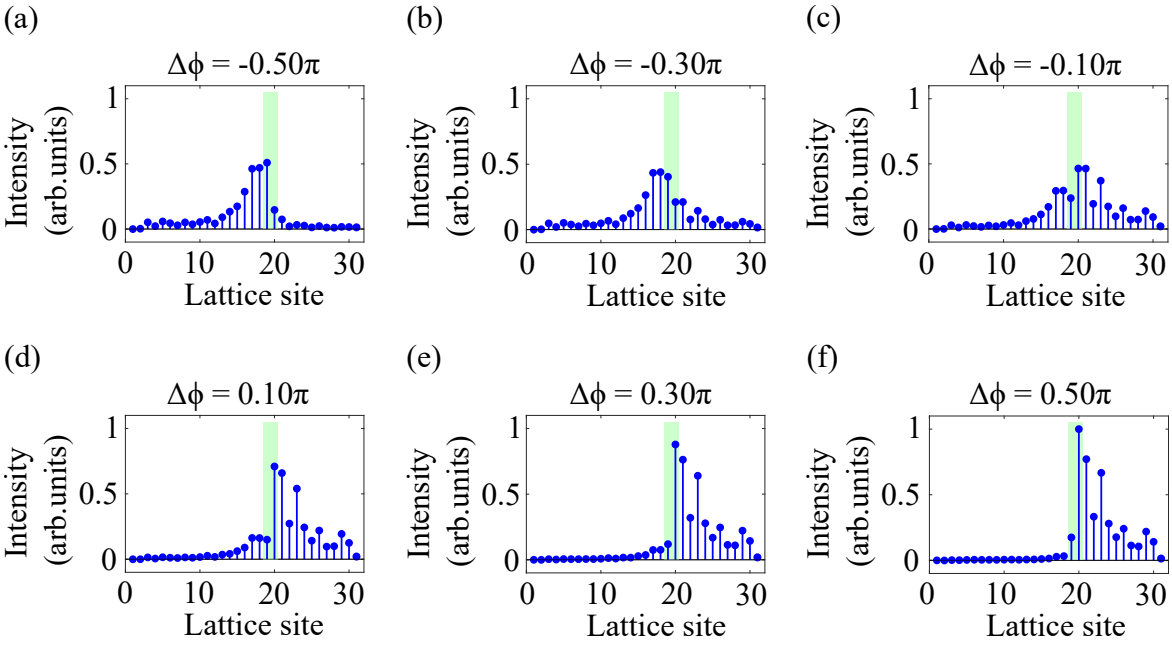

Figure 2.4: (a–f) Experimentally measured intensity profiles for different pump phase differences $\Delta\phi$ between two adjacent sites, ranging from -0.5π to 0.5π. The laser detuning is set to $\Delta/t = 0$. Each panel corresponds to a distinct phase difference between the two excitation spots showing qualitative agreement with the numerical results in Fig. 2.5. Shaded areas correspond to the sites $(19, 20)$ where the external pump is applied.

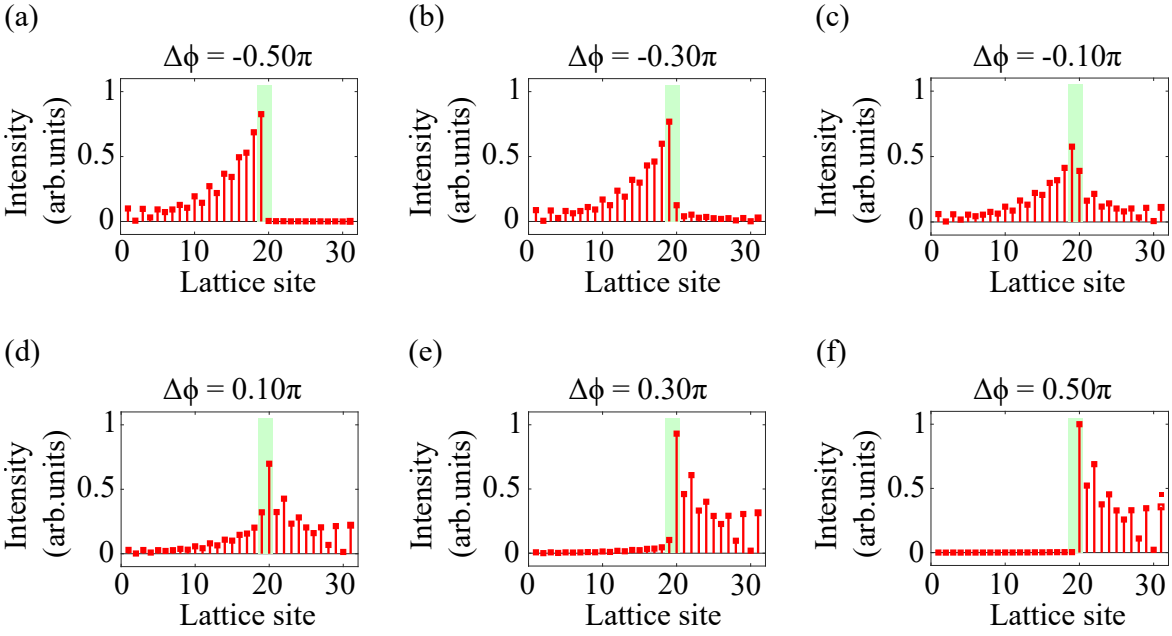

Figure 2.5: (a–f) Numerical steady-state intensity profiles for different pump phase differences $\Delta\phi$ between two adjacent sites, ranging from -0.5π to 0.5π. The laser detuning is set to $\Delta/t = 0$. The strongest leftward transport occurs at $\Delta\phi = -0.5\pi$, while rightward transport is maximized at $\Delta\phi = +0.5\pi$. Shaded areas indicate the pumped sites (19, 20).

To gain further insights on the transition from the left to right directional transport, we compare the spatial intensity profiles measured experimentally as shown in Fig. 2.4 and numerically in Fig. 2.5 as a function of the phase difference between the two pump spots. Tuning the phase difference in Figs. 2.4 and 2.5 from -0.5π to $+0.5\pi$ induces a gradual shift in the direction of light propagation within the lattice. This behavior arises from constructive and destructive interference between drive and lattice eigenmodes, which alters the balance between left- and right-propagating components. Both simulations and experiments exhibit the strongest asymmetry at $\Delta\phi = \pm\frac{\pi}{2}$: a phase difference of $-\pi/2$ leads to maximum transport to the left, while $+\pi/2$ results in maximum transport to the right.

To quantify directional emission in the lattice, we define the total intensities emitted to the left and right of the pumped region as $I_L = \sum_{m<m_{\text{pump}}} I_m$ and $I_R = \sum_{m>m_{\text{pump}}} I_m$, where I_m denotes the intensity at the lattice site m after normalization of the total emitted intensity in all lattice sites to 1 ($I_{total} = \sum_m I_m = 1$). The pump lattice sites are denoted as m_{pump} (in our case, sites 19 and 20). The pumped sites are excluded from the summation to ensure that only the transported intensity is considered. The directional transport (D) is then defined as

$$D = \frac{I_R - I_L}{I_R + I_L} \tag{2.3}$$

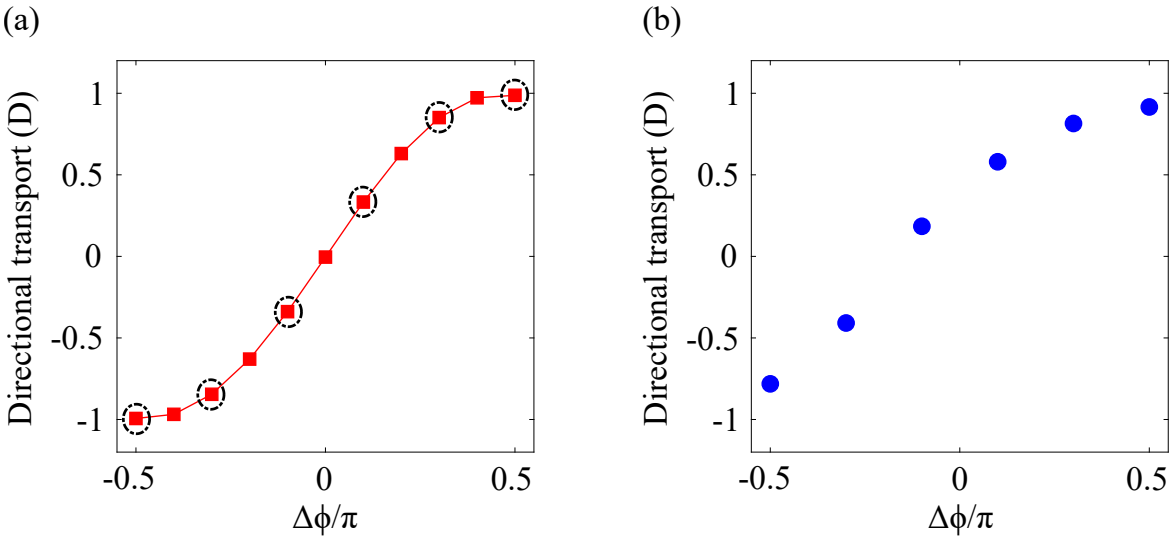

Figure 2.6: Phase dependent directional transport $D(\Delta\phi)$ extracted from both numerical simulations panel (a) and experimental measurements panel (b). The six black circles in panel (a) mark the phase values used in the experimental measurements shown along the x-axis in panel (b).

By definition, D lies in the range $[-1, 1]$ and provides the fraction of directional emission. $D = 0$ implies mode symmetry distribution on both sides. Positive values of D indicate net rightward transport, while negative values indicate leftward transport. Fig. 2.6(a) presents the directional transport D as a function of the phase

difference $\Delta\phi/\pi$ between the two laser spots obtained from simulations of Eqs. 2.5 and 2.6 (both equations are presented in the next section of numerical modeling).

Figure 2.6(b) shows the corresponding experimental results. To illustrate directional transport quantitatively, we highlight two representative phase values. When $\Delta\phi = -\frac{\pi}{2}$, 78% of the injected light is directed to the left of the pumped region (excluding the pumped sites), while only 22% is observed to the right. In contrast, for $\Delta\phi = +\frac{\pi}{2}$, the directionality is reversed, with 92% of the light appearing to the right of the pump spots and just 8% to the left.

2.4 Numerical modeling

To better understand the system and enable a direct comparison with the experiment, we have developed a numerical model of an array of 31 coupled sites in the tight-binding limit. To keep track of the hybrid light matter nature of the micropillar resonances, we model each site m with a discrete cavity mode $\psi_{C,m}(t)$ and an exciton mode $\psi_{X,m}(t)$. This is a discretized version to take into account the lattice of the equation introduced in Chapter 1. This numerical model is introduced not only to analyze the present transport phenomena, but also as a general framework that will be applied to the study of localization effects discussed in Chapter 3. The two coupled fields are assembled into a state vector $\mathbf{y}(t) \in \mathbb{C}^{62}$:

$$\mathbf{y}(t) = \begin{bmatrix} \psi_{C,1}(t) \\ \psi_{X,1}(t) \\ \psi_{C,2}(t) \\ \psi_{X,2}(t) \\ \vdots \\ \psi_{C,31}(t) \\ \psi_{X,31}(t) \end{bmatrix} \tag{2.4}$$

The time evolution of the system is governed by the following coupled differential equations [139]:

$$i\hbar\frac{d\psi_{C,m}}{dt} = \left(\delta_C - i\frac{\gamma_C}{2}\right)\psi_{C,m} + \frac{\hbar\Omega_R}{2}\psi_{X,m} + t\sum_{\langle n\rangle}\psi_{C,n} + t'\sum_{\langle\langle n\rangle\rangle}\psi_{C,n} + F_m \tag{2.5}$$

$$i\hbar\frac{d\psi_{X,m}}{dt} = \left(\delta_X - i\frac{\gamma_X}{2} + g_X|\psi_{X,m}|^2\right)\psi_{X,m} + \frac{\hbar\Omega_R}{2}\psi_{C,m} \tag{2.6}$$

where $\delta_C = E_p - E_C^0$ and $\delta_X = E_p - E_X$ denote the photon and exciton detunings relative to the pump energy E_p, the photon and exciton decay rates are γ_C and γ_X, the term $g_X|\psi_{X,m}|^2$ captures the exciton-exciton nonlinearity, and $\langle n\rangle$ and $\langle\langle n\rangle\rangle$

refer to the nearest- and next-nearest-neighbors. The pump F_m is applied at two sites m_1 and m_2 with a relative phase difference $\Delta\phi$ as:

$$F_m = F_p \left(\delta_{m,m_1} + e^{i\Delta\phi} \delta_{m,m_2} \right) \tag{2.7}$$

where $\delta_{m,m_{1,2}}$ is the Kronecker delta function. In the model, only the photon field $\psi_{C,m}$ undergoes hopping between sites via the nearest (t) and next-nearest-neighbor (t') couplings, while the exciton field $\psi_{X,m}$ remains localized due to its significantly larger effective mass compared to the photon. At low input intensities, Eqs. 2.5 and 2.6 have a steady-state solution for each configuration of the drive field F_m. To solve the coupled exciton–photon Eqs. 2.5 and 2.6, we employ MATLAB's `ode15s` solver, which is specifically designed to handle stiff systems of ordinary differential equations. It uses variable-order, implicit integration methods based on numerical differentiation formulas (NDFs), which make it ideal for simulating photon and exciton interactions within photonic lattices.

We have performed numerical simulations under the conditions of the experiments shown in Fig. 2.2(a-b) and Fig. 2.3(a-b). In these simulations in the linear regime, $g_X = 0$ and both excitation spots are driven with equal amplitudes F_p. For convenience, we set $\gamma_x = \gamma_c \equiv \gamma$ with a value of 0.12 meV, which fits the measured decay of the polariton intensity in Fig. 2.2(b). We numerically reproduce the key experimental observations: the existence of ON and OFF states in Fig. 2.2(a) and Fig. 2.2(b), as well as the directional propagation across the lattice displayed in Fig. 2.3(a) and 2.3(b). In Fig. 2.2(a), the driven sites exhibit significantly less intensity in the numerical simulations compared to the experiment, which can be attributed to the ideal mode matching between the pump and each site in the simulations. The simulation in Fig. 2.3(a) reproduces the intensity oscillations observed in the experiment, which arise from the interference between the right propagating field and the polaritons reflected from the edge of the lattice.

2.5 Analytics - tunable directional transport

After experimentally observing and numerically confirming scenarios enabling light transport and manipulation in the lattice, we next ask whether additional, less intuitive transport regimes may exist within the accessible parameter space. To explore this, we derive an analytical expression based on a Fourier-space solution of the steady-state coupled Eqs. 2.5 and 2.6 following the methods introduced in Ref. [140]. Specifically, we consider an infinite 1D lattice for two coherent pumps applied at distinct lattice sites m_1 and m_2 and solve the equations in momentum space, followed by an inverse Fourier transform to recover the photonic spatial field distribution $|\psi_{C,m}|^2$. To simplify the analytical expression, we consider the case $t' = 0$ and the limit of purely photonic polaritons, which implies that the

lattice bandwidth is $4t$. The detailed derivation is given in the Appendix B. The photon intensity at each site m takes the form:

$$|\psi_{C,m}|^2 = |F_p|^2 D(\Delta)^2 \left| e^{ik_0|m-m_1|} e^{-\gamma D(\Delta)|m-m_1|} + e^{i\Delta\phi} e^{ik_0|m-m_2|} e^{-\gamma D(\Delta)|m-m_2|} \right|^2 \quad (2.8)$$

where $k_0 \equiv \arccos\left(\frac{-\Delta}{2t}\right)$ and $D(\Delta) = \frac{1}{\sqrt{4t^2-\Delta^2}}$ is the density of states. From Eq. 2.8, we derive the general conditions that establish the relation between Δ and $\Delta\phi$ for directional propagation to occur. For propagation to the right, we impose destructive interference in the region to the left of the pump spots, i.e. $|\psi_{C,m}|^2 = 0$ for $m < \min(m_1, m_2)$ in the limit of negligible losses $\gamma \ll t$. This leads to the condition (derivation in Appendix B):

$$\cos\left(\Delta\phi + k_0(m_2 - m_1)\right) = -1 \quad (2.9)$$

which yields the phase-matching requirement:

$$\Delta\phi + k_0(m_2 - m_1) = (2\ell + 1)\pi, \quad \ell \in \mathbb{Z}. \quad (2.10)$$

For directional propagation to the left, we get the condition:

$$\Delta\phi - k_0(m_2 - m_1) = (2\ell + 1)\pi, \quad \ell \in \mathbb{Z}. \quad (2.11)$$

Equations 2.10 and 2.11 reveal that directional transport is tunable: for any value of laser detuning Δ, which sets k_0 within the band, there exists a corresponding phase difference $\Delta\phi$ that enables directional propagation, except at the band edges. The appropriate phase difference can be found for any separation between the two pumping spots. In the specific case of $\Delta = 0$ (i.e., $k_0 = \pm\pi/2$) and $m_2 - m_1 = 1$, directional propagation occurs at $\Delta\phi = \pm\pi/2$. Our experiments and numerical simulations confirm this situation, even though they deviate slightly from the conditions in which Eqs. 2.8-2.11 have been obtained: experiments and simulations are done in the presence of losses and include weak next-nearest neighbor coupling and a small excitonic component which modify the shape of the pure photonic band with just next-neighbor hoppings assumed in Eq. 2.8.

2.6 Summary

In this chapter, we report the experimental realization and characterization of a one-dimensional lattice of coupled microresonators. Angle-resolved photoluminescence confirmed that the structure supports the expected coupled modes and that its dispersion relation is well described by a tight-binding model with nearest and next-nearest-neighbor hopping. Building on this foundation, we demonstrated that interference between lattice modes and multiple coherent external drives can be harnessed as an active control mechanism. By resonantly exciting adjacent sites

with tunable relative phases, we achieved two key functionalities: optical switching and directional transport. To compare these results, we developed a numerical model based on coupled exciton–photon equations and further derived an analytical description that establishes phase-matching conditions for tunable transport. Beyond transport, the interference framework developed here likewise underpins the study of localization phenomena, which will be the focus of the next chapter.

3

NONLINEAR LOCALIZATION OF LIGHT IN A 1D DRIVEN-DISSIPATIVE LATTICE

In the previous chapter, we demonstrated how interference between two external coherent drives and lattice eigenmodes can be used to achieve optical switching and tunable directional transport in a one-dimensional photonic lattice. In this chapter, we extend this approach to investigate localization phenomena. We first study localization in the linear regime, where interference effects lead to the formation of spatially confined steady states. We then explore the nonlinear regime, where increased driving power acts as a tuning parameter, enabling nonlinear localization at frequencies inaccessible in the linear case. To gain a deeper understanding of the factors that influence interference and thus affect localization, the experimental results are complemented by numerical simulations. These simulations allow us to disentangle the respective contributions of the external coherent drive (which establishes phase-controlled interference), hopping and onsite disorder, nonlinear saturation effects, and stray light, providing a comprehensive picture of how driving, disorder, and interactions can shape and alter interference-driven localization in a simple $1D$ driven dissipative photonic lattice.

3.1 Localization by drive and dissipation

The engineering of localized modes in photonic lattices is a widely established approach, as such modes are fundamental in enhancing light-matter interactions, amplifying nonlinear responses, and enabling information storage within highly confined spatial volumes. They also serve as a useful testbed for investigating how different structural arrangements ranging from periodicity to disorder and quasi-periodicity, affect wave propagation in complex photonic systems [141–143]. Therefore, a variety of strategies have been implemented to realize localization, most of which exploit the spectral features of a lattice such as bandgaps, flat bands, van Hove singularities, and Dirac cones that determine the degree of confinement. These spectral features underpin different mechanisms to achieve localization, many of which are governed by interference effects. Some representative examples include defect modes, where localized states emerge within the bandgap due to intentional breaking of translational invariance [144]; Anderson localization, in which random fluctuations suppress wave transport and induce strong spatial confinement [141, 145]; flat-band states, where destructive interference eliminates dispersion, leading to compact localized states [17, 146, 147]; bound states in the continuum (BICs), in which radiative channels cancel out and the mode remains localized within extended bands [148–151] and the non-Hermitian lattices tuned near the parity-time symmetric condition also exhibit defect-induced localization through the balance of gain and loss [152]. In addition to bulk mechanisms, localization can occur at system boundaries. A well-known example is the Tamm state, where an on-site potential introduced at the edge of a periodic lattice generates a surface-localized mode [153–155]. More recently, lattices with non-trivial topological bands have enabled edge and corner localized modes whose existence and spectral position are protected against certain classes of disorder, without requiring local on-site potential [12, 130, 156–160].

One common feature of the localized modes discussed above is that their localization length typically exceeds a single site. For example, the localization lengths achieved from bound states in the continuum extend over several sites [161] and in disordered systems multiple scattering can confine light to a small cluster of sites. In the case of flat-band lattices, compact localized states arise from destructive interference between at least two lattice sites that carry non-zero amplitudes with opposite phases [162, 163]. These compact modes can then be superposed to form arbitrary localized patterns in arbitrary sites [16]. In all these examples, the localized modes are eigenstates of the system such that their spatial profiles are fixed and do not depend on the particular excitation conditions. Therefore, it is the lattice geometry itself (the specific dielectric arrangement) that sets the position, shape, and spatial extent of the modes, leaving only a very limited flexibility to modify their localization properties after fabrication. Achieving reconfigurable

localized modes independent of the lattice geometry would make it possible to implement on-demand localization in essentially any lattice through external control.

The engineering of drive patterns in photonic lattices has already been shown to produce steady states localized over single or multiple sites, and this concept has been extensively explored in our group in the linear regime [49, 51, 140, 164]. A notable example is the honeycomb lattice of coupled micropillars, where a laser excitation arranged across three sites was demonstrated to confine light onto a single site [49]. Building on this foundation, we now turn to investigate interference induced localization in the nonlinear regime. In the following section, we begin by analyzing localization in a one-dimensional lattice, which serves as a first step toward studying the impact of nonlinear effects in the same lattice.

3.1.1 Derivation of the criteria for linear localization

In the analytical derivation of Chapter 2, we established the conditions for tunability in directional transport: for each value of Δ, a corresponding phase difference $\Delta\phi$ could be chosen to induce transport. Motivated by this result, we now apply the same approach to explore the conditions under which localization arises in Eq. 2.8 for a one-dimensional lattice with two pump spots at the sites m_1 and m_2, separated by $d = |m_2 - m_1|$ as sketched in Figure 3.1. By localization, we mean that the light remains confined between the two pump sites according to the results observed from [49, 51, 140, 164]. For this, we consider the steady-state field

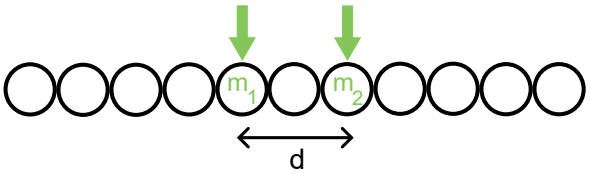

Figure 3.1: Schematic of the lattice with two pump spots at sites m_1 and m_2, separated by $d = |m_2 - m_1|$.

amplitude at an arbitrary site m resulting from coherent driving at two sites m_1 and m_2 in Eq. 2.8. In Eq. 2.8, we focus on sites m that are far from the driven sites m_1 and m_2, such that $|m - m_1|$ and $|m - m_2|$ are both much larger than their separation $d = |m_2 - m_1|$. Since the dissipation γ is small compared to the hopping amplitude, we can set $e^{-\gamma D(\Delta)|m-m_2|} \simeq e^{-\gamma D(\Delta)|m-m_1|}$, allowing us to write the field as

$$\psi_m = FD(\Delta)e^{-\gamma D(\Delta)|m-m_2|}\left[e^{ik_0|m-m_1|} + e^{i\Delta\phi}e^{ik_0|m-m_2|}\right] \tag{3.1}$$

We want to identify how constructive or destructive interference between the two driving fields can lead to enhanced localization at specific sites, depending on

pump separation and relative phase. We aim to find conditions on $\Delta\phi$ and k_0 such that:

1. Destructive interference occurs at all sites $m \leq m_1$,
2. Destructive interference occurs at all sites $m \geq m_2$,

3.1.1.1 *Destructive Interference for $m \leq m_1$*

Introducing $p_1 \geq 0$ such that $m = m_1 - p_1$ we have:

$$|m - m_1| = p_1, \quad |m - m_2| = d + p_1, \quad \text{where } d = m_2 - m_1$$

Replacing with p_1 in Eq. 3.1, the field becomes

$$\psi_m = FD(\Delta)e^{-\gamma D(\Delta)|m-m_2|}e^{ik_0 p_1}\left(1 + e^{i(\Delta\phi + k_0 d)}\right) \tag{3.2}$$

Destructive interference condition require $\psi_m = 0$ which is satisfied for:

$$1 + e^{i(\Delta\phi + k_0 d)} = 0 \tag{3.3}$$

3.1.1.2 *Destructive Interference for $m \geq m_2$*

Introducing $p_2 \geq 0$ such that $m = m_2 + p_2$ we have:

$$|m - m_1| = d + p_2, \quad |m - m_2| = p_2$$

Replacing with p_2 in Eq. 3.1, the field becomes

$$\psi_m = FD(\Delta)e^{-\gamma D(\Delta)|m-m_2|}e^{ik_0(d+p_2)}\left(1 + e^{i(\Delta\phi - k_0 d)}\right) \tag{3.4}$$

Destructive interference condition require $\psi_m = 0$ which is satisfied for:

$$1 + e^{i(\Delta\phi - k_0 d)} = 0 \tag{3.5}$$

Assembling these conditions of Eq. 3.3 and Eq. 3.5 requires simultaneously satisfying:

$$\Delta\phi = (2n+1)\pi + k_0 d \tag{i}$$
$$\Delta\phi = (2n+1)\pi - k_0 d, \tag{ii}$$

As $\Delta\phi$ is defined modulo 2π, the only solution is $k_0 d = \pm\pi$. This criterion is generic and applies to any separation d (in lattice spacings). In the experiment, we focus on the simplest case where the two pump spots enclose a single site (i.e., $d = 2$), therefore k_0 must be equal to $\pm\frac{\pi}{2}$. These k_0 values are satisfied only for

a detuning $\Delta = 0$, providing the condition to observe localization. The analysis therefore highlights a fundamental distinction: while directional transport is tunable, localization is restricted to zero energy ($\Delta = 0$).

3.2 Localization in linear regime

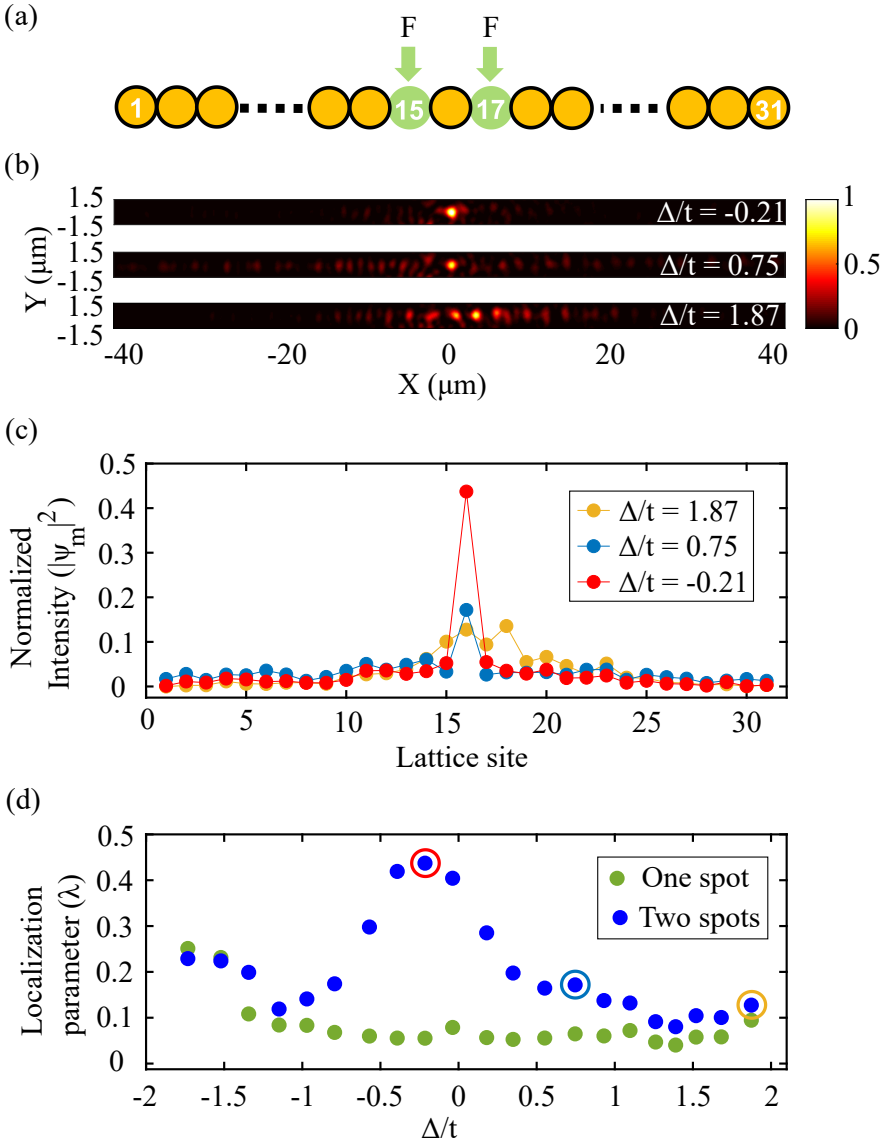

Figure 3.2: (a) Schematic of the 1D lattice consisting of 31 micropillars, with excitation spots with equal phase $\Delta\phi = 0$ and enveloping a single site. (b, c) Real-space intensity distributions for three values of $\Delta/t = -0.21$, 0.75, and 1.87, along with their corresponding line profiles. (d) Δ/t scan spanning from the bottom to the top of the dispersion band, presented for two cases: a single excitation spot on the 15th site -green dots-, and with two excitation spots on the 15th and 17th sites -blue dots-.

Having established analytically that localization occurs exclusively at zero energy for $d = 2$, here we want to explore that experimentally. In this section, we describe how localization can be observed in a one-dimensional lattice with two external drives. In contrast to the optical switching and directional transport experimental set up, where the phase difference between the two spots was tuned using a piezo-controlled mirror, here we employ a Spatial Light Modulator (SLM) for reasons of experimental convenience to maintain a constant phase difference ($\Delta\phi = 0$) between the two laser spots. Two-beam excitation is generated using a reflective phase-only SLM (PLUTO-2.1-NIR-015 (HR)), which is based on a liquid crystal on silicon (LCOS) microdisplay with a full HD resolution of 1920 × 1080 pixels, $8\mu m$ pixel pitch and an input frame rate of $60Hz$. The SLM is integrated into the excitation path to shape and control the phase profile of the driving beams. A detailed description of the algorithm used to generate the phase patterns for the SLM, as well as the calibration procedure, is provided in Appendix B of [100].

3.2.1 Experimental results

Two coherent laser beams of equal intensity and phase ($\Delta\phi = 0$) are focused at lattice sites $j-1$ and $j+1$ as sketched in Fig. 3.2(a). Following the discussion in the previous section, we expect localization of light at the central site for $\Delta/t = 0$, with negligible intensity under the pump spots or anywhere else. However, in the experiment, we observe localization at the central site for a laser detuning $\Delta/t = -0.21$, corresponding to an energy detuning of $E_p - E_0 = -0.07\,\text{meV}$, as displayed in Fig. 3.2(b)-(c). The deviation from $\Delta/t = 0$ arises from the next nearest neighbour coupling t', a common effect that has already been reported in studies of localization in honeycomb lattices [49]. It should be noted that t' was not included in the analytical derivation of Eq. 2.8 and the value was identified from the lattice dispersion fit in Chapter 2. At other laser detunings, Fig. 3.2(b)-(c) shows a broader distribution of light across the lattice. In panel (c), the measured intensity is normalized such that the total sum of the squared intensities over all lattice sites is equal to 1 (i.e., $\sum_m |\psi_{C,m}|^2 = 1$).

The degree of localization can be quantified with the localization parameter:

$$\lambda = \frac{|\psi_j|^2}{\sum_m |\psi_m|^2}. \tag{3.6}$$

It measures the fraction of the total intensity at site j (in between the two pump spots), which is where we expect the localization to happen. A higher value of λ indicates a greater degree of localization between the pumping spots, whereas a lower value describes extended modes across the lattice. Figure 3.2(d) -blue dots- displays the measured values of λ in the configuration of panel (a) when the laser energy is scanned across the entire band. It confirms that the maximum localiza-

tion occurs exclusively at $\Delta/t = -0.21$. This behavior is very different from the case of a single spot excitation, in which light spreads over all lattice sites at all excitation energies as shown in green dots in Fig. 3.2(d). Note that at the band edges at around $\Delta/t \approx -1.7$ and $+1.9$ the low group velocity (exactly zero at the band edge) results in a significant degree of localization for both one and two spots.

3.3 Numerical Modeling of Linear Localization

While the previous section focused on the experimental observation of localization, here we present the corresponding numerical modeling of linear localization to enable qualitative comparison with the experimental results. The numerical modeling follows the same approach described in Chapter 2 for switching and transport. However, in this case, instead of two adjacent excitation spots, the excitation beam consists of two spots (pumped sites are 15 and 17 in this configuration) that surround a single site (site 16) as implemented in the experiment.

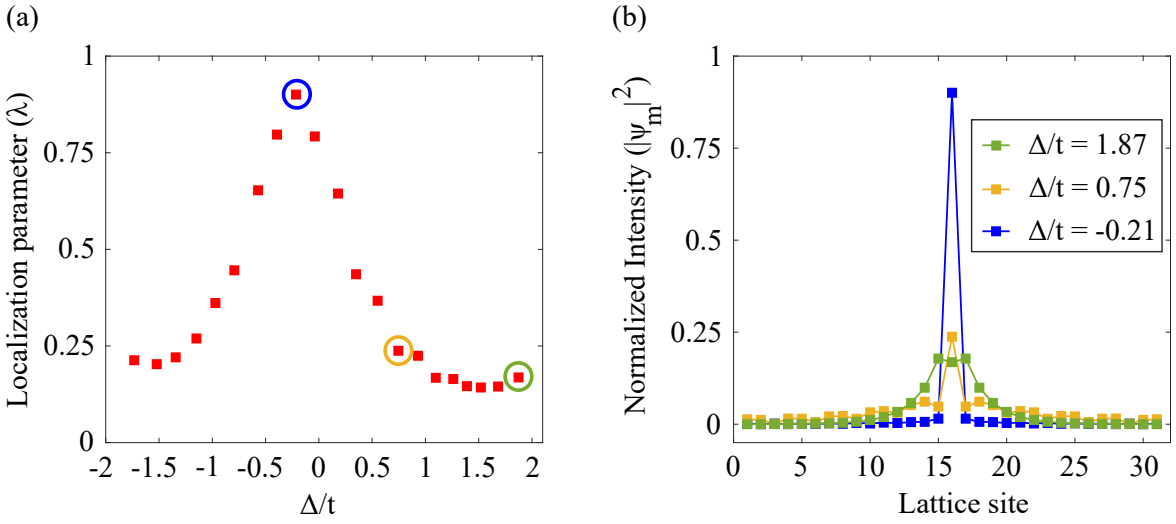

Figure 3.3: (a) Δ/t scan spanning from the bottom to the top of the lowest band in numerics, presented for two excitation spots on the 15th and 17th sites. In panel (a), the three circles in green, yellow, and blue correspond to $\Delta/t = 1.87$, 0.75, and -0.21, respectively and their line profiles are displayed in panel (b).

Figure 3.3(a) shows the localization parameter as a function of Δ/t obtained by scanning the band from top to bottom, analogous to the experimental results presented in Fig. 3.2(d) for two-spot excitation. The three marked circles in panel (a) indicate selected detuning values ($\Delta/t = 1.87$, 0.75, and -0.21), and their corresponding line profiles are displayed in Fig. 3.3(b), in direct analogy with the experimental profiles of Fig. 3.2(c). The numerical simulations qualitatively reproduce the experimental observations, with the highest localization value occurring at $\Delta/t = -0.21$. However, quantitatively, the numerical localization parameter (λ) is significantly higher than in the experiment (except near band edges), reaching nearly twice the value at $\Delta/t = -0.21$. The possible reasons for this discrepancy will be analyzed and discussed in detail in the final section of this chapter.

3.4 Nonlinearity enabled localization

In the linear regime, the maximum localization occurs at $\Delta/t = -0.21$. To understand how the localization is modified by interactions, we explored the role of on-site Kerr nonlinearities in shaping the steady-state field at the site located between the two pump spots. A recent theoretical study by Muñoz de las Heras et al. [140] demonstrated that in the presence of nonlinearities, strong localization can also occur at different detunings. In our experiment, the nonlinear interaction strength is controlled via the power of the coherent pumps, which modulates the polariton density.

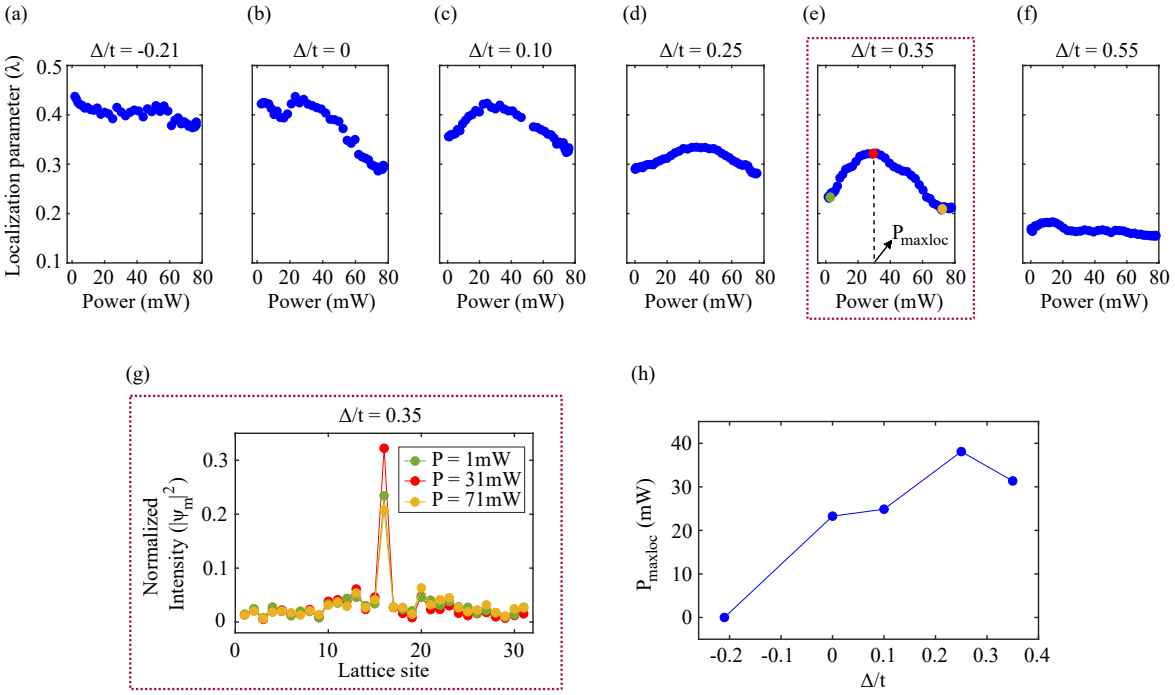

Figure 3.4: (a)-(f) Power dependence of the localization parameter for six different detunings Δ/t: -0.21, 0, 0.10, 0.25, 0.35, and 0.55. (g) Line profiles for three different powers (1 mW, 31 mW, and 71 mW) at a detuning of $\Delta/t = 0.35$, indicated by different markers in (e). (h) Maximum localization power (P_{maxloc}) as a function of the first five detunings. For $\Delta/t = 0.55$, P_{maxloc} is not included in (h) as nonlinearity-induced localization is no longer observed.

3.4.1 Experimental results

Figure 3.4(a)-(f) display the measured localization parameter (λ) as a function of the pump power at six laser detunings. At $\Delta/t = -0.21$ (Fig. 3.4(a)), at low power, we measure $\lambda = 0.44$, which indicates a strong localization. When increasing the pump power, the localization level slightly decreases. When the laser detuning is increased to $\Delta/t = 0$ (Fig. 3.4(b)), the value of λ at low power is smaller than at $\Delta/t = -0.21$, and the highest localization is observed at a laser intensity of about

23 mW before significantly declining at higher powers. This trend becomes clearer at higher detunings up to $\Delta/t = 0.35$, displayed in Fig 3.4(e), when the highest measured localization takes place at 31mW (see Fig. 3.4(g) for a comparison of the mode distribution at three different powers). The power at which the highest localization takes place increases with the detuning as displayed in Fig. 3.4(h). At even higher detunings ($\Delta/t = 0.55$, Fig. 3.4(f)) the measured impact of the nonlinearity becomes weak. The modifications of λ across varying pump powers and laser detunings show that nonlinearity modifies the interference conditions in the lattice to partially re-establish localization. Therefore, for specific detunings, the non-linearity shifts the resonance of the localized field pattern to higher frequency (a blue shift) that re-establishes localization.

3.5 Numerical Modeling of Nonlinear Localization

To further understand this phenomenon, we revisit the numerical results of Ref. [140], which uses a Gross-Pitaevskii model to describe the localization in a lattice similar to the one discussed in our work. The model in that work assumes no next-nearest neighbor hopping, and it predicts a linear scaling of the power at which maximum localization occurs (P_{maxloc}) with increasing detuning. However, this mean-field approach does not account for nonlinear saturation effects that arise from the mixed light-matter nature of polaritons. To address this limitation, we use the model presented in Eqs. 2.5 and 2.6.

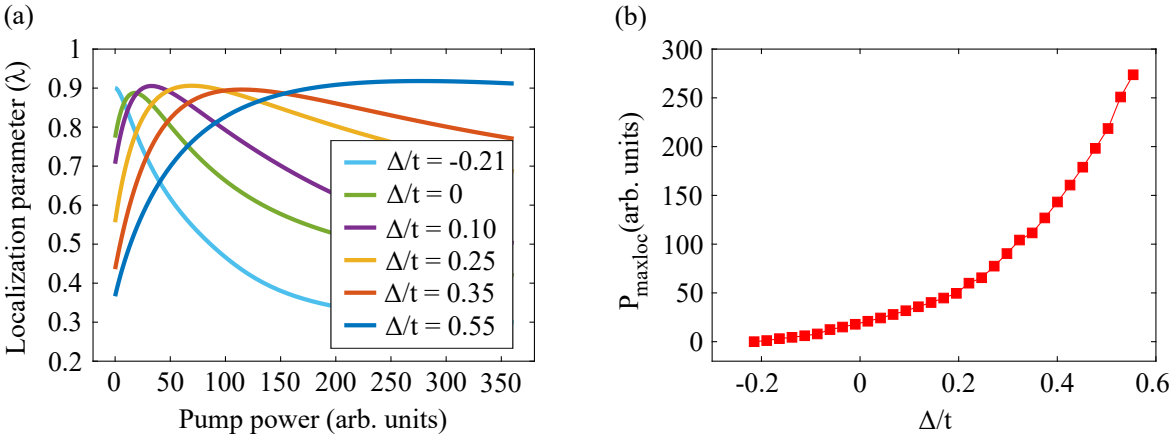

Figure 3.5: (a) Numerical results for the λ dependence on pump power for the same detuning settings as in the experiments in Fig. 3.4, with $g_x \neq 0$. (b) Maximum localization power (P_{maxloc}), as a function of detuning Δ/t.

Figure 3.5(a) displays the numerically computed value of λ as a function of the pump power for various detunings using the lattice parameters of the simulations in Fig. 2.1. For $\Delta/t = -0.21$, the localization is initially high at low pump powers but gradually decreases with increasing power. In contrast, for other detunings, λ increases with pump power, reaching a peak at a specific value P_{maxloc}, after which it begins to decline. For large detunings such as $\Delta/t = 0.35$ and 0.55, the

localization grows more gradually and eventually saturates, reflecting a nonlinear plateau.

These simulations show that a high degree of localization can be recovered at any of the studied detunings for the proper value of the driving power. However, in contrast to the results in Ref. [140], the pump power required to reach the maximum λ increases superlinearly with detuning, as observed in Fig. 3.5(b). The reason is that in the two coupled equation model used in our study, exciton interactions lead to an increase in the exciton self-energy, whereas the photon energy is not affected by them. As a result, the lower-branch polaritons constituting the lattice modes become increasingly photonic with power, leading to a reduction in their effective interactions. This self-limiting behavior leads to the superlinear increase of P_{maxloc} with detuning in Fig. 3.5(b), and it also smoothens the response with power at high detunings (Fig. 3.5(a)). Although the model displays an increase of P_{maxloc} with power as in the experiments, there are discrepancies between the simulations in Fig. 3.5 and the experiments reported in Fig. 3.4. In particular, in the experiments, the nonlinear response at large detunings does not show the high localization values observed at $\Delta/t = -0.21$ in the linear regime. To better understand these differences, we examine three possible contributing factors in the following sections.

3.5.1 Effect of disorder in localization

Previous studies have shown that disorder can alter interference-based localization in photonic lattices by degrading phase-coherent transport or suppressing nonlinear localization mechanisms [165–167], motivating us to assess its impact on our system. Therefore, to study the effects of disorder in the localization of light when the pump spots are separated by two sites ($j-1$ and $j+1$), we perform numerical simulations in the linear regime ($g_X = 0$) by including disorder in either onsite or hopping energy. For each value of disorder strength α, the system was simulated with 25 independent disorder realizations. At each realization, the steady-state intensity profile was extracted and normalized. The resulting spatial profiles were then averaged to obtain the disorder-averaged intensity distribution. The error bars represent the standard deviation of the intensity at each site across these 25 realizations, indicating the spread due to random disorder. In this way, we address the typical effect of disorder on the localization feature, rather than a specific realization. In the experiment, only a single (and generally unknown) disorder realization can be present, so our averaging procedure should be understood as a numerical tool to characterize the expected behavior. For the simulations presented in Figs. 3.6 and 3.7 below, the pump spots are located at lattice sites 15 and 17, with a laser detuning of $\Delta/t = -0.21$, with $t = 0.35$meV (nearest-neighbor hopping) and $t' = -0.03$meV (next-nearest-neighbor hopping).

3.5.1.1 *Onsite Disorder*

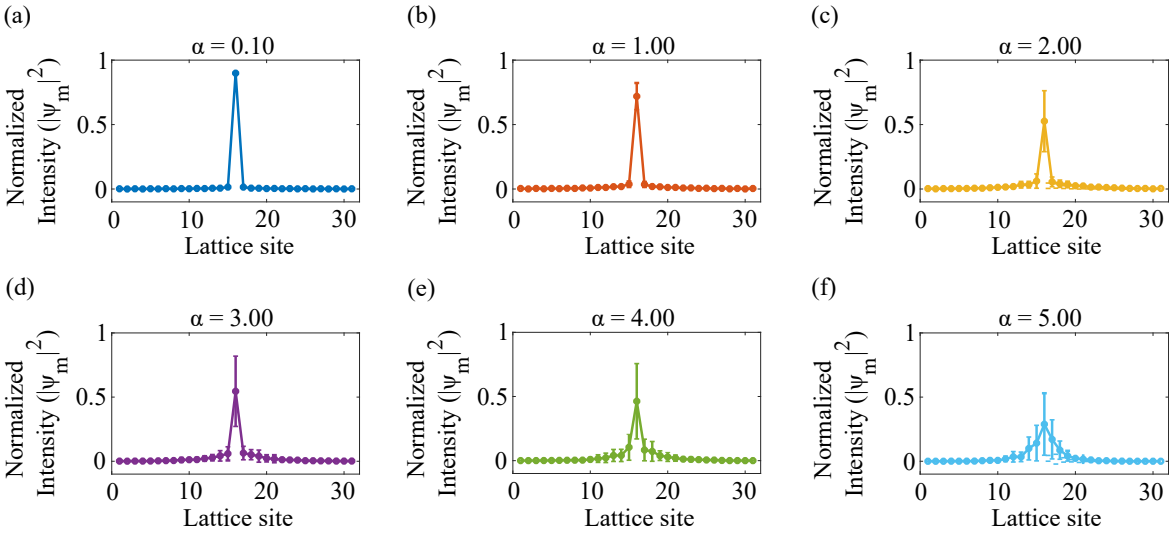

Figure 3.6: Normalized intensity profiles for increasing onsite disorder strength α. (a)–(f) correspond to: (a) $\alpha = 0.1$, (b) $\alpha = 1$,(c) $\alpha = 2$, (d) $\alpha = 3$, (e) $\alpha = 4$ and (f) $\alpha = 5$.

Within a given realization, the photon and exciton experience identical on-site disorder at every site. The on-site disorder for $i \in \{\text{photon}, \text{exciton}\}$ is given by:

$$\text{onsite\_disorder}_i = \alpha \cdot t \cdot \left[\text{rand}(1, N_{\text{pillars}}) - 0.5\right] \tag{3.7}$$

where α is the disorder strength, t is the nearest hopping energy and $\text{rand}(1, N_{\text{pillars}})$ generates a random array of values uniformly distributed in the interval $[0, 1]$. The subtraction of 0.5 centers the disorder around zero.

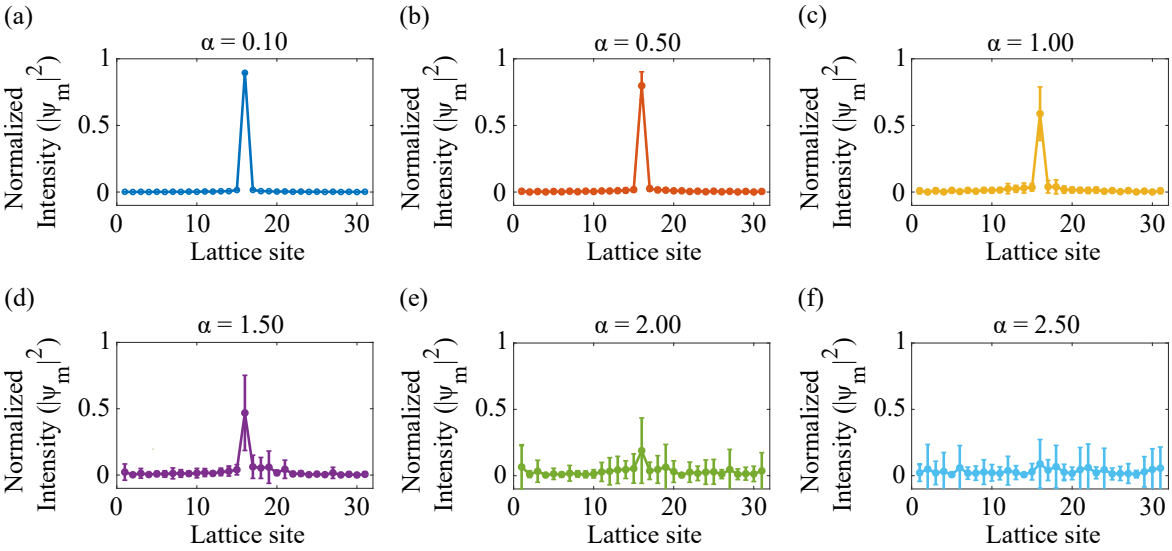

Figure 3.7: Normalized intensity profiles for increasing hopping disorder strength α. (a)–(f) correspond to: (a) $\alpha = 0.1$, (b) $\alpha = 0.5$,(c) $\alpha = 1$, (d) $\alpha = 1.5$, (e) $\alpha = 2$ and (f) $\alpha = 2.5$.

3.5.1.2 *Hopping Disorder*

The hopping disorder for the nearest-neighbor (t) and next-nearest-neighbor (t') couplings is introduced as:

$$t_{\text{disorder}} = t + \alpha \cdot t \cdot \left[\text{rand}(1, N_{\text{pillars}} - 1) - 0.5\right] \tag{3.8}$$

$$t'_{\text{disorder}} = t' + \alpha \cdot t' \cdot \left[\text{rand}(1, N_{\text{pillars}} - 2) - 0.5\right] \tag{3.9}$$

where t, t' are the nearest and next-nearest hopping amplitudes, α is the disorder strength (same as for the on-site disorder), $\text{rand}(1, N)$ generates a uniformly distributed random array in $[0, 1]$.

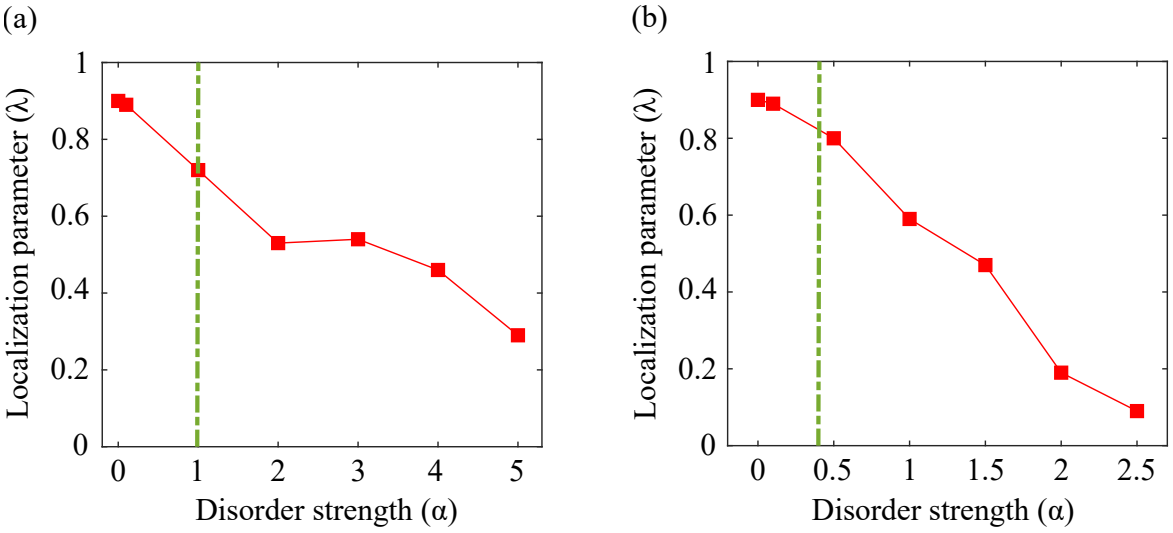

Figure 3.8: Disorder-averaged localization parameter (λ) as a function of disorder strength (α). (a) Onsite disorder, (b) Hopping disorder.

Figure 3.8(a,b) show the localization parameter as a function of disorder strength for onsite and hopping disorder, respectively, extracted from the numerical data shown in Figs. 3.6 and 3.7. A vertical green line is included in each panel to indicate the maximum allowable disorder strength (constitutes an upper bound) that still preserves good agreement with the experimental dispersion in Fig. 2.1(b). For disorder values below the green line, the simulated localization parameter remains higher than the experimentally measured one. This indicates that the localization effect is qualitatively robust even when onsite and hopping disorder exceed the hopping strength, and that our experiments are stable against such imperfections within these ranges. The origin of this robustness lies in dissipation, which plays a key role in protecting localized states from system imperfections. Therefore, it is unlikely that disorder is the main cause of the discrepancy between the measured localization parameter and the simulations based on Eqs. 2.5 and 2.6. Since disorder does not explain the discrepancy, the following subsection explores the role of saturation nonlinearity (g_{sat}).

3.5.2 Effect of saturation nonlinearity in localization

Recent demonstrations of oscillator strength saturation in polariton nonlinearities [95, 168] are a motivation to examine whether this nonlinear saturation could explain the mismatch between our experimental results and the numerics. The oscillator strength saturation originates from phase-space filling: as the exciton density increases, the available electronic states become progressively occupied, reducing the probability of creating additional excitons. This appears in the exciton-photon Hamiltonian as a density-dependent reduction of the Rabi coupling, and an experimental study has confirmed that it can dominate the nonlinear response of polaritons in GaAs microcavities [169]. These findings highlight saturation nonlinearity a particularly relevant parameter to investigate in our system that plays a slightly more complex role than the usual g_X interactions strength. Therefore, with the inclusion of saturation nonlinearity, the exciton-photon model introduced in Eqs. 2.5 and 2.6 takes the modified form:

$$i\hbar\frac{d\psi_{C,m}}{dt} = \left(\delta_C - i\frac{\gamma_C}{2}\right)\psi_{C,m} + \left(\frac{\hbar\Omega_R}{2} - \frac{1}{2}g_{\text{sat}}|\psi_{X,m}|^2\right)\psi_{X,m} + t\sum_{\langle n\rangle}\psi_{C,n} + t'\sum_{\langle\langle n\rangle\rangle}\psi_{C,n} + F_m \tag{3.10}$$

$$i\hbar\frac{d\psi_{X,m}}{dt} = \left(\delta_X - i\frac{\gamma_X}{2} + g_X|\psi_{X,m}|^2\right)\psi_{X,m} + \left(\frac{\hbar\Omega_R}{2} - g_{\text{sat}}|\psi_{X,m}|^2\right)\psi_{C,m} - g_{\text{sat}}\,\psi_{X,m}^2\,\psi_{C,m}^* \tag{3.11}$$

To investigate how saturation nonlinearity modifies localization, we solve the coupled differential Eqs. 3.10 and 3.11 under conditions $g_X = 0$ and $g_{\text{sat}} \neq 0$. To ensure that saturation alone produces a measurable change in the localization pattern within our pump range, we deliberately choose a large coefficient ($g_{sat} = 100g_X$), where g_X is taken from the analysis performed in the earlier section 3.5 of the same chapter. In this case, the oscillator strength saturation becomes the dominant nonlinear mechanism, allowing us to isolate its role in interference for localization. Figure 3.9(a) presents the numerically computed localization parameter λ as a function of pump power for different detunings, using the same lattice parameters as in Fig. 2.1. For $\Delta/t = -0.21$, localization is initially high at low power, but decreases steadily as the pump increases. In contrast, for other detunings ($\Delta/t = 0, 10, 25$), λ increases with power, reaching a maximum value (P_{maxloc}) before decreasing again. At larger detunings, such as $\Delta/t = 0.35$ and 0.55, the increase in localization is more gradual and does not exhibit the saturation observed in Fig. 3.5(a) when the exciton-exciton interaction g_X is present. Importantly, in the case where only oscillator strength saturation is included ($g_X = 0, g_{sat} \neq 0$), the value of P_{maxloc} is

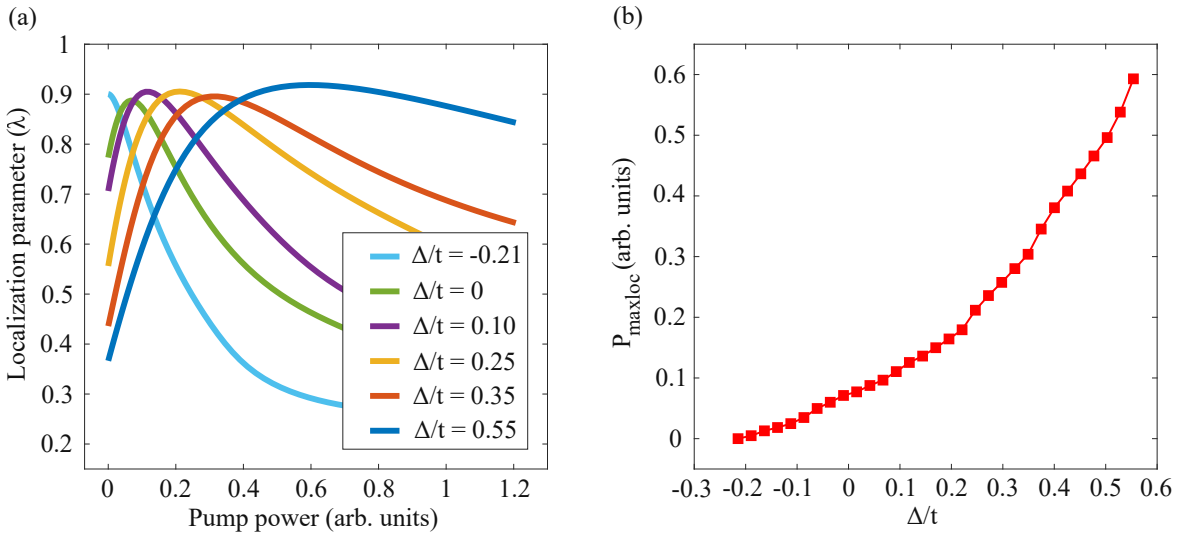

Figure 3.9: (a) Numerical results for the λ dependence on pump power for the same detuning settings as in the experiments in Fig. 3.4, with $g_X = 0$ and $g_{sat} = 100g_X$ (with g_X taken from the analysis done in the earlier section 3.5 of the same chapter). (b) Maximum localization power (P_{maxloc}), as a function of detuning Δ/t.

reached at pump powers significantly lower than in the case with g_X alone for the same detuning in Fig. 3.5(a).

However, the pump power required to reach the maximum value of λ grows superlinearly with detuning, as shown in Fig. 3.9(b), consistent with the trend observed in Fig. 3.5(b). Thus, the inclusion of an additional nonlinear term in Eqs. 2.5 and 2.6 to describe oscillator strength saturation does not qualitatively alter the behavior of the simulations presented in Fig. 3.5, even in the case where saturation nonlinearity dominates over exciton-exciton interactions (g_X).

3.5.3 Effect of stray light in localization

Since neither disorder nor saturation nonlinearity accounts for the discrepancy, we next turn to other possible sources of deviation, with particular attention to experimental limitations. Stray light is a significant factor that can influence the measured localization parameter: unwanted reflections or scattering from the edges of the microstructures reaching the detection camera may introduce parasitic signals, reducing both the precision and contrast of the measurement. The origin of the stray light can be traced down to the geometry of the microstructures we studied. The one-dimensional lattice used in this work was fabricated via deep etching of the upper and lower mirrors of the microcavity down to the GaAs substrate. This procedure ensures a deep confinement of the photonic modes inside the micropillar but allows residual laser light around the sides of the etched micropillars and through the substrate towards the CCD detector and pollute the measured

intensity profiles, in particular close to the excitation spots. Since the localization parameter (λ) is derived from intensity measurements, the presence of stray light can parasitically contribute to the signal, thereby affecting the extracted value of λ.

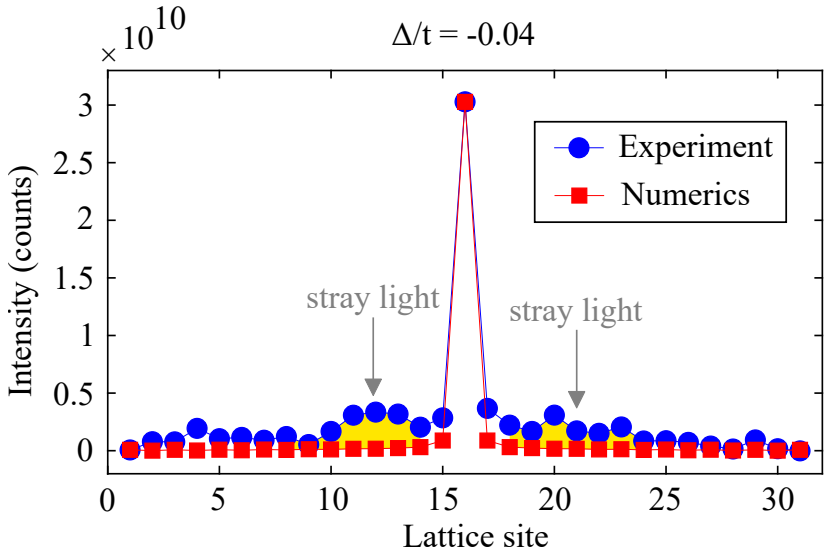

Figure 3.10: Line profile showing the intensity counts for both the experiment and numerical simulations at $\Delta/t = -0.04$, highlighting the presence of stray light (yellow shadow).

Figure 3.10 shows the measured intensity profile (blue points) for $\Delta/t = -0.04$ at low power, along with a simulation in the same conditions (red points). Both data sets have been normalized to the emitted intensity at the localized site. A distinct feature in the experimental data is the presence of a bump on both sides of the pumped sites, which is completely absent in the numerical simulations. It is highlighted with yellow shadows in Fig. 3.10. Similar bumps are observed at all powers and detunings in the experiment, which strongly suggests that its origin is stray light. The next step is to evaluate the influence of stray light, first in the linear regime and subsequently in the nonlinear regime.

3.5.3.1 *Linear Regime*

We focus on the case with detuning $\Delta/t = -0.21$, where localization reaches its maximum in the linear regime, with two pump spots applied at lattice sites 15 and 17. For this detuning, the intensity at the maximally localized site (site 16) in the numerics was matched to the corresponding experimental intensity, as shown in Fig. 3.11(a).

Stray light was artificially added to the simulation as a static background intensity individually to the affected sites (11-15 and 17-23), and the stray light strength s was determined by tuning its value such that the simulated real-space intensity profile approximately reproduces the experimental intensity at the affected sites. This procedure yields a stray light strength of $s = 0.085$, corresponding to 8.5%

per site in the region 11-15 and 17-23 of the total lattice intensity at steady state. The method for incorporating stray light and computing the localization parameter λ is as follows. Let I_n denote the steady-state intensity at site n, obtained from solving the two coupled Eqs. 2.5 and 2.6. The stray light contribution is defined as

$$I_n^{\text{stray}} = \begin{cases} s \sum_{m=1}^{N} I_m, & \text{if } n \in S, \\ 0, & \text{otherwise,} \end{cases} \tag{3.12}$$

where $S \subset \{1, \ldots, N\}$ is the set of stray light affected sites. The total intensity is then

$$I_n^{\text{total}} = I_n + I_n^{\text{stray}} \tag{3.13}$$

and the localization parameter is calculated as

$$\lambda = \frac{I_{16}}{\sum_{n=1}^{N} I_n^{\text{total}}} \tag{3.14}$$

where I_{16} is the intensity at the maximum localized site (in between the two pump spots). This approach enables us to quantitatively assess how the presence of stray light reduces the localization parameter (λ) in the experiment. In

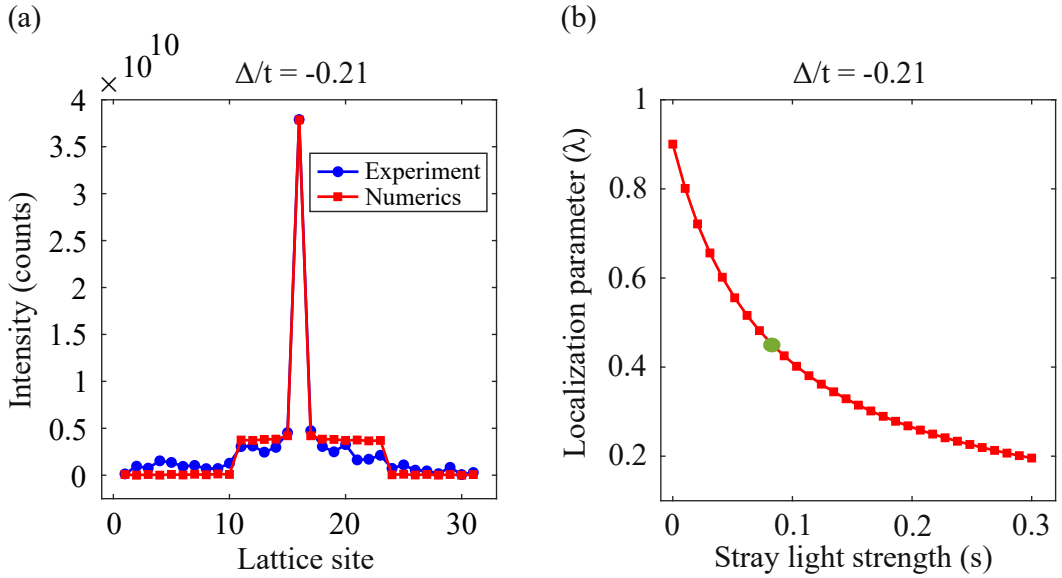

Figure 3.11: (a) Intensity profile (with stray light strength $s = 0.085$) compared to the experimental data at $\Delta/t = -0.21$. (b) Localization parameter λ as a function of stray light strength s.

Fig. 3.11(a), the intensity profile obtained from the numerics (with stray light included at $s = 0.085$) against the experimentally measured profile at $\Delta/t = -0.21$ is plotted. Figure 3.11(b) shows the computed localization parameter λ as a function of stray light strength s. As expected, λ decreases with increasing s, reflecting the delocalizing effect of stray light. The localization parameter corresponding to $s = 0.085$ is highlighted with a green circle which corresponds to $\lambda = 0.445$, matching the experiment value of 0.44.

3.5.3.2 *NonLinear Regime*

From the stray light strength identified from the green circle ($s = 0.085$) in Fig. 3.10(b), we investigate the effect of stray light in the nonlinear regime by numerically calculating the localization parameter (λ) as a function of pump power. Figure 3.12 presents two cases at $\Delta/t = -0.21$: one without stray light and the other with stray light included. In the absence of stray light, λ decreases significantly from 0.90 to 0.38 as the pump power increases, indicating strong nonlinear delocalization as power increases for this specific detuning. In contrast, when stray light is present, λ decreases more gradually, from 0.445 to 0.32. This slower drop suggests that the presence of background intensity (stray light) diminishes the sensitivity of localization to nonlinear effects at this detuning.

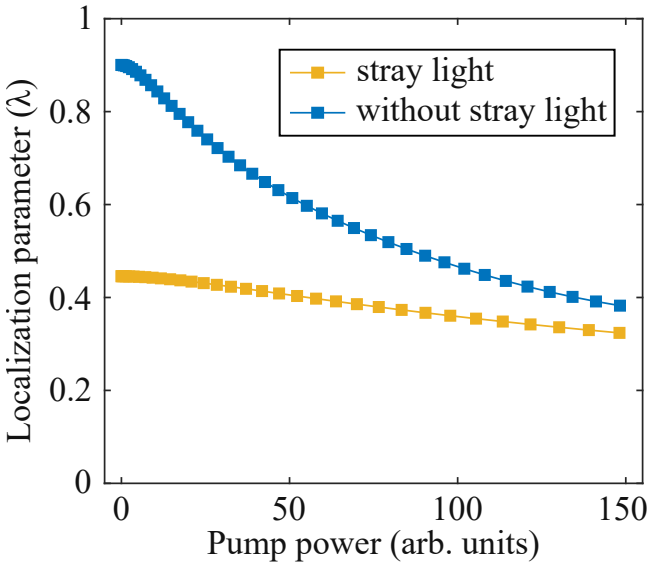

Figure 3.12: Localization parameter λ as a function of pump power with and without stray light.

Therefore, as an illustrative example among the various detunings studied in Figure 3.4, we show that for $\Delta/t = -0.21$, inclusion of stray light in the simulations yields localization parameters close to the experimental values in the linear regime and qualitatively reproduces the power dependence observed in Fig. 3.4(a). A full quantitative agreement between experiment and theory for all detunings would require simultaneously incorporating the effects of stray light, disorder, and other features such as asymmetries between the excitation pump spots. However, the large number of fitting parameters would render such an analysis impractical. Our experimental observations and simulations highlight the main sources of deviation between the real system and Eqs. 2.5 and 2.6, which nevertheless provide a good qualitative description.

3.6 Summary

In this chapter, we have shown that by precisely controlling the laser phase at individual sites and tuning the pump energy, it is possible to manipulate interference patterns and achieve localization in driven-dissipative photonic lattices. We further demonstrated that interactions enable light confinement in frequency regimes inaccessible under purely linear conditions, in agreement with the predictions of [140]. A quantitative discrepancy between the experimental observations and numerical simulations was also identified and systematically examined. Hopping and onsite disorder, as well as nonlinear saturation, were found to be insufficient to account for the deviation. Instead, stray light emerged as the most plausible source, consistent with the sensitivity of interference-based localization explored here.

4

LINE LASING IN A 2D LIEB SP LATTICE

In the previous chapters, the role of phase-controlled interference between external drives and lattice eigenmodes was investigated to achieve tunable directional transport and nonlinear localization under resonant excitation conditions. In this chapter, we shift our focus to engineering band dispersion in a specifically designed driven-dissipative polariton lattice called the Lieb *sp* lattice to achieve lasing in exotic modes. Using a convenient combination of orbital photonic modes, the photonic bands are tailored such that they are flat along one direction and dispersive along the perpendicular one, leading to the emergence of n independent $1D$ line eigenmodes within a $2D$ matrix. The goal of this chapter is to demonstrate line lasing along any of the line modes of the square Lieb *sp* lattice by employing a spatially tailored non-resonant pumping profile. In addition, we show that cross-shaped excitation produces two orthogonal line lasers that can be locked in energy and phase, which otherwise would be independent line lasers. A particularly intriguing effect is the polarization locking that emerges between the two line lasers, each of which exhibits it's own intrinsic polarization when lasing alone. Finally, the experimental protocol used to investigate phase and polarization locking is described, which includes interference measurements to quantify fringe visibility and to elucidate the origin of the observed polarization locking.

4.1 Band Engineering in Driven-Dissipative Photonic Lattice

The engineering of specialty lasers with unconventional mode structures is one of the modern challenges in the development of integrated coherent sources with enhanced functionalities. Examples include the use of bound states in the continuum, microlasers with orbital angular momentum, Dirac-band lasers and topological lasers. The use of periodic photonic structures has been one of the main pathways to design specialty semiconductor lasers with small sizes and straight integrability. Early photonic crystals lasers introduced defect modes to produce single mode out-of-plane laser emission in extremely compact designs [170]. Suffering from limited output power, there have been important efforts to implement designs with large area, single mode operation in integrated geometries with high directionality. A successful pathway has been the use of double-lattice photonic crystal resonators based on an intricate interplay of interference and Hermitian and non-Hermitian couplings [171]. A realization based on AlGaAs materials has demonstrated several Watts output power with submilimeter footprints [172]. A different approach is to engineer photonic band structures based on Dirac dispersions [173]. This method exploits the inherently large frequency separation between in-plane modes in linear dispersions to achieve large-area single-mode operation [174]. Another strategy is to use the one-dimensional edge state of a two-dimensional lattice whose bands possess a non-trivial topology. The robustness of the topological edge mode to local disorder ensures the mode locking of a large number of resonators, resulting in powerful output emission with interesting directional and orbital angular momentum properties both for in-plane [175–177], out-of-plane operation [178, 179] and lasing in line interface modes [180]. In the following sections, we propose and demonstrate an architecture that enables a novel type of lasing emission from a lattice of coupled photonic resonators.

4.1.1 Orbital Lieb lattice

The coupling of orbital modes of individual resonators has been extensively used in photonic [124, 181–183] and atomic systems [184–186] to engineer elaborate band structures. Our design is based on coupled micropillars that combine different orbital modes to create photonic bands with a flat dispersion along one spatial direction and a dispersive band along the perpendicular direction. The eigenmodes of this arrangement are independent line modes that cover the whole lattice.

The building blocks used to implement an orbital Lieb lattice are AlGaAs micropillars grown via molecular beam epitaxy on a two-dimensional GaAs substrate. The lower and upper Bragg mirrors are made of 31 and 27 pairs, respectively, of

$\lambda/4$ alternating layers of $Al_{0.1}Ga_{0.9}As$ and $Al_{0.95}Ga_{0.05}As$. The central GaAs spacer has an optical width of λ. We design λ to be close to 849nm, the lowest energy transition at 4K of an $In_{0.05}Ga_{0.95}As$ quantum well of 17nm in width located at the center of the spacer.

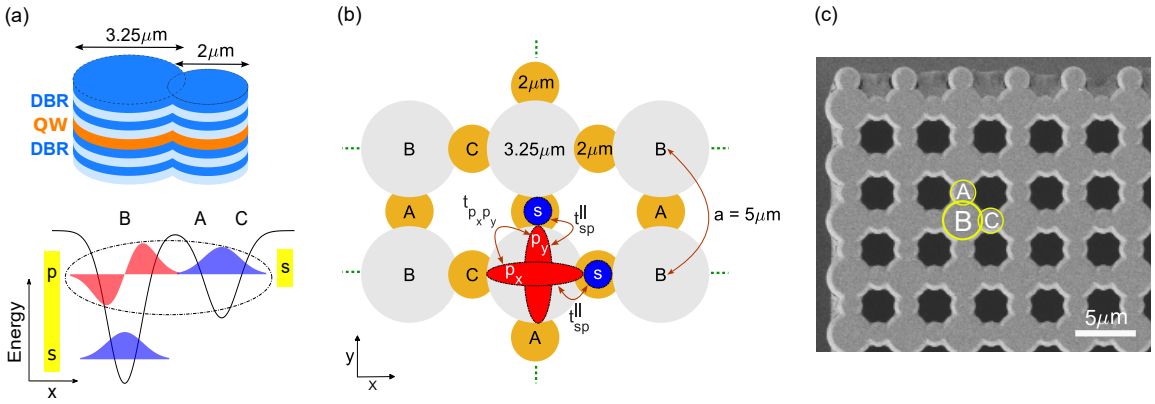

Figure 4.1: (a) Scheme of two coupled micropillars of different diameter. As schematically depicted on the energy level diagram below, the diameters of the micropillars are designed for the p_x and p_y modes of the large micropillar to be at the energy of the s modes of the smaller micropillar. (b) Arrangement of the overlapping orbitals in the sp bands of the Lieb lattice. (c) Scanning electron microscope image of a typical sp Lieb lattice.

The microcavity wafer is then etched down to the substrate in the form of a Lieb lattice of coupled micropillars (see Fig. 4.1(c)). The three-dimensional confinement of light in each individual micropillar results in a series of discrete photonic modes [187, 188] with s, p, d, ... symmetries (see Figs. 4.1(a)-(b)), a labeling inspired by the electronic orbitals of the hydrogen atom. The photon frequency of the modes is determined by the diameter of the micropillar. To make the Lieb sp lattice, we combine micropillars of two different diameters (3.25 and 2μm) with a center-to-center interpillar distance of 2.5μm and a lattice constant of 5μm (see Fig. 4.1). The size of the pillars is designed such that the s modes of the smallest diameter micropillars are at the energy of the first excited p_x and p_y modes of the large diameter micropillars (Fig. 4.1(a)).

The lowest energy modes of the structure are the independent s modes of the large pillars. The first excited set of bands hybridizes the cylindrical symmetric s orbitals of the small micropillars at A and C sites with the p_x and p_y antisymmetric orbitals of the larger pillars at B sites (Fig. 4.1(a) and (b)). The eigenenergies and eigenvectors of this band can be described using a tight-binding Hamiltonian:

$$H_{\mathrm{sp}} = \sum_{l,m} -t_{\mathrm{sp}} \left(|\psi^{\mathrm{B},p_y}_{l,m}\rangle\langle\psi^{\mathrm{A},s}_{l,m}| + |\psi^{\mathrm{B},p_x}_{l,m}\rangle\langle\psi^{\mathrm{C},s}_{l,m}| + |\psi^{\mathrm{A},s}_{l,m}\rangle\langle\psi^{\mathrm{B},p_y}_{l,m+1}| + |\psi^{\mathrm{C},s}_{l,m}\rangle\langle\psi^{\mathrm{B},p_x}_{l+1,m}| \right) + \mathrm{h.c.} \tag{4.1}$$

We have used the s orbital energy in the small pillars as the reference energy, and the basis $\{|\psi^{J,\mu}_{l,m}\rangle\}$ of lattice sites that host a single orbital $\mu = s$ for the J = A and C pillars and a pair of orbitals $\mu \in \{p_x, p_y\}$ for the J = B pillars, with l, m labeling the unit-cell positions and t_{sp} the nearest-neighbors hopping amplitude. The diagonalization of the Hamiltonian in momentum space displays four different bands that cross at the center of the Brillouin zone, see Fig. 4.2(a). Each band is flat along one quasimomentum direction and dispersive along the perpendicular one.

The origin of this intriguing configuration is the directional coupling of the p_x and p_y modes of the large micropillars, displayed in Fig. 4.1(b). At B sites, the p_y orbitals only couple to the s modes of the A sites in the vertical direction, while the p_x orbitals couple only to the C sites in the horizontal direction. Therefore, the eigenmodes of this lattice are independent one-dimensional line modes along the vertical and horizontal lines of the lattice. The one-dimensional nature of the modes results in a band dispersion that is flat along one quasimomentum direction, which corresponds to the direction in real space perpendicular to the considered line. Along the other direction, the bands follow the typical dispersion of a one-dimensional lattice.

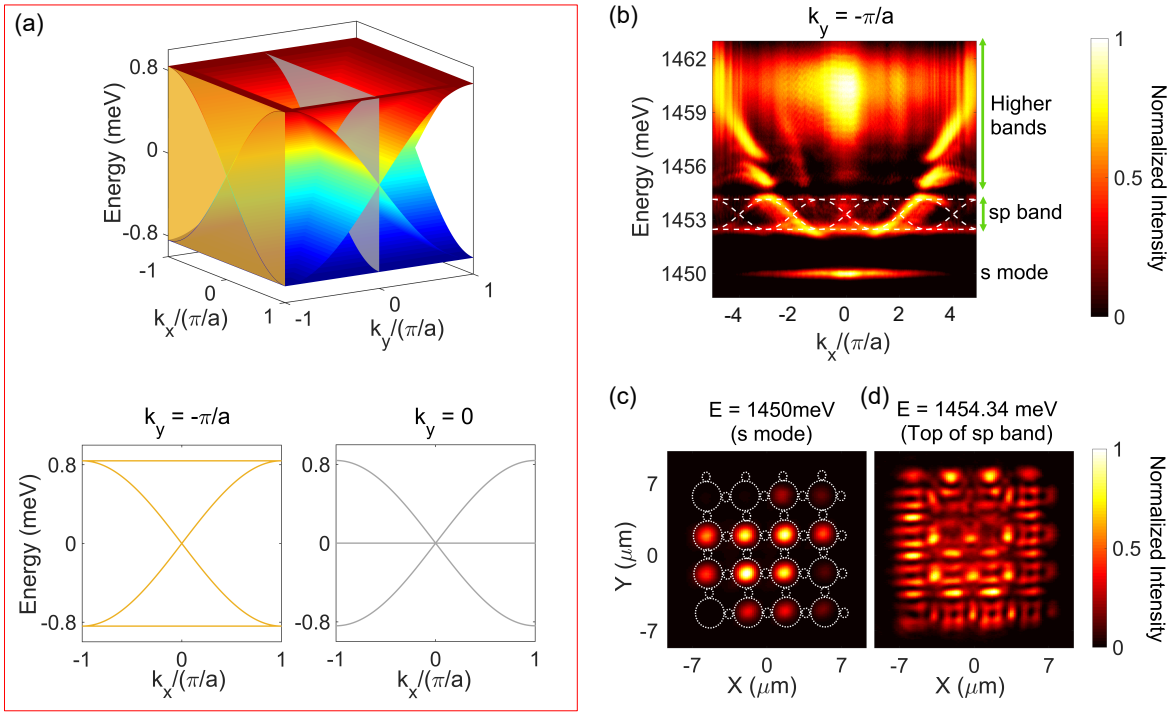

Figure 4.2: (a) Eigenvalues of the sp orbital bands computed from a tight binding model with nearest-neighbours. (b) Measured bands at $k_y = -\pi/a$ at low excitation power. Dashed lines display a fit to the eigenvalues of Eq. 4.1. (c) Real space emission measured at the energy of the s mode for a 4×4 lattice. (d) Real space emission measured at the energy of the top of the sp band.

The line eigenmodes and, correspondingly, the flat-dispersive bands in momentum space are the main difference with the s bands of a standard Lieb lattice made of identical micropillars at all sites. In that case, one of s bands is flat in both k_x and k_y directions, with corresponding plaquette states fully localised in a few unit cells (Fig. 4.3(b,c)). This situation is reported in [59, 60]. The p bands reported in those works are similar to the ones shown in Fig. 4.2: the eigenmodes are also line modes arising from the directionality of the p_x and p_y orbitals of the B sites (Fig. 4.3(b,d)). However, the spectrum presents an additional two-dimensional flat band arising from the p_x orbitals of the A sites and from the p_y orbitals of the C sites, which are not coupled to any other site. Therefore, they are fully localized at each of those sites (Fig. 4.3(b,e)). These highly localized modes dominate the lasing properties of the p bands, which was reported in [59, 60]. The main novelty of the design mixing s and p orbitals proposed in our work is that the line modes are separated in energy from other localized modes. This feature will be decisive for the observation of lasing in line modes.

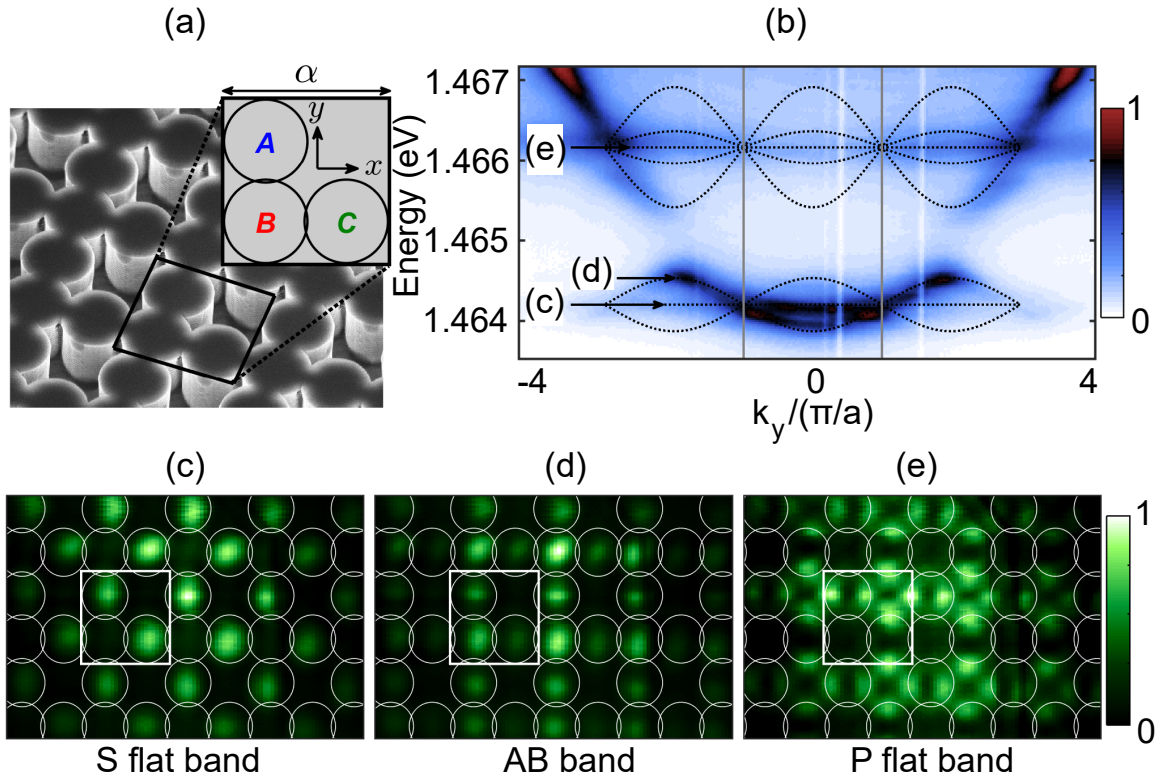

Figure 4.3: (a) Scanning electron microscope image of a section of the $2D$ Lieb lattice. (b) Lattice emission in energy-momentum space measured under low-power non-resonant excitation. (c)–(e) Emission in real space at the energies of the S flat band (c), the AB band maxima (d) and the P flat band (e). The white squares correspond to one unit cell as shown in (a) and the corresponding energies are shown by arrows in (b). Taken from [60].

Figure 4.2(b) displays the measured low-power photoluminescence of a sp Lieb lattice in momentum space as a function of k_x for $k_y = -\pi/a$. A large Gaussian spot at a wavelength of 820 nm is used for excitation. Emission from several bands is evidenced. The lowest energy one, fully flat, corresponds to the emission from

the s modes localized at each of the large B micropillars. This is confirmed in Fig. 4.2(c), which displays the real space photoluminescence at the energy of the s modes in a Lieb lattice with 4×4 unit cells. The two-dimensional real-space images are obtained using standard spectral tomography which spatially and spectrally resolves the photoluminescence of the lattice [59, 60, 189]. Well separated above the s modes, the sp set of bands is visible with flat bands at the bottom and top of the set for this specific measurement at $k_y = -\pi/a$. A fit of the eigenvalues of Eq. 4.1 to the measured sp bands in Fig. 4.2(b) – see dashed line – results in a value of t_{sp} = 0.42meV. The real-space emission at the energy of the top of the band is shown in Fig. 4.2(d), revealing its mixed s and p orbital structure. At even higher energy, other orbital bands are observed in Fig. 4.2(b).

4.2 Lasing in line modes

To study lasing action along different lines of the Lieb lattice, we consider a lattice with 4×4 unit cells. Since the eigenmodes of Lieb sp lattice are line modes, maximizing the modal overlap, and hence the gain required for lasing demands a line-shaped pump profile. Therefore, with the use of a cylindrical lens in combination with a regular short focal aspherical lens, we excite the lattice with an elongated Gaussian spot under non-resonant pumping along either the vertical/horizontal or both directions simultaneously. Energy-resolved photoluminescence is collected in the transmission geometry, as shown in Fig.4.4.

4.2.1 Experimental setup

Fig. 4.4 illustrates the experimental setup. The sample consists of a Lieb sp lattice placed inside a vacuum within a closed cycle helium cryostat and maintained at a temperature of 4K, as recorded in the sample holder. A narrow linewidth (<10MHz) single-mode Ti:Sapphire laser serves as the excitation source (wavelength 820nm). The beam is delivered through a single mode polarization maintaining optical fiber to ensure a high quality Gaussian spatial profile. After exiting the fiber, the beam power is regulated using a combination of a half-wave plate ($\lambda/2$) and a polarizing beam splitter (PBS), which together serve as a tunable power control unit. To generate two different excitation spots we divide the excitation beam in using a beamsplitter. Each arm is equipped with a cylindrical lens (focal length $f = 700\,\text{mm}$) to create elongated Gaussian spots independently in each arm. The beams are then recombined at a PBS, forming the final excitation profile. A portion of the beam is diverted by a beam splitter (BS) for power monitoring, while the rest is directed toward the sample for excitation. The measurements are carried out in a transmission geometry: the excitation beams enter the sample through the epitaxial side, propagate through the substrate, and exit via a 3mm slit in the sample holder before reaching the collection optics. Both excitation and

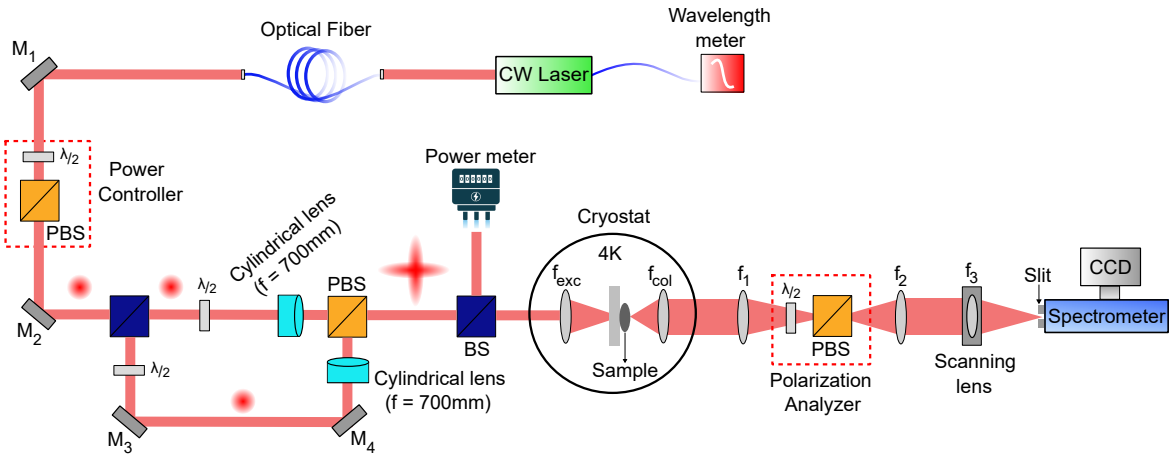

Figure 4.4: Scheme of the experimental setup illustrating the excitation of the Lieb sp lattice and real space imaging of polariton photoluminescence (PL). Abbreviations: $\frac{\lambda}{2}$ - half-wave retarder, PBS - polarized beam splitter, BS - beam splitter. Lenses: f_{exc}, f_{col} = 8 mm, f_1 = 300 mm, f_2 = 150 mm and f_3 = 500 mm.

detection optics employ aspheric lenses (f_{exc}, f_{col}) with a numerical aperture of 0.5. It is worth noting that the GaAs substrate exhibits negligible absorption at the operating wavelength allowing efficient light transmission. The photoluminescence emitted from the sample is first magnified using a telescope composed of two lenses with focal lengths f_1 and f_2. Following this, the beam passes through a polarization analysis setup consisting of a half-wave plate ($\lambda/2$) and a polarizing beam splitter (PBS).The transmitted light is then collected by a lens (f_3) and directed either to a CCD camera for imaging or to a spectrometer for spectral analysis. The lens (f_3) is mounted on a movable stage that can be scanned laterally to perform $2D$ tomography in real and fourier space. For Fourier space imaging, an additional lens is inserted between the telescope and the scanning lens.

4.2.2 Horizontal pumping

To investigate lasing along the horizontal line of the Lieb lattice, we excite the system with a horizontally elongated Gaussian spot. The spot, generated with a cylindrical and an aspherical lens (8 mm focal length), has full widths at half maxima of 2.5μm vertically and 18μm horizontally. The spot is located at the center of one of the bulk lines of the lattice, sketched in Fig. 4.5(a) for an horizontal line excitation.

At low excitation power, Fig. 4.5(d), we observe emission from the s modes at 1450 meV, the sp bands in the range 1452.22-1454.34 meV and other orbital bands at higher energy. Figure 4.5(e) shows that at the energy of the top of the sp bands, the emission is spread throughout the lattice. When the excitation power is increased, the emitted intensity at the energy of the top mode of the sp band displays a lasing threshold at about 10 mW of input power (see Fig. 4.5(b)). The spectrum above

threshold is displayed in Fig. 4.5(f): it shows narrow linewidth laser emission from the top of the *sp* band at about 1454.5 meV (linewidth $\sim$ 60 μeV, which is the spectrometer resolution), and from the isolated *s* modes of the B pillars under the excitation spot, each of them emitting at slightly different energies. The real-space emission at the energy of the lasing *sp* mode displayed in Fig. 4.5(g) reveals the antibonding nature of the modes, with nodes at the junctions between the *s* and *p* lobes. Remarkably, this laser mode is constrained to a single line and presents coherent emission all over its length.

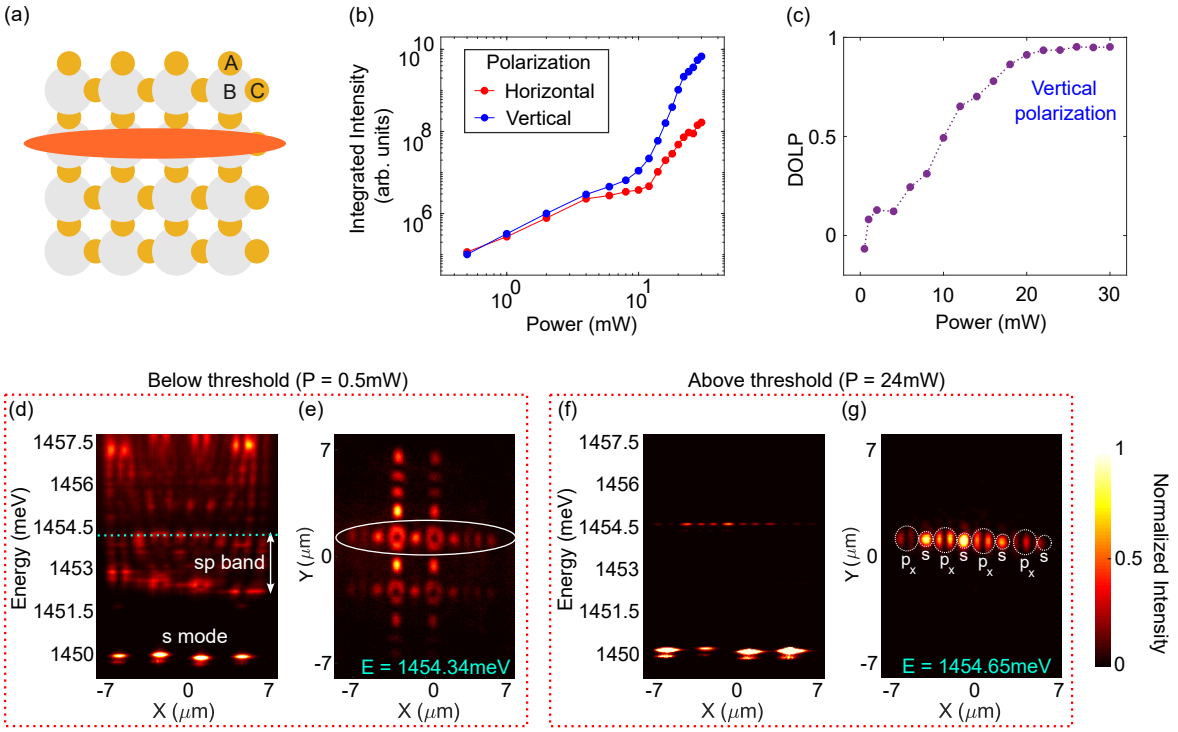

Figure 4.5: Sketch of the configuration for the excitation of an horizontal line of the lattice. (b) Integrated intensity of the upper *sp* mode along the line in which the lattice is excited. The intensity is resolved in linear polarization. (c) Degree of linear polarization computed from (b). (d) Emitted spectrum along a line crossing the center of the excitation spot at low excitation power (0.5 mW). (e) Real-space photoluminescence at the energy of the top of the *sp* band. (f)-(g) Same as (d)-(e) at an excitation power above the lasing threshold.

The observed blueshift between the top of the *sp* bands at low power (Fig. 4.5(d), dashed line) and the lasing mode above threshold (Fig. 4.5(f)) arises from the loss of strong coupling at high powers. Indeed, at the low temperatures of the experiments, the exciton resonance of the quantum well at 1460.4 meV and the photonic bands are in strong light-matter coupling, with a characteristic Rabi splitting of about 3.5 meV [190]. At low power, the strong coupling shifts down the energy of the upper *sp* modes by about 0.3 meV with respect to the bare photonic modes. At high excitation power, at which *sp* lasing takes place, phase-space filling effects provoke the loss of strong coupling and lasing takes place at the energy of the bare photonic modes [191]. The loss of strong coupling along the excited line and

the corresponding blueshift introduce a lateral confinement that pushes the line emission into the gap, and facilitates decoupling from other lattice modes.

The onset of lasing is accompanied by the appearance of a significant degree of linear polarization with vertical orientation (perpendicular to the line geometry). The degree of linear polarization (DOLP) is defined as

$$\mathrm{DOLP} = \frac{I_\mathrm{V} - I_\mathrm{H}}{I_\mathrm{V} + I_\mathrm{H}}, \tag{4.2}$$

where I_H and I_V are the emission intensities obtained by projecting onto the horizontal and vertical linear polarization bases with a polarimetric analyzer ($\lambda/2$ and a PBS; see Fig. 4.4). Above threshold, the DOLP remains constant and very close to 1, see Fig. 4.5(c). Similar results are observed for an excitation spot aligned along any other of the horizontal and vertical lines of the orbital Lieb lattice.

4.2.3 Vertical pumping

An example of lasing under excitation along a vertical line is shown in Fig. 4.6(b). In this case, the lasing emission is polarized in the horizontal direction (perpendicular to the excited line, see Figs. 4.6(c)-(d)), which is consistent with the observations of Fig. 4.5.

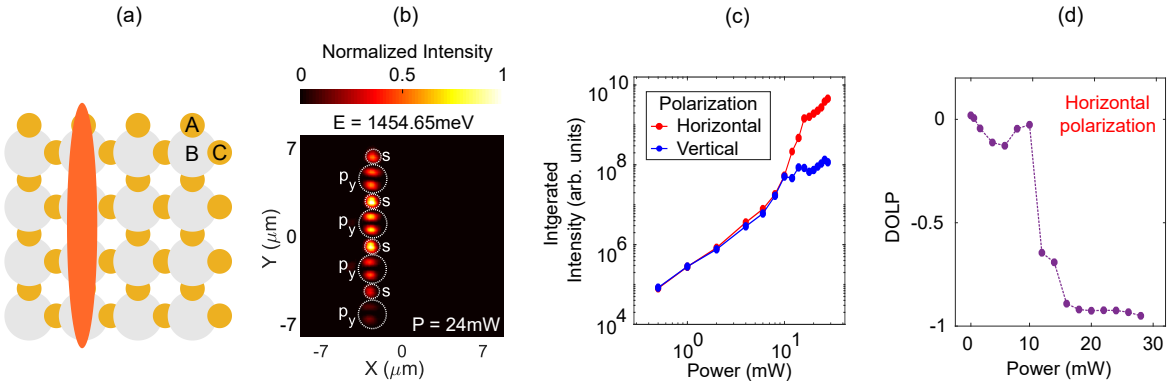

Figure 4.6: Sketch of the excitation configuration of a vertical line of the lattice. (b) Real-space emission at the energy of the *sp* lasing mode above threshold. (c) Integrated intensity of the upper *sp* mode along the line in which the lattice is excited. The intensity is resolved in linear polarization. (d) Degree of linear polarization computed from (c).

The reason for the lasing mode to select a linear polarization perpendicular to the lasing line is related to the local blueshift created by the loss of strong coupling under the excitation spot. The local blueshift of the excited line into the gap induces a lateral photonic confinement. This confinement results in the splitting of modes with linear polarizations along and perpendicular to the line due to the polarization dependent penetration of the photonic field at the sides of the confined line. As the lateral spread of the line modes depends on their linear polarization,

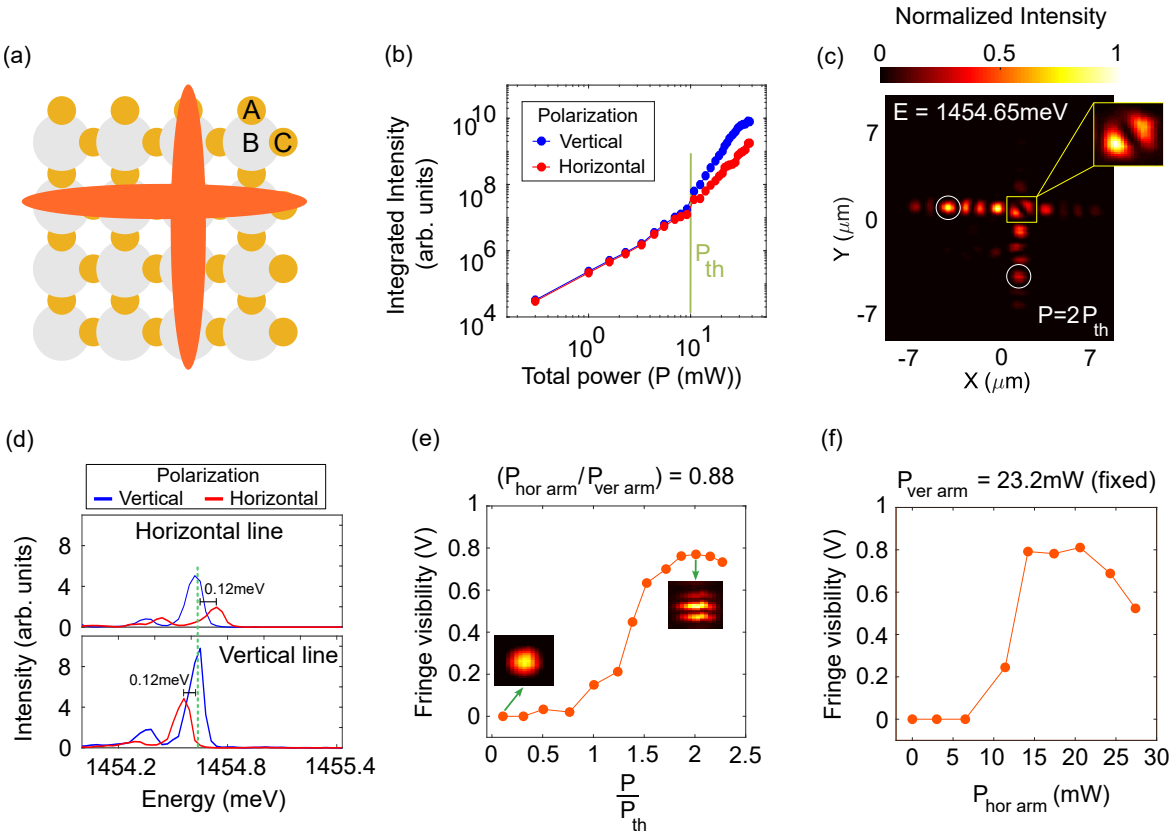

Figure 4.7: (a) Scheme of the crossed excitation spot along a vertical and a horizontal line. (b) Integrated intensity of the top of the sp band integrated over the sites along the lines in which the lattice is excited. (c) Measured laser emission at the energy of the sp lasing mode above threshold ($P = 2P_{th}$). The inset shows a zoomed view of the micropillar at which the two lines cross. (d) Measured spectrum resolved in linear polarization at $P = 1.2P_{th}$ for photon energies at the top of sp band at two different spatial points corresponding to the circles in the horizontal and vertical arms in (c). (e) Visibility of the fringes arising from the interference between the two circled sites in (c) when they are overlapped on a CCD camera. Insets show the overlapped images at low and high power. (f) Same as (e) when the power of the vertical excitation spot is kept at 23.2 mW and the power of the horizontal excitation spot is varied.

modes with different polarizations may couple differently to the excitation spot and have different gains (more details on this will be provided in the upcoming sections).

4.3 Phase locking of crossing laser modes

To further demonstrate the versatility of the orbital Lieb lattice to engineer intricate laser modes, we study the possibility of implementing a laser mode in the form of two crossing lines. To do so, we engineer two identical elongated excitation spots that cross at a large diameter micropillar at a B site; see scheme in Fig. 4.7(a).

To avoid interference effects at the crossing site, the two excitation spots have perpendicular linear polarizations.

Figure 4.7(b) displays the emission measured at the energy of the top of the sp band integrated spatially across the two excited lines when the total excitation power increases. The intensity of the horizontal pump spot is 0.88 times that of the vertical spot (the specific choice of this value will be explained later in the following section). We observe a lasing threshold P_{th} of 10mW, with dominating emission in vertical polarization. Figure 4.7(c) displays the measured spatial pattern of the laser emission at $2P_{th}$: it shows lasing in the form of a cross under the excitation spots. The two crossing lasing lines emit at the same photon energy, are phase-locked and share the same polarization (vertical).

Let us first characterize the observed energy and phase locking of the two lines. This locking is clearly evidenced in the inset of Fig. 4.7(c), which displays a zoom of the B pillar at which the two lines cross. The intensity pattern with diagonal lobes corresponds to the specific linear combination of $|p_x\rangle + |p_y\rangle$ modes. A random relative phase between the two lasing modes or a difference in energy would result in the averaging of many different relative phases between the p_x and p_y lobes in our time integrated experiments, and the pattern at the crossing micropillar would rather show a ring-like shape (indicated by a white arrow in Fig. 4.8(c)). Such a ring-like pattern is actually observed in the low power regime of spontaneous emission.

4.3.1 Fringe Visibility - Interference experiment

As an additional proof of the energy and phase locking between the lasers, we study the interference pattern when the emission from the two circled micropillars in Fig. 4.7(c) is overlapped in a CCD camera using a set of beamsplitters and mirrors (see Fig. 4.8(a)).

Fig. 4.8(a) shows the interferometer configuration using three mirrors, with mirror M_6 mounted on a kinematic stage for fine adjustment. This allows precise control of the optical path length to achieve near zero delay between the two arms, which is essential for observing interference and verifying phase coherence between the modes. Figure 4.8(b) illustrates the schematic of the interference process. One arm of the interferometer captures the direct image of the emission, while the other arm produces a spatially displaced and mirror-flipped version of the same image. This configuration allows the two images to overlap and interfere. Figure 4.8(c) - left panel - shows the initial image below threshold. Emission is spread over several lines in the lattice. At the crossing site of the two pump spots (see arrow), we observe a ring like emission. This ring pattern is characteristic of the random phase between the p_x and p_y orbitals in the spontaneous emission re-

gime below threshold. The white circles on the left and central images of Fig. 4.8(c) highlight the spatial regions where the *s*-orbital modes from the two orthogonal lines are made to interfere in the right panel. The absence of interference fringes witnesses the absence of phase locking in the spontaneous emission regime at $P/P_{th} = 0.1$. Above threshold ($P/P_{th} = 2$), Fig. 4.8(d) shows the emergence of interference fringes, clearly visible in the inset of the right panel, indicating phase locking.

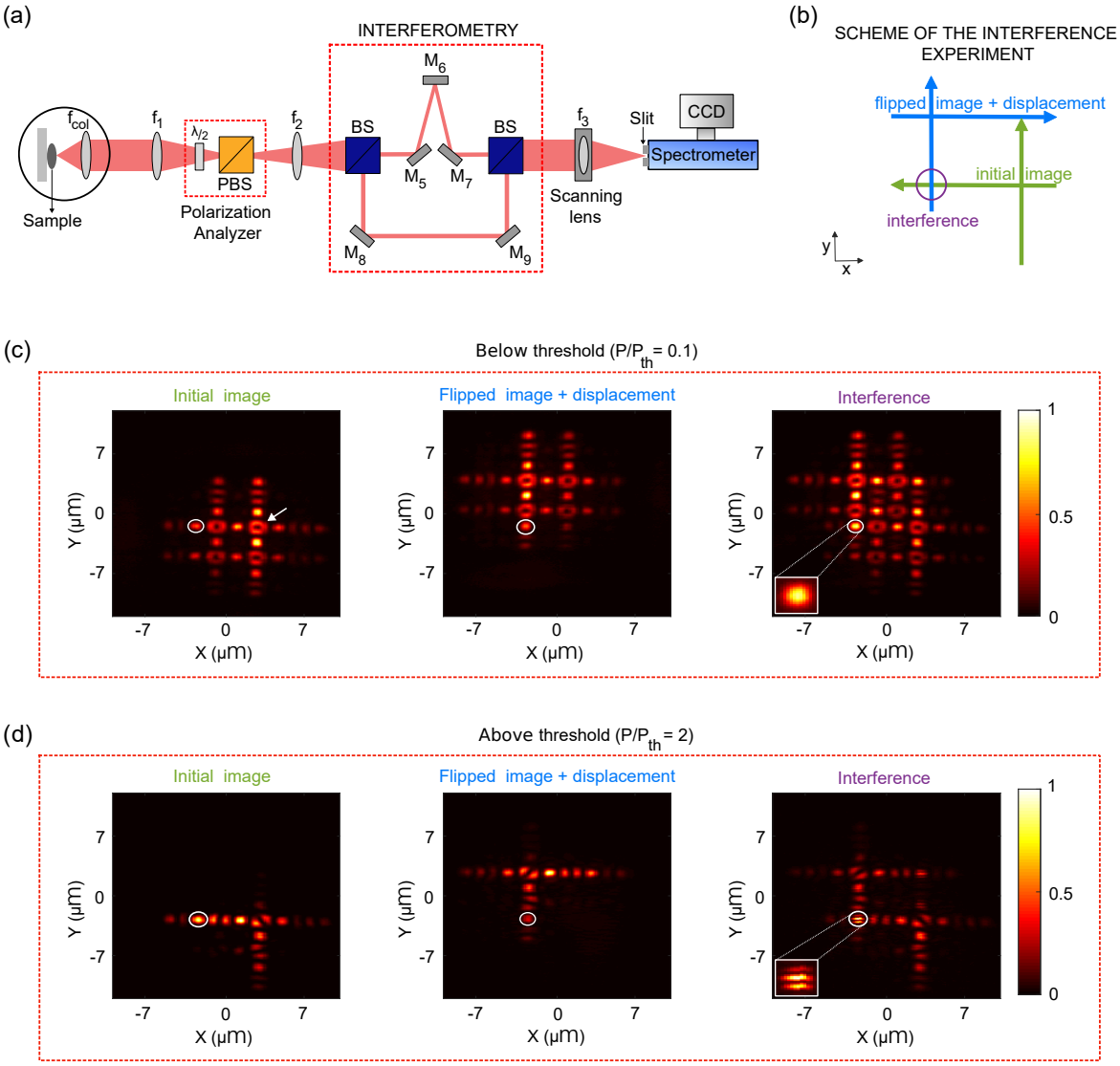

Figure 4.8: (a) Schematic of the experimental setup for the interferometry. (b) Illustration of the interference procedure: the initial image is flipped and spatially displaced then recombined to produce the interference pattern. (c) Interferogram recorded below threshold power, where no interference is observed (shown as an inset). (d) Interferogram recorded above the threshold power, revealing clear interference fringes (shown as an inset).

Figure 4.7(e) shows the measured visibility of the interference fringes of the overlapping spots as a function of the total pump power which is defined as:

$$\text{visibility} = \frac{I_{\max} - I_{\min}}{I_{\max} + I_{\min}}, \tag{4.3}$$

where $I_{\max}$ and $I_{\min}$ are the maxima and minima intensities around the central interference peak. At low power, in the spontaneous emission regime (see the inset at $P/P_{th} = 0.1$) no fringes are observed in the two overlapping spots in the CCD, resulting in visibility close to zero. At high power, the observation of deep stable fringes with high visibility (see the inset at $P/P_{th} = 2$) in our continuous wave experiment with integration times of the order of several seconds confirms the robust energy and phase locking of the two lasing energy lines.

4.3.2 Polarization locking

We now address the conditions for polarization locking in the cross line laser. Figure 4.7(d) displays the measured spectrum resolved in linear polarization at $P = 1.2P_{th}$ for photon energies at the top of sp band. The measurements are done at two different spatial points corresponding to the circles in the horizontal and vertical arms in Fig. 4.7(c). For the horizontal line, the top of the sp band is split into modes with perpendicular linear polarizations. As discussed above for a single line excitation, the origin of this splitting is related to the blueshift of the lasing line at high excitation powers. The top panel of Fig. 4.7(d) explicitly shows this splitting. The majority of the emission is in the lasing mode with vertical polarization (blue line in Fig. 4.7(d)), which emits at lower energy than the horizontal polarization (red line). Note that, at higher pump powers, the vertically polarized intensity largely overwhelms the horizontally polarized emission. If we now focus on the spectra emitted by the vertical line, we observe the same hierarchy of splittings but now rotated by 90°: the majority of the emission is also in the vertical polarization (blue line), but now this mode is at higher energy than the horizontally polarized emission (red line). The splitting is 0.12 meV in both lines.

We therefore see that the blueshifts induced by the loss of strong coupling under the pump spots result in the splitting of the polarization in the vertical and horizontal lines and are such that the vertically polarized modes have the same photon energy in both lines. To achieve this energy resonance, each arm requires a different blueshift, which in turn requires different pump powers. Note that the energy of the lasing horizontal line in Fig. 4.7(d) is higher than the one of the vertical line. This feature indicates that in the horizontal line more carriers are injected than in the vertical one because the blueshift is proportional to the local carrier density. However, the measured excitation power before the sample was stronger in the vertical arm than in the horizontal arm ($P_{\text{hor arm}} = 0.88P_{\text{ver arm}}$). This discrep-

ancy may be caused by deviations from perfect alignment of the two pump spots, which resulted in a worse line overlap for the vertical spot.

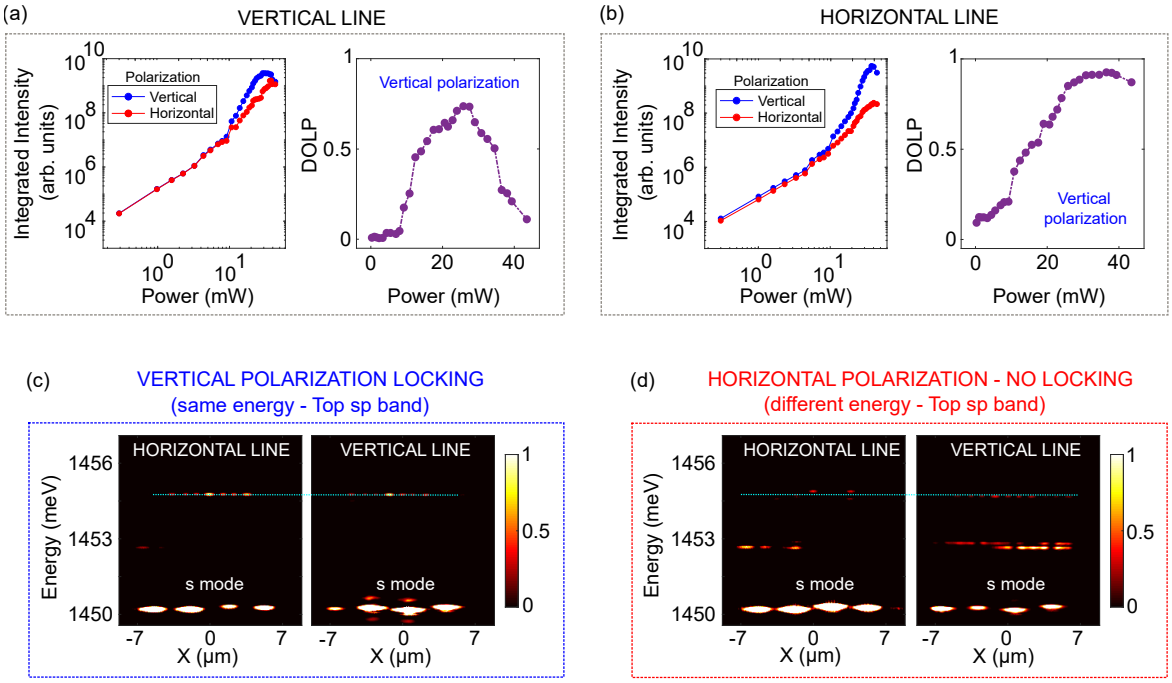

Figure 4.9: (a) Integrated intensity of the upper sp mode along the vertical line for a cross pumping configuration in which the lattice is excited. The intensity is resolved in linear polarization and the Degree of linear polarization (DOLP) is computed from the integrated intensity. b) Integrated intensity of the upper sp mode along the horizontal line for a cross pumping configuration in which the lattice is excited. The intensity is resolved in linear polarization and the Degree of linear polarization (DOLP) is computed from the integrated intensity. c) Polarization locking observed due to the degeneracy of the top sp band for both the vertical and horizontal line. d) Absence of polarization locking, attributed to the energy difference between the top sp bands along the vertical and horizontal line.

To provide additional experimental details on the polarization resolved emission for the crossed lines excitation, we focus on the conditions described for the crossed lines excitation of a 4×4 lattice reported in Fig. 4.7(b,d). Figures 4.9(a) and (b) display the polarization resolved emission integrated spatially over each of excited lines (vertical line in (a), horizontal line in (b)) at the energy of the top of the *sp* bands. The horizontal axis corresponds to the total excitation power (sum of the power of the two spots). Above threshold, the degree of linear vertical polarization is high for both lines. It is important to note that cross-locking is obtained only within a finite pump-power window where lasing occurs at the top of *sp* band. At higher powers, additional modes build up and compete, reducing the value of DOLP for the vertical line (beyond 27mW in Fig. 4.9(a)).

In Fig. 4.7(d), analysis of blueshift was done at $P/P_{th} = 1.2$. As an additional proof, Figure 4.9(c) shows the energy spectra of the emission along the vertical and

horizontal lasing lines with the analyzer in the vertical linear polarization position, which corresponds to the polarization of the laser emission, for an excitation power well above threshold ($P/P_{th} = 1.6$). The laser emission energy in this polarization for the modes at the top of the sp bands is identical up to our spectral resolution (dashed line). Figure 4.9(d) shows the energy spectra of the emission with opposite polarization (horizontal), for the two lasing lines. Emission from the top mode of sp band is weaker but still visible. However, it does not happen at the energy of the vertical polarization emission of the lasing mode in Fig. 4.9(c). Each line of the lattice emits horizontally polarized light at the top mode of sp band at different energies. This polarization behavior is displayed in Fig. 4.7(d). It shows that different blueshifts on each line are required for polarization alignment and locking of the lasing mode.

To get deeper insights into the energy, phase and polarization locking between the two laser lines, we have tested the resilience of the fringe visibility to asymmetries in the excitation power of the two lines. To do so, we increase the power of horizontal excitation spot while the power of the vertical spot is kept at 23.2 mW. The measured fringe visibility is plotted in Fig. 4.7(f). Only when the two arms have similar powers the fringe visibility is high, witnessing locking between the two lasers.

4.4 Line lasing in a 10 × 10 lattice

The experimental results shown in the previous sections were presented for a 4 × 4 lattice configuration. To demonstrate that the observed line lasing behavior and polarization locking phenomena are not specific to the system size and not a consequence of edge effects, here we present measurements performed on a larger 10 × 10 lattice etched in the same microcavity wafer. Real space imaging of polariton photoluminescence was performed at the top of the sp band under a horizontally elongated excitation spot. All panels in Fig. 4.10(a) were taken above the lasing threshold, with a pump power of 35 mW. The emission was recorded for four linear output polarization angles: 135°, 0°, 45°, and 90°, corresponding to distinct analyzer orientations. In Fig. 4.10(b), a similar set of measurements was carried out using a vertically elongated excitation spot, also pumped above threshold at 35 mW. Real space images were recorded under the same set of output polarization angles (135°, 0°, 45°, and 90°). In the cross-pump excitation configuration as shown in Fig. 4.10(c), real space emission was again recorded under the four linear analyzer angles at a combined total power of 71 mW.

To extract the orientation of linear polarization from the measured photoluminescence for above three cases, intensities obtained by integrating the PL signal along a fixed energy (top of sp band) is calculated at four linear polarization ana-

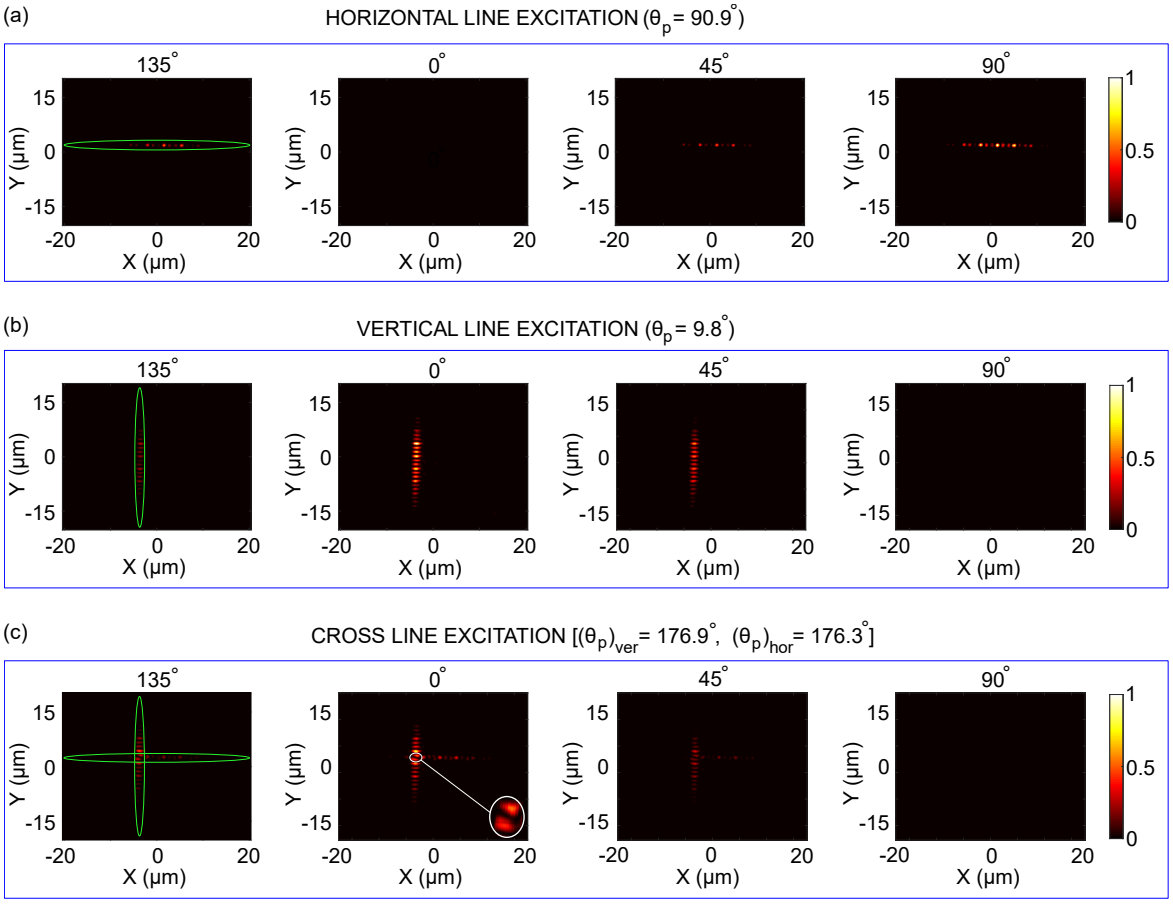

Figure 4.10: Real space photoluminescence (PL) images analyzed at four output polarization angles: 135°, 0°, 45°, and 90°, using a polarization analyzer consisting of a half-wave plate and linear polarizer. (a) PL from the horizontal line with horizontal spot excitation at P = 35mW. (b) PL from the vertical line with vertical spot excitation at P = 35mW. (c) PL under cross pumping excitation with a total power of 71mW. All images are extracted at a fixed energy slice (top sp band).

lyzer angles: 135°, 0°, 45°, and 90° respectively. The Stokes parameters S_0, S_1, and S_2 were calculated using the following relations:

$$S_0 = I_{0^\circ} + I_{90^\circ} \tag{4.4}$$

$$S_1 = I_{0^\circ} - I_{90^\circ} \tag{4.5}$$

$$S_2 = I_{45^\circ} - I_{135^\circ} \tag{4.6}$$

$$S_3 = 0 \quad \text{(assuming negligible circular polarization)} \tag{4.7}$$

The angle of linear polarization is calculated using:

$$\theta_p = \frac{1}{2}\tan^{-1}\left(\frac{S_2}{S_1}\right) \tag{4.8}$$

The computed angle θ_p gives the polarization of the line lasing mode. For horizontal excitation, $\theta_p = 90.9^\circ$ (vertical polarization), while for vertical excita-

tion, $\theta_p = 9.8^\circ$(horizontal polarization). Under cross-pump conditions, the vertical line yields $(\theta_p)_{\text{ver}} = 176.9^\circ$ (horizontally polarized) and the horizontal line gives $(\theta_p)_{\text{hor}} = 176.3^\circ$ (horizontally polarized). These results confirm that the two line modes are both phase (as shown in the inset of Fig. 4.10(c)) and polarization locked, consistent with the behavior observed in the 4×4 lattice. Note that the power arrangement between the two pump spots in a 4×4 lattice resulted in vertical polarization locking. In the experiment displayed in Fig. 4.10 for a 10×10 lattice the two spots have slightly different powers ($P_{horarm} = 38$ mW and $P_{verarm} = 33$ mW) such that the local blueshifts result in an energy resonance of modes with horizontal polarization.

4.5 Summary

In this chapter, to realize line-like eigenmodes, we engineered the band dispersion of the Lieb *sp* lattice by coupling orbital modes of overlapping pillars with different diameters. By aligning the non-resonant pump of line like spatial profile with these eigenmodes, line lasing along both the horizontal and vertical axes is achieved; each line exhibiting a distinct polarization and thus operating as an independent laser. However, under a cross-shaped excitation, the two orthogonal line lasers lase simultaneously, and a single polarization component becomes energy- and phase locked, indicating coupling between the lines. Polarization-resolved measurements show that different blueshifts between lines are required to align the lasing-mode polarizations, showcasing the origin of polarization locking. However, the mechanism responsible for phase locking remains open and will be addressed numerically in the next chapter, where we identify what creates the orthogonal line lasers to phase lock.

5

NUMERICAL MODELING OF PHASELOCKING

In the previous chapter, an experimental demonstration of phase locking between two orthogonal line lasers was established under a non-resonant cross-pumping configuration in the Lieb *sp* lattice. However, the physical origin of this locking remained unclear. This chapter addresses that question by developing a driven–dissipative lattice-lasing model in which a scalar photon field evolves under a tight-binding Hamiltonian coupled at each site to an electron–hole reservoir via rate equations, where the pump is applied in the form of discretized gaussian profiles at desired sites. We neglect the polarization degree of freedom and consider scalar fields in the simulations. Incorporating polarization into the model is straightforward in principle, but would significantly increase the number of parameters to be fitted. Although this represents a substantial simplification, it is not required to capture the physics of phase locking. With this we identify the minimal set of terms needed in the Hamiltonian to explain how cross-pumping drives the lattice in achieving stable phase locking with maximal emission from the two lines.

5.1 Eigen modes of 4 × 4 lattice

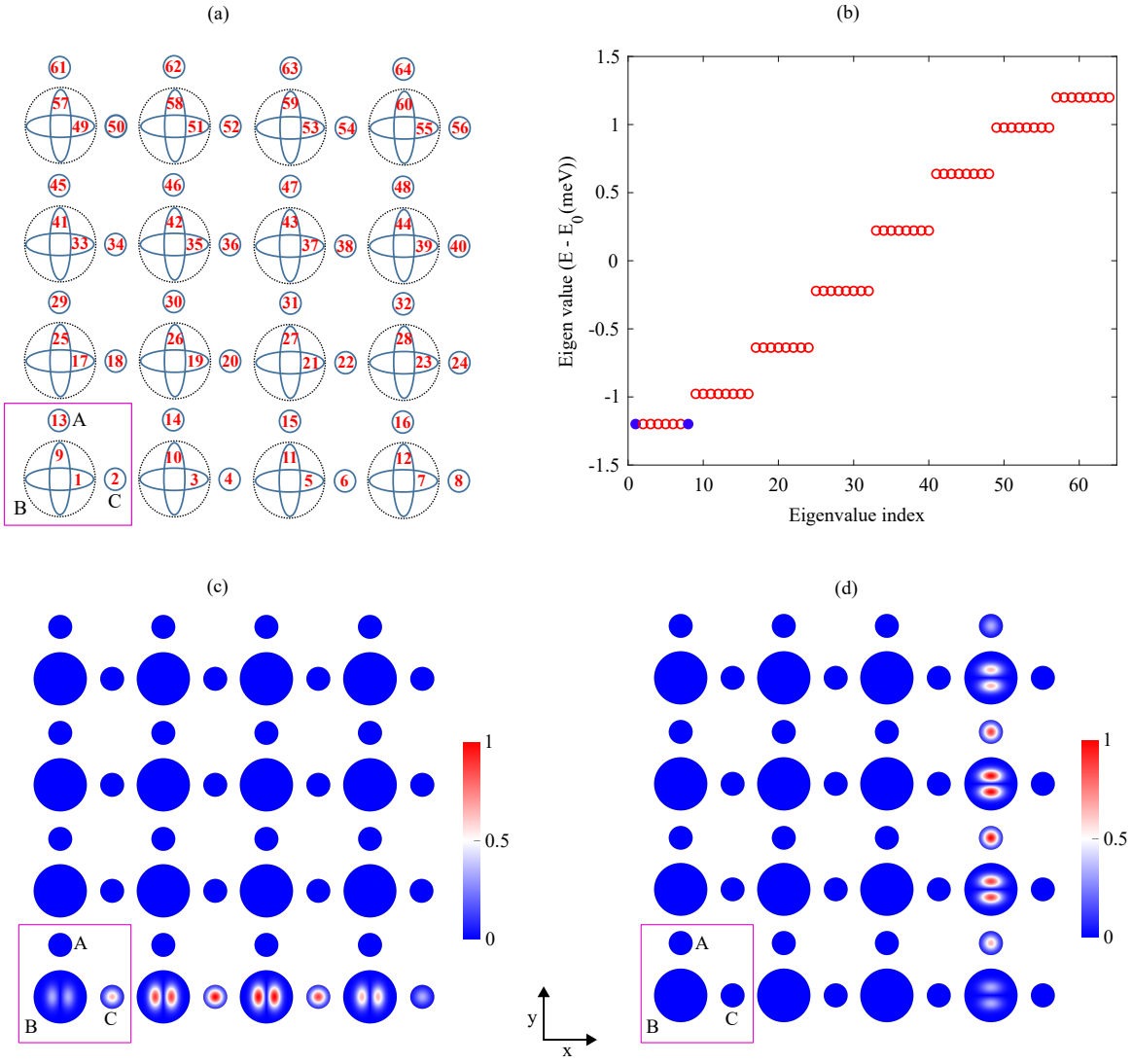

Figure 5.1: (a) Schematics of the mode index used in the simulation. (b) Eigen values of the diagonalized Hamiltonian with blue circles (indices 1 and 8) representing the two different eigen modes from the same degenerate energy. (c) The real space intensity profile for the eigenmode indexed 1 and (d) indexed 8 which were marked as blue circles in (b).

In the previous chapter, the experimental results of line lasing and phase locking between orthogonal lines in a Lieb sp lattice were discussed. Here, we turn to numerical modeling of the same lattice in the tight-binding limit. For visualization, let's explicitly number the sites mode index as illustrated in Fig. 5.1(a). The lattice consists of 4×4 unit cells, resulting in 64 assigned mode indices. Sites with cross-shaped geometry (B - indicated by lobes in both horizontal and vertical directions) support two orbitals p_x and p_y that co-exist within a single micropillar as orthogonal spatial modes. In contrast, circular sites (A and C) without lobes correspond to s-like modes. The corresponding Hamiltonian, constructed based on the indexed modes, includes nearest-neighbor couplings via a hopping parameter

$t = 0.42$meV, which is extracted from the white line fit in Fig. 4.2(b). Diagonalizing the tight-binding Hamiltonian with the $s - p_x$ and $s - p_y$ couplings, the resulting eigenvalue plot is shown in Fig. 5.1(b), which exhibits eight distinct eigenenergies, each eightfold degenerate, reflecting the eight independent line modes in each energy. The eigenvalues in Fig. 5.1(b) are ordered by energy: indices 1 to 8 form the lowest energy (bonding - all pillars are in phase), while 57 to 64 correspond to the highest energy (antibonding - featuring π phase difference between adjacent pillars). To visualize the eigenmodes in real space, we assign spatial profiles to each orbital type: p_x and p_y orbitals are represented by antisymmetric Gaussian lobes; s orbitals are represented by symmetric Gaussian spots in the small pillars. Fig. 5.1(c,d) presents the real-space intensity profiles for two degenerate eigenmodes (indices 1 and 8) within the bonding energy, but they are $1D$ independent lines as written in matrix form in Eq. 5.3.

To understand how each line is a unique matrix, we begin by considering a single one-dimensional tight-binding chain with $N = 8$ sites and nearest-neighbour hopping amplitude $-t$. Labeling the sites of this chain by $\{|1\rangle, \ldots, |8\rangle\}$ and defining it's Hamiltonian as

$$H = -t \sum_{j=1}^{7} \left(|j\rangle\langle j+1| + |j+1\rangle\langle j| \right). \tag{5.1}$$

In the site basis $\{|1\rangle, \ldots, |8\rangle\}$, the matrix representation of H is the 8×8 tridiagonal matrix

$$\mathbf{T}_8 = \begin{pmatrix} 0 & -t & 0 & 0 & 0 & 0 & 0 & 0 \\ -t & 0 & -t & 0 & 0 & 0 & 0 & 0 \\ 0 & -t & 0 & -t & 0 & 0 & 0 & 0 \\ 0 & 0 & -t & 0 & -t & 0 & 0 & 0 \\ 0 & 0 & 0 & -t & 0 & -t & 0 & 0 \\ 0 & 0 & 0 & 0 & -t & 0 & -t & 0 \\ 0 & 0 & 0 & 0 & 0 & -t & 0 & -t \\ 0 & 0 & 0 & 0 & 0 & 0 & -t & 0 \end{pmatrix}. \tag{5.2}$$

For the Lieb sp lattice in a 4×4 unit cell, the coupling are the same as for the $1D$ discussed above, such that the tight-binding Hamiltonian can be decomposed into eight independent one-dimensional chains of this form: four horizontal lines and four vertical lines. As there is no coupling between different lines the H_{sp} matrix can be represented as a block diagonal, with one 8×8 block $\mathbf{T}_8$ for each chain and zeros elsewhere:

$$\mathbf{H}_{sp} = \begin{pmatrix} \mathbf{T}_8 & \mathbf{0} & \mathbf{0} & \mathbf{0} & \mathbf{0} & \mathbf{0} & \mathbf{0} & \mathbf{0} \\ \mathbf{0} & \mathbf{T}_8 & \mathbf{0} & \mathbf{0} & \mathbf{0} & \mathbf{0} & \mathbf{0} & \mathbf{0} \\ \mathbf{0} & \mathbf{0} & \mathbf{T}_8 & \mathbf{0} & \mathbf{0} & \mathbf{0} & \mathbf{0} & \mathbf{0} \\ \mathbf{0} & \mathbf{0} & \mathbf{0} & \mathbf{T}_8 & \mathbf{0} & \mathbf{0} & \mathbf{0} & \mathbf{0} \\ \mathbf{0} & \mathbf{0} & \mathbf{0} & \mathbf{0} & \mathbf{T}_8 & \mathbf{0} & \mathbf{0} & \mathbf{0} \\ \mathbf{0} & \mathbf{0} & \mathbf{0} & \mathbf{0} & \mathbf{0} & \mathbf{T}_8 & \mathbf{0} & \mathbf{0} \\ \mathbf{0} & \mathbf{0} & \mathbf{0} & \mathbf{0} & \mathbf{0} & \mathbf{0} & \mathbf{T}_8 & \mathbf{0} \\ \mathbf{0} & \mathbf{0} & \mathbf{0} & \mathbf{0} & \mathbf{0} & \mathbf{0} & \mathbf{0} & \mathbf{T}_8 \end{pmatrix}_{64\times 64} \tag{5.3}$$

where the first block of T_8 in Eq. 5.3 corresponds to the sites $1-8$ labeled in Fig. 5.1(a); the remaining seven blocks of T_8 map to the other lines according to the numbering in Fig. 5.1(a).

5.2 Modeling of driven-dissipative lattice lasing modes

With the eigenvalues and eigenmodes established for a Lieb sp lattice of a 4×4 unit cell in the last section, we proceed to model the driven–dissipative lattice. To simplify the analysis in modeling, we neglect the polarization degree of freedom and consider scalar fields. While this simplification is significant, it provides relevant insights on the conditions for phase locking. Adding polarization to the model does not constitute a major difficulty but implies a higher number of fitting parameters. We focus on the sp bands and ignore lasing in the s modes of the B pillars, which was systematically observed along lasing in the line modes of the sp bands in the experiment. The time evolution of the scalar photon field $\{|\psi^{J,\mu}_{l,m}\rangle\}$ at unit cell l,m, site $J = A,B,C$ and orbital $\mu = s,p_x,p_y$ is governed by the following differential equation [192]:

$$i\hbar\frac{d}{dt}|\psi^{\mathrm{J},\mu}_{l,m}\rangle = \left(H_{\mathrm{sp}} - i\frac{\Gamma_p}{2} + i\frac{\Gamma_d}{2}n^J_{l,m}\right)|\psi^{\mathrm{J},\mu}_{l,m}\rangle + \frac{\sqrt{n^{\mathrm{J}}_{l,m}}}{2}\Gamma_d e^{i\phi^{\mathrm{J},\mu}_{l,m}(t)} \tag{5.4}$$

H_{sp} is the tight-binding Hamiltonian in Eq. 4.1. $\Gamma_p = 62.5\,\mu$eV is the decay rate via escape of photons from the cavity. This value is estimated from an independent measurement of the photon lifetime on a one-dimensional lattice in the same wafer [193]. The next term in Eq. 5.4 involve the coupling of the photon field to an exciton reservoir fed by the pump laser. Γ_d is the stimulated scattering rate from the reservoir to the photon field. The last term is a source term that accounts for spontaneous stochastic scattering from the reservoir, in which $\phi^{\mathrm{J},\mu}_{l,m}(t)$ is a random phase uniformly distributed in $[0,2\pi)$ and serves as a seed for lasing.

The photon field is coupled to the exciton reservoir $n^{\mathrm{J}}_{l,m}$ (active gain medium) at each site l, m pumped by the external laser. The p_x and p_y modes of the B sites share a common reservoir whose dynamics is given by:

$$\hbar \frac{dn^{\mathrm{B}}_{l,m}}{dt} = 2P^{\mathrm{B}}_{l,m} - \Gamma_e n^{\mathrm{B}}_{l,m} - \Gamma_d n^{\mathrm{B}}_{l,m} \left(|\psi^{\mathrm{B},p_x}_{l,m}|^2 + 1 + |\psi^{\mathrm{B},p_y}_{l,m}|^2 + 1 \right). \tag{5.5}$$

The $\hbar$ prefactor on the left hand side has been added for consistency of units. The s modes in the A and C micropillars have individual reservoirs:

$$\hbar \frac{dn^{\mathrm{J}}_{l,m}}{dt} = P^{\mathrm{J}}_{l,m} - \Gamma_e n^{\mathrm{J}}_{l,m} - \Gamma_d n^{\mathrm{J}}_{l,m} \left(|\psi^{\mathrm{J},s}_{l,m}|^2 + 1 \right). \tag{5.6}$$

The pump profile is given by $P^{\mathrm{J}}_{l,m}$. The factor of 2 in Eq. 5.5 is a geometric factor: It accounts for the larger size of the B micropillars whose reservoir is about twice as large as for the A and C pillars. Γ_e is the decay rate of the reservoir. As mentioned above, Γ_d is the emission rate into the photon field. The values of those parameters used in the simulations are $\Gamma_e = 0.417\,\mu$eV and $\Gamma_d = 1.52\,\mu$eV, which fall in the typical range of parameters used in micropillar lattices under non-resonant excitation [194, 195]. The pump profile $P^{J}_{l,m}$ is implemented as discretized elongated Gaussian spots applied along the horizontal or vertical lines of the lattice. At each site, the pump intensity is assigned based on its position along the Gaussian envelope. The time evolution of the photon field and the reservoir populations are computed using the ode45 solver, which implements an explicit Runge-Kutta (4,5) method based on the Dormand–Prince pair. This solver uses adaptive step sizing to efficiently and accurately integrate coupled nonlinear differential equations.

5.2.1 Horizontal pumping

We begin by applying a discretized horizontally elongated Gaussian pump profile at specific sites as shown in Fig. 5.2(a). Figure 5.2 provides an illustration of the emergence of lasing in the horizontal line of a Lieb-sp lattice with the excitation conditions of the experiments reported in Fig. 4.5. Fig. 5.2(b) displays the total photon population numerically computed as a function of the applied pump power on log-log scale. For each pump power, the total photon density is evaluated at long enough times for the system to reach the steady state. The characteristic threshold behavior is evident, with a sharp increase in the photon density once the pump exceeds a critical value. This nonlinearity marks the onset of macroscopic occupation, signaling the transition to the lasing regime. To examine the nature of eigenmode selection across threshold, the final steady state photon wavefunction is normalized ($\psi_{\mathrm{final}} = \hat{\psi}/||\hat{\psi}||_2$) and then projected onto the eigenmodes (Φ_n) of the tight-binding Hamiltonian with $s - p_x$ and $s - p_y$ couplings. The corresponding mode weights are given by $|\langle \Phi_n \mid \psi_{\mathrm{final}} \rangle|^2$ that satisfies $\sum_n |\langle \Phi_n \mid \psi_{\mathrm{final}} \rangle|^2 = 1$.

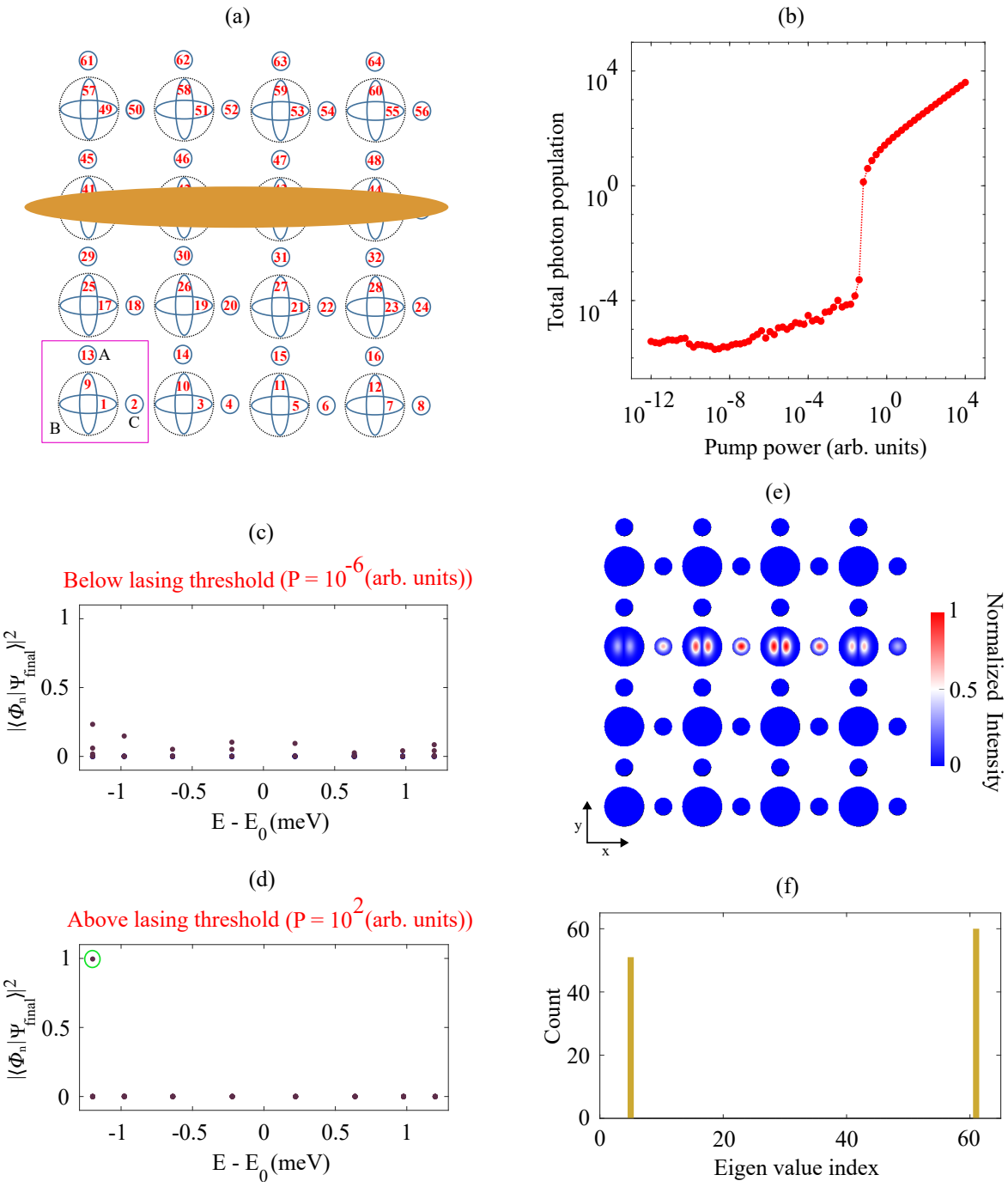

Figure 5.2: (a) Sketch of the configuration for the excitation of an horizontal line of the lattice. (b) Total photon population as a function of pump power, showing the onset of lasing. The final steady-state photon wavefunction projected onto the eigenmodes ($|\langle \Phi_n \mid \psi_{\text{final}} \rangle|^2$) at two pump strengths, one below (c) and one above the lasing threshold (d). (e) The real space intensity profile for the only lasing eigenmode that is circled in green in (d). (f) Histogram of the lasing eigenmodes across 100 different realizations.

The set $|\langle \Phi_n \mid \psi_{\text{final}} \rangle|^2$ is reported for two pump strengths: one below and one above threshold. As shown in Fig. 5.2(c), below threshold ($P = 10^{-6}$ (arb. units)), the photon population is broadly distributed across many modes, while above threshold ($P = 10^{2}$ (arb. units)), a single mode dominates (specifically, the 5th mode index circled in green from the lowest eigenmode energy), with a projection value close to 0.99 in Fig. 5.2(d). Fig. 5.2(e) displays the steady state spatial distribution of the lasing mode in real space, taken at a pump value $P = 10^{2}$ (arb. units) (above the lasing threshold). To quantify the spatial confinement of the lasing mode in real space, the ratio of the total intensity within the horizontally pumped sites to the total intensity across the entire lattice was calculated. This fraction approaches unity, indicating that the lasing mode remains strongly confined to the pumped region. It is important to note that the panels Fig. 5.2(b-e) are plotted for one stochastic realization.

In the model described in Eq. 5.4, lasing is initiated by spontaneous stochastic scattering from the reservoir, which is represented as a random-phase noise term $e^{i\phi_{l,m}^{J,\mu}(t)}$ in the field equation. This noise seeds symmetry breaking among nearly degenerate modes; close to threshold, gain and mode competition exponentially amplify infinitesimal differences, leading to shot-to-shot variability in the selected lasing eigenmode. Numerically, the noise term is evaluated at the adaptive time points chosen by MATLAB's ode45 solver, so the noise enters the field equation as a discrete-time random drive sampled on a non-uniform, solver-chosen grid. To capture this intrinsic variability and obtain reliable statistics, we compute an ensemble of 100 independent realizations with distinct Random Number Generator (RNG) seeds in MATLAB. The resulting histogram of the lasing mode indices, shown in Fig. 5.2(f), reveals that line lasing occurs consistently in two dominant eigenmodes: the 5th mode index (a bonding mode - where all pillars are in phase), appearing in 40 trials, and the 61st mode index (an antibonding mode - π phase difference between adjacent pillars), appearing in 60 trials. Therefore, the stochastic realization selects either the bonding or antibonding mode for lasing; however, this behavior is not observed in the experiments. This discrepancy will be addressed in the next section.

5.2.2 The role of dissipative coupling

In the experiment, lasing occurs consistently in line modes at the top of the *sp* band (antibonding), regardless of whether we use a single elongated pump spot or two crossed spots, as discussed in Chapter 4. This preference for antibonding band edge lasing was also observed in previous microcavity lattice studies [124, 196, 197] due to its longer photon lifetime. The spatial profile of these antibonding modes possess a node in the junctions between adjacent pillars. These junctions have the smallest etching features of the structure and the highest density of defects. In contrast, the wavefunctions of the lower-energy bonding modes exhibit

high intensity at these very junctions, subjecting them to stronger dissipation and making them less favorable for lasing. To model this feature, we have introduced a dissipative coupling term [198] in H_{sp} of Eq. 4.1, by replacing t_{sp} with $t_{sp} + i\gamma_{sp}$. This imaginary hopping term results in complex eigenvalues of H_{sp} whose imaginary part can be associated with extra photon losses and is greater for the upper band eigenvalues than for the lower band ones. Using a value of γ_{sp} as small as $5\,\mu$eV, the simulations systematically produce lasing at the top modes of the *sp* band across 100 independent stochastic realizations. For the configuration of Fig. 5.2(f) with dissipative coupling, the histogram in Fig. 5.3 shows lasing at the eigenvalue index 61 in all 100 trials (antibonding state preferred). This outcome is directly comparable to the experimental observation. It is important to mention that if t_{sp} is replaced with $t_{sp} - i\gamma_{sp}$, the lasing eigenmode in all 100 realizations will be index 5 of the lowest band (bonding state will be preferred). Therefore, it should be noted that all simulations discussed for vertical and cross pumping configuration from now on will have dissipative coupling in the Hamiltonian such that upper band has higher losses.

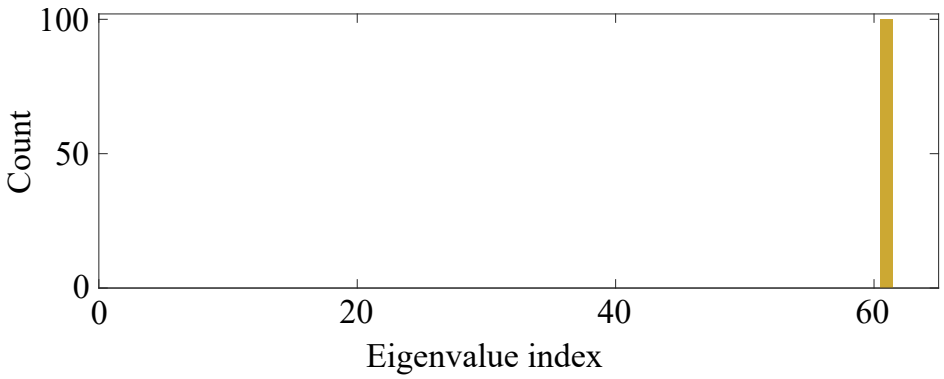

Figure 5.3: Histogram of the lasing eigenmodes across 100 different realizations for the same configuration as Fig. 5.2(f) but by replacing t_{sp} with $t_{sp} + i\gamma_{sp}$ in the Hamiltonian.

5.2.3 Vertical pumping

The same protocol followed for horizontal pumping in the previous section is mimicked using a vertically elongated Gaussian pump profile, now applied to a set of vertically aligned lattice sites as in Fig. 5.4(a). The analysis mirrors that of the horizontal case for the lasing threshold in Fig. 5.4(b), mode projection onto the eigenmodes is shown for both below Fig. 5.4(c) and above lasing threshold Fig. 5.4(d), with lasing mode dominance at 60th eigen value index (circled in green) with a projection value close to 0.99. Fig. 5.4(e) displays the real space intensity distribution for the lasing eigenmode circled in green. The vertical confinement ratio is close to unity, confirming that the line lasing mode remains spatially localized along the vertically pumped sites.

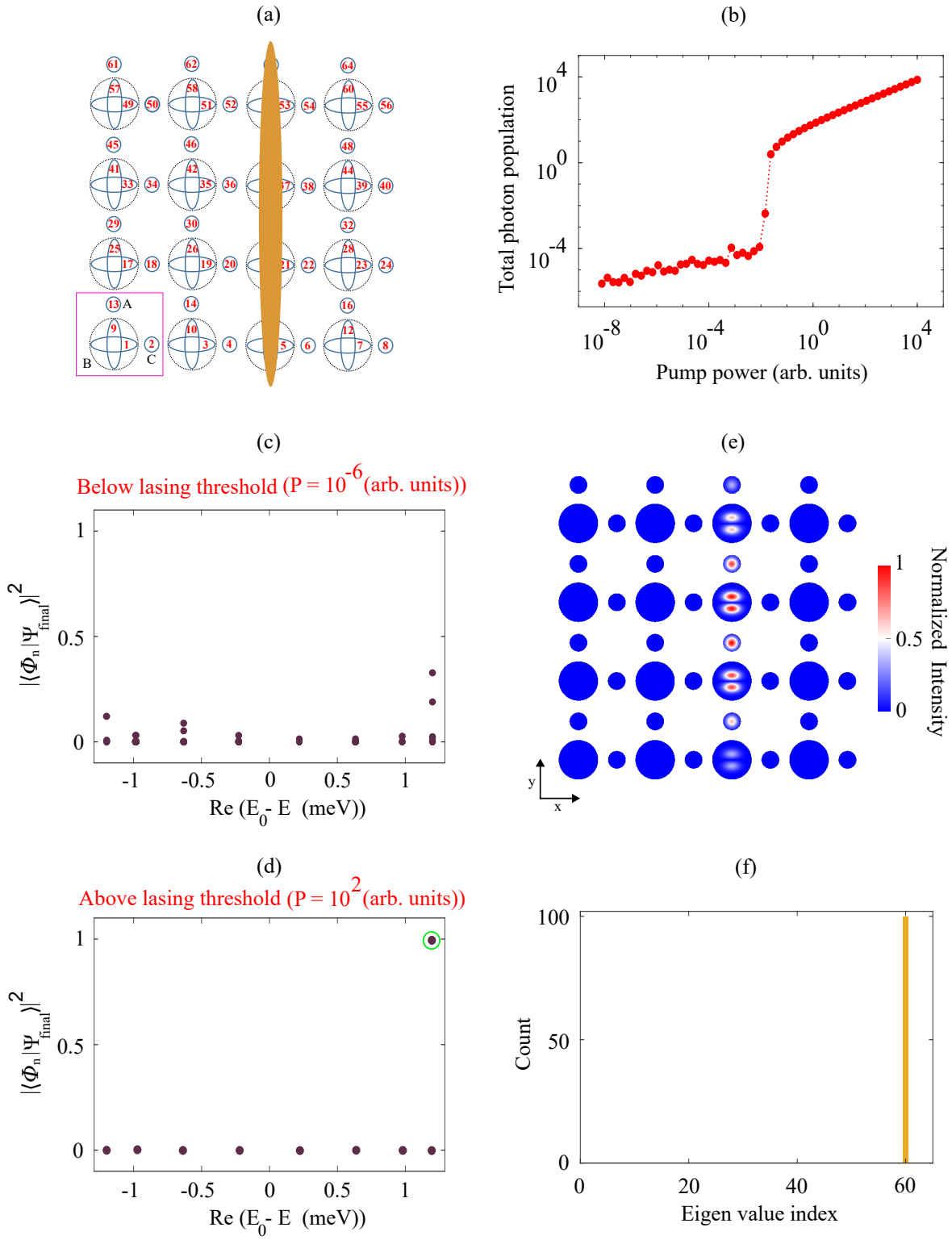

Figure 5.4: (a) Sketch of the configuration for the excitation of an vertical line of the lattice. (b) Total photon population as a function of pump power, showing the onset of lasing. The final steady-state photon wavefunction projected onto the eigenmodes ($|\langle \Phi_n \mid \psi_{\text{final}} \rangle|^2$) at two pump strengths, one below (c) and one above the lasing threshold (d). (e) The real space intensity profile for the only lasing eigenmode that is circled in green in (d). (f) Histogram of the lasing eigenmodes across 100 different realizations with dissipative coupling.

The histogram of lasing mode indices for 100 independent stochastic realizations in Fig. 5.4(f) reveals consistent line lasing in the 60th eigenvalue index (antibonding mode in the upperband) due to dissipative coupling.

5.3 Cross pumping

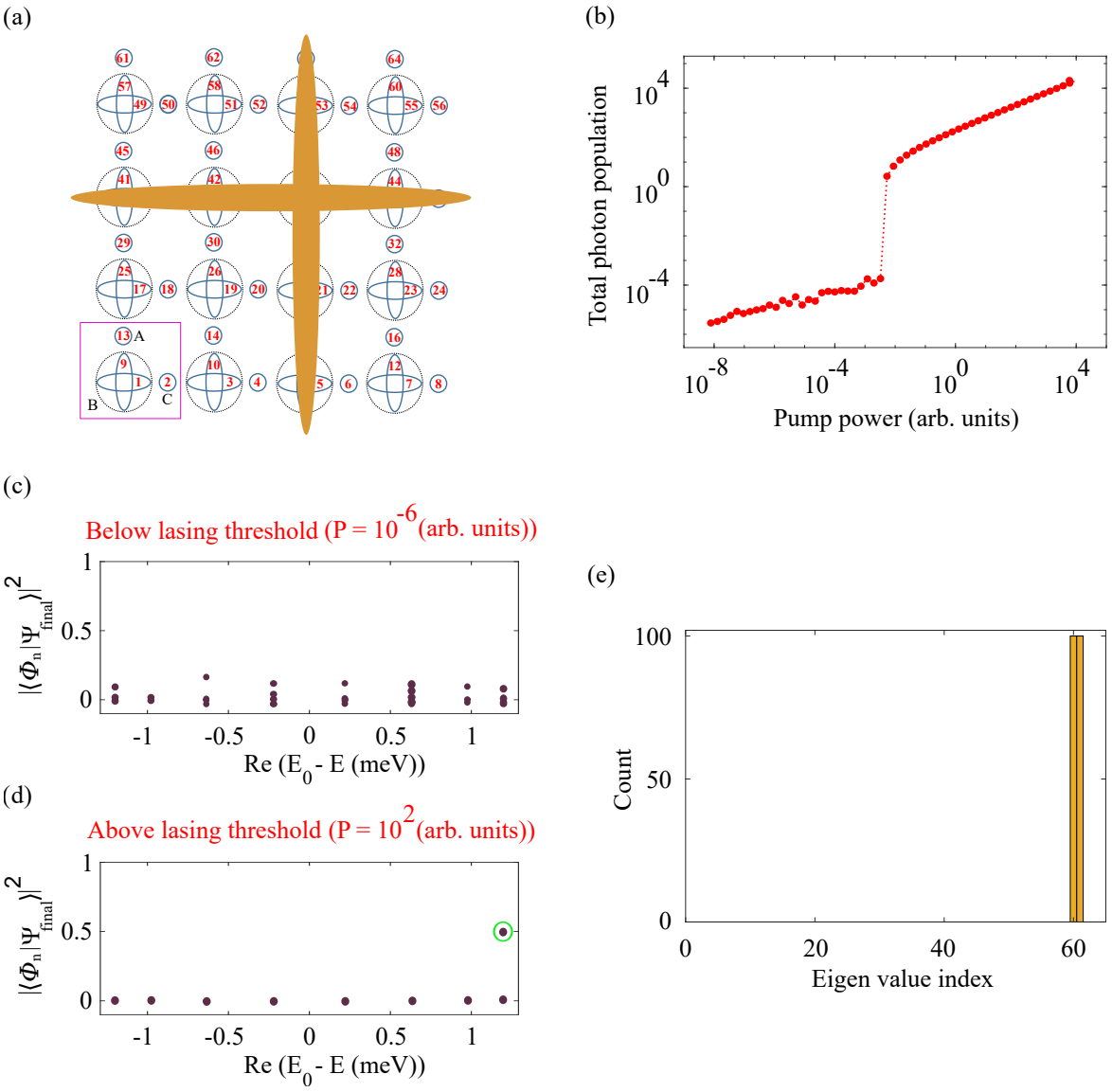

Figure 5.5: (a) Sketch of the configuration for the excitation of crosspump of the lattice. (b) Total photon population as a function of pump power, showing the onset of lasing. The final steady-state photon wavefunction projected onto the eigenmodes ($|\langle \Phi_n \mid \psi_{\text{final}} \rangle|^2$) at two pump strengths, one below (c) and one above the lasing threshold (d). (e) Histogram of the lasing eigenmodes across 100 different realizations showing two eigenvalue index lasing simultaneously.

Since the horizontal and vertical configurations reproduce the experimental behavior, we now delve into the origin of phase locking under cross pumping. In the experiment, the two crossing excitation spots cross at a common site (B pillar) with

perpendicular polarization, so in the modeling the intersection site receives contributions from both pump spots, as sketched in Fig. 5.5(a). Using the same analysis protocol used before, the lasing threshold is shown in Fig. 5.5(b). Mode projection onto the eigenmodes is shown for both below (Fig. 5.5(c)) and above lasing threshold (Fig. 5.5(d)). The two line modes in the antibonding band lase simultaneously at eigenvalue indices 60 and 61, with projection weights of 0.5 each which is encircled with green in Fig. 5.5(d). The real space intensity profile also yields horizontal and vertical fractions of 0.5 as shown in Fig. 5.6(a). The robustness of this result is confirmed across 100 independent stochastic realizations, summarized by the histogram of lasing mode indices in Fig. 5.5(e).

To test whether the common reservoir at the intersection of two pump spots could enforce phase locking, the time evolution of the relative phase is simulated between two selected sites - one on the horizontal arm and one on the vertical arm (rectangle box in Fig. 5.6(a)) after the pump is switched on. Fig. 5.6(b) plots the temporal evolution of the relative phase between the two sites. At short times (up to $\sim$ 100 ps), spontaneous scattering from the reservoir leads to random phase dynamics at both sites, i.e., the absence of long-range phase coherence. As the lasing mode begins to dominate ($\sim$ 100–300 ps), the relative phase exhibits coherent oscillations and eventually stabilizes around $-2\pi/3$ at longer times, as shown in Fig. 5.6(b). Each run proceeds from 0 to 1500 ps, however, the analysis is restricted to the window 700–1500 ps where the relative phase is stable. This result corresponds to one stochastic realization.

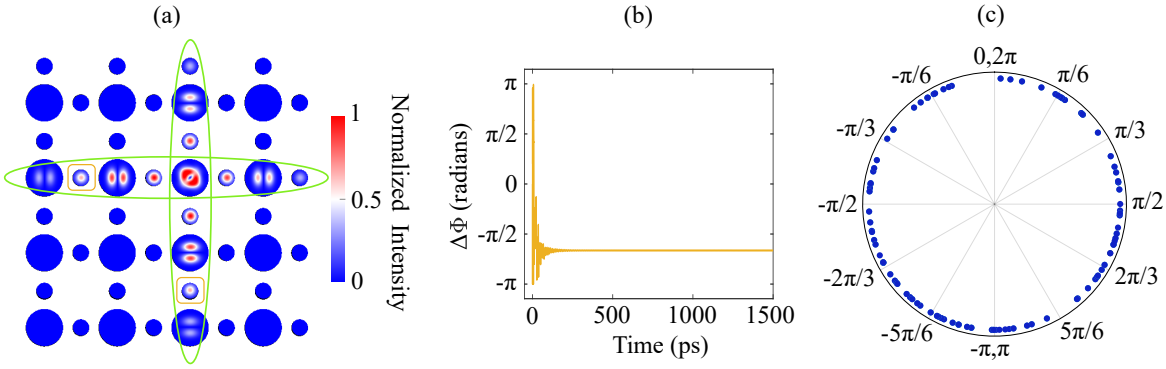

Figure 5.6: (a) Real-space intensity profile of the lasing mode above the lasing threshold, illustrating line lasing within the lattice. (b) Relative phase difference over time between two selected sites, one in the horizontal arm and one in the vertical arm highlighted by rectangles in (a). (c) Wrapped circular mean ($\langle \Delta\phi \rangle_{\text{circ}}$) showing dispersed points for 100 different realizations.

To assess how consistent this steady-state relative phase is across realizations, we do the following for each realization: compute the relative phase ($\Delta\Phi$) between the two boxed sites in Fig. 5.6(a) in the steady state window $\{k : 700 \leq T_k \leq 1500\}$ and map it in the complex plane via $z_k = e^{i\Delta\Phi(T_k)}$. The complex average is $\bar{z} = \frac{1}{N}\sum_k e^{i\Delta\Phi(T_k)}$ and $\langle \Delta\phi \rangle_{\text{circ}} = \arg(\bar{z})$ gives the circular mean angle. In the polar plot across multiple realizations, each dot represents one realization plotted at unit

radius (emphasizing only the mean relative phase) with angle $\langle \Delta\phi \rangle_{\text{circ}}$. Clustering near 0 indicates in-phase locking, while clustering near π indicates anti-phase locking. Across 100 realizations, the points on the unit circle are broadly dispersed in Fig. 5.6(c), indicating no preferred relative phase and thus no phase locking. Therefore, a shared reservoir is not the cause of locking mechanism and an additional term is required to induce phase locking.

5.3.1 $P_x - P_y$ coupling

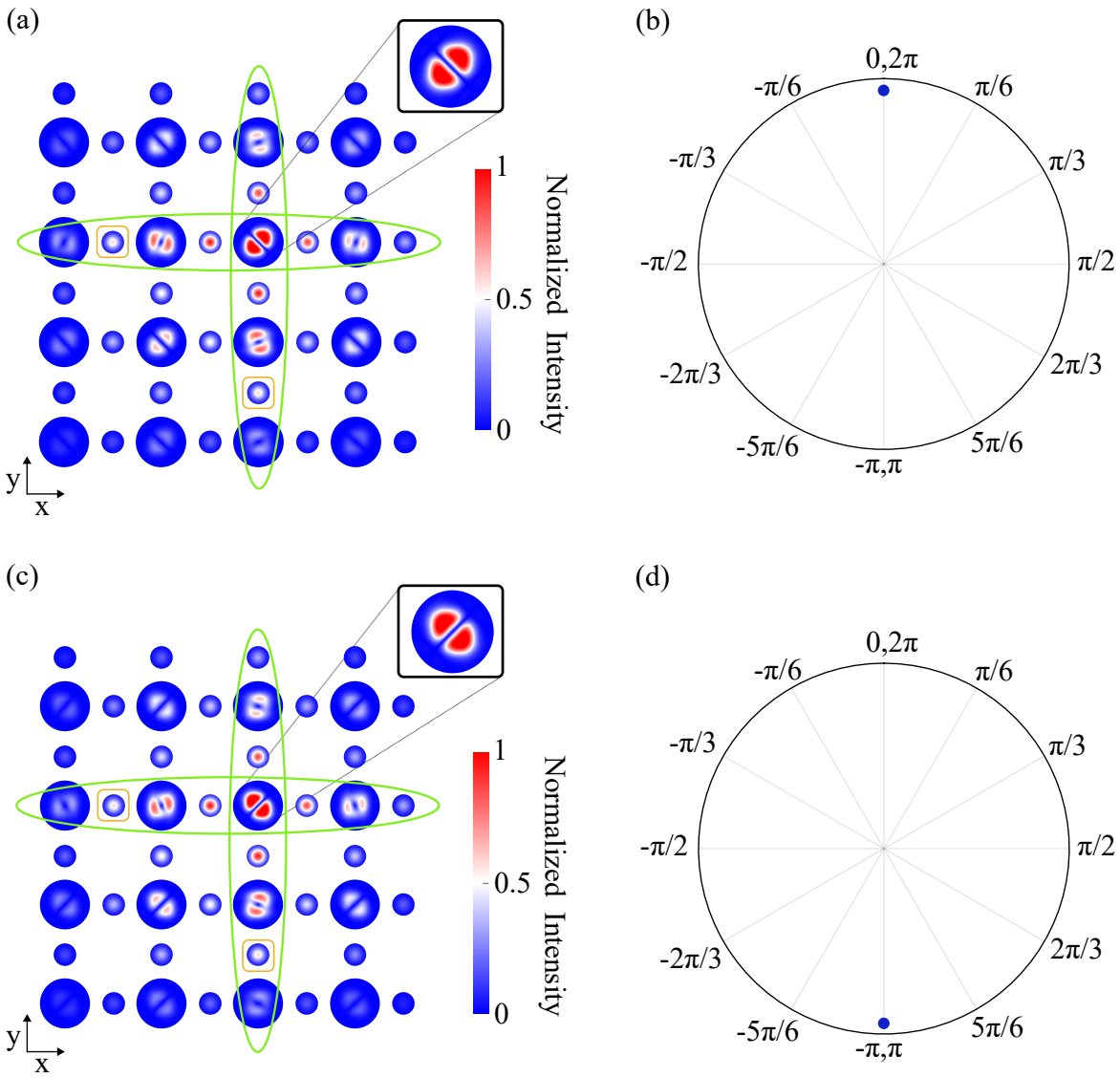

Figure 5.7: (a) Real-space intensity profile of the lasing mode above the lasing threshold, illustrating line lasing within the lattice. The inset shows a zoomed view of the site at which the two lines cross. (b) Wrapped circular mean ($\langle \Delta\phi \rangle_{\text{circ}}$) showing phase locking at $0, 2\pi$ for 100 different realizations. (c,d) Same configuration as (a,b) but with $t_{p_x p_y}$ reversed and the $\langle \Delta\phi \rangle_{\text{circ}}$ showing phase locking at $-\pi, \pi$ for 100 different realizations.

Since dissipative coupling together with the cross-shaped pump profile did not reproduce the observed phase locking between horizontal and vertical lines, the next test was whether the B-site ellipticity could be responsible. This is motivated by the recent work of [199] that even weak ellipticity lifts the p_x/p_y degeneracy and hybridizes these orbitals within a single trap. Therefore, to model this feature in Eq. 5.4, a coupling term is incorporated between the p_x and p_y orbitals of each B site: $H_{p_xp_y} = \sum_{\text{B sites}} -t_{p_xp_y}|\psi_{l,m}^{\text{B},p_x}\rangle\langle\psi_{l,m}^{\text{B},p_y}| + h.c.$ A possible origin of this term in our case might be a residual ellipticity in the shape of the B pillars, most probably introduced during fabrication. This ellipticity breaks the degeneracy between the p_x and p_y orbitals. Through numerical simulations across 100 independent stochastic realizations, we find that for the parameters used in our simulations, a minimum coupling strength $t_{p_xp_y} = 37.5\,\mu$eV (nearly half of Γ_p) is required to induce phase locking of the two line modes with the observed relative phase. Fig. 5.7(a) shows the real space pattern for lasing eigenmode above the lasing threshold with the crossing site corresponding to the linear superposition $|p_x\rangle + |p_y\rangle$ (shown as an inset). This is confirmed by the unit circle plot of circular mean clustered at 0 or 2π for all realizations, as shown in Fig. 5.7(b). Reversing the sign of $t_{p_xp_y}$ flips the locked phase by π, resulting in $|p_x\rangle - |p_y\rangle$ (shown as an inset) in Fig. 5.7(c). The circular-mean angles for all realizations are concentrated at π or $-\pi$ as shown in Fig. 5.7(d). Although $p_x - p_y$ mixing is sufficient to produce phase locking, the two targeted line modes carry only ($\sim$ 66%) of the total emission, indicating leakage into other lines that is absent in the experiment. This discrepancy motivates the inclusion of an additional term, discussed in the following section.

5.3.2 Reservoir-induced nonlinear blueshift

From the previous section, we find that introducing $p_x - p_y$ coupling is sufficient to obtain phase locking; however, only $\sim$ 66% of the emitted intensity originates from the pumped lines, while the experiment (Fig. 4.7(d)) exhibits maximum confinement to the two pumped lines. Few recent studies have shown that under non-resonant pumping, the excitonic reservoir can generate a local blueshift potential that traps and guides polariton condensates [108, 200]. Guided by this, we hypothesize that the pumped sites might be effectively detuned from the rest of the lattice in the experiment. To capture this effect in the simulation, we include a reservoir-induced blueshift that raises the on-site photon energy at pumped sites by adding a real on-site term $g_R n_{l,m}^J$ to the Hamiltonian, so that the time evolution of the scalar photon field $\{|\psi_{l,m}^{J,\mu}\rangle\}$ at unit cell (l,m), site $J \in \{A,B,C\}$, and orbital $\mu \in \{s,p_x,p_y\}$ includes dissipative coupling, $p_x - p_y$ overlap, and the reservoir-induced blueshift which is given by;

$$i\hbar\frac{d}{dt}|\psi^{J,\mu}_{l,m}\rangle = \left(H_{sp} + H_{p_x p_y} - i\frac{\Gamma_p}{2} + g_R n^J_{l,m} + i\frac{\Gamma_d}{2}n^J_{l,m}\right)|\psi^{J,\mu}_{l,m}\rangle + \frac{\sqrt{n^J_{l,m}}}{2}\Gamma_d e^{i\phi^{J,\mu}_{l,m}(t)} \tag{5.7}$$

where g_R is the strength of the nonlinear interaction between the photon field and the reservoir.

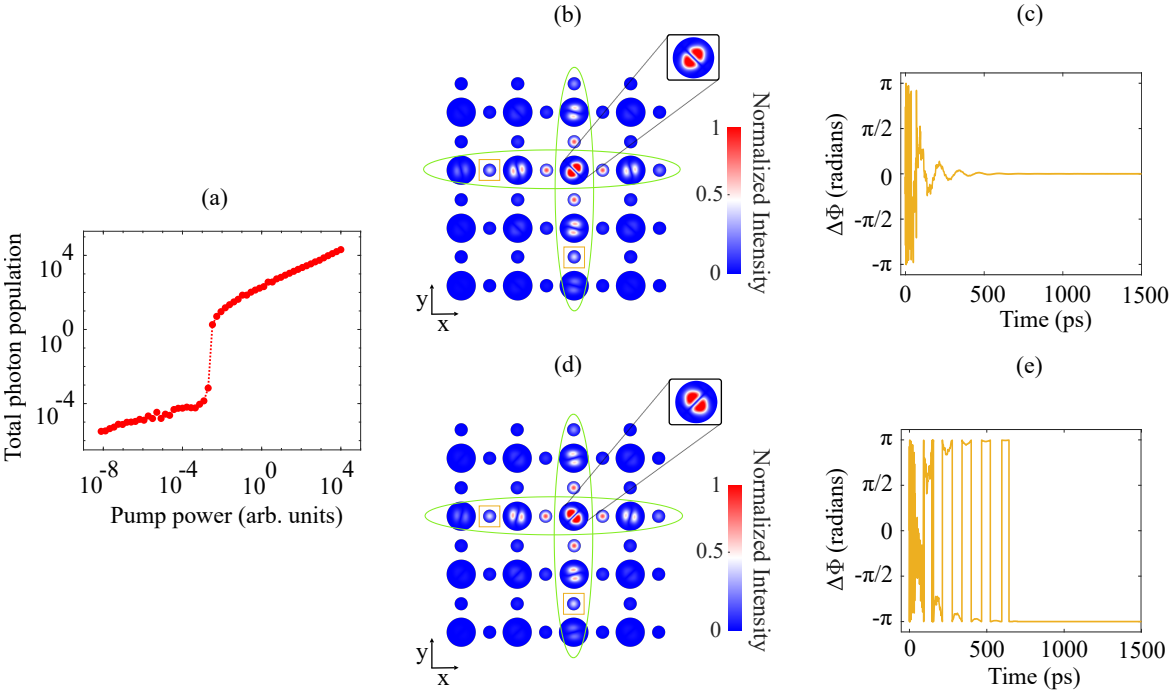

Figure 5.8: (a) Total photon population as a function of pump power, showing the onset of lasing. (b) Real-space intensity profile of the lasing mode above the lasing threshold, illustrating line lasing within the lattice. The inset shows a zoomed view of the site at which the two lines cross. (c) Relative phase difference over time, phase locking at 0 between two selected sites, one in the horizontal arm and one in the vertical arm highlighted by rectangles in (b). (d, e) For the same configuration as (b) and (c) but with $t_{p_x p_y}$ reversed where the phase locking is at $-\pi$.

By introducing an on-site reservoir blueshift in the simulation, with a value of $g_R = 2\,\mu$eV, the lasing confinement to the two pumped lines becomes maximum. Figure 5.8(a) shows the total photon population computed as a function of pump power on a log-log scale. In Fig. 5.8(b), the real-space pattern for the lasing eigenmode at above lasing threshold, the crossing site corresponds to the linear superposition $|p_x\rangle + |p_y\rangle$ (shown as an inset). With the addition of the nonlinear term g_R, the two targeted line modes carry ($\sim 96\%$) of the total emission. The temporal evolution of the relative phase for the two boxed sites in Fig. 5.8(b) indicates that it locks to 0 or 2π at longer times, as shown in Fig. 5.8(c). When the sign of $t_{p_x p_y}$ is reversed, the pattern of the crossing-site at above lasing threshold exhibits antisymmetric superposition ($|p_x\rangle - |p_y\rangle$) (Fig. 5.8(d), inset), and the relative phase

locks to $-\pi$ or π as shown in Fig. 5.8(e). Thus, Eq. 5.7 that combines dissipative coupling, p_x–p_y overlap and reservoir-induced blueshift constitutes the minimal Hamiltonian that reproduces phase locking with maximum line-confined lasing from the pumped lines.

5.4 Summary

This chapter addressed the origin of phase locking between two line lasers. A driven-dissipative model with mode-selective dissipation and the cross-shaped pump alone does not lock: the wrapped circular means over 100 realizations are broadly distributed, showing that a shared reservoir is insufficient. Phase locking emerges when an $p_x - p_y$ overlap is added within the pillars where orthogonal modes exist. For our parameters, a threshold of $t_{p_x p_y} \approx 37.5\ \mu\text{eV}\ (\Gamma_p/2)$ yields the observed relative phase, and reversing $\text{sign}(t_{p_x p_y})$ flips the locked phase by π, consistent with $|p_x\rangle \pm |p_y\rangle$ at the crossing. With this overlap term introduced in the effective Hamiltonian, about 66% of the emission resides in the two target lines. However, adding a reservoir-induced blueshift suppresses this residual leakage and concentrates the lasing emission on those lines, producing robust locking across realizations. Thus, the minimal Hamiltonian that explains cross pumping induced phase locking seen in the experiment comprises mode selective dissipation, orthogonal modes in the same-pillar $p_x - p_y$ overlap, and reservoir nonlinearity.

6

CONCLUSION & PERSPECTIVES

6.1 Conclusion

In this thesis, we have investigated semiconductor microstructures based on a Fabry–Perot cavity with an embedded quantum well, laterally patterned to explore non-Hermitian physics. The fabrication processes developed in the cleanroom facilities of C2N enabled the realization of $1D$ and $2D$ lattices of coupled semiconductor micropillars. Precise control over the cavity wedge, pillar diameter, and inter-pillar overlap allowed us to implement and study tight-binding lattice Hamiltonians in a well-controlled setting. The driven–dissipative nature of the system made it possible to directly access both real-space mode profiles and the lattice band structure at cryogenic temperatures via photoluminescence measurements. This thesis was organized around two main lines of investigation: (i) how interference between coherent external drives and lattice eigenmodes can be harnessed to control transport and localization, and (ii) how band-structure engineering can be used to obtain lasing in unconventional exotic modes.

In the first part of the thesis, interference was used as a powerful control parameter to tailor transport and localization. By tuning the relative phase of coherent drives, we demonstrated directional transport across the entire band and established how light inside the lattice can be switched ON and OFF purely by phase control. Importantly, we showed that nonlinearity reshapes these interference conditions: increasing pump power allows localization to reappear at detunings where the linear system is only weakly localized, giving access to states that are inaccessible in the linear regime. From an experimental perspective, we identified the sensitivity of such interference phenomena, in particular how stray light can strongly suppress localization, setting clear constraints for future implementations. A key conceptual difference from Gross–Pitaevskii modeling in [52] is that we go beyond a single-field description and use a two-coupled exciton–photon model to understand the experimental observations. Within this framework, the pump power for maximum localization shows a superlinear increase with detuning, in clear contrast to the linear trend obtained from the Gross–Pitaevskii approach.

In the second part of the thesis, we introduce a band-engineered lasing architecture based on orbital coupling in a Lieb sp lattice, to produce bands that are

flat along one direction and dispersive along the orthogonal one. This enabled line lasing in a $2D$ matrix and phase locking between orthogonal line modes when pumped in the form of a cross. Having uncovered the underlying mechanism in terms of orbital coupling and reservoir-induced nonlinearities, the ideas can now be used deliberately to design cross-coupled lasing modes and locking schemes in more complex geometries.

6.2 Perspectives

From the perspective of interference-controlled transport and localization, the observed effects highlight the central role of interference in the presence of nonlinearities and motivate further exploration of lattices with topological properties, where nontrivial edge and gap states may provide robustness against imperfections while still supporting rich nonlinear behavior [201], as well as lattices with alternative band structures, where tailored dispersions can open new regimes of controllable localization [50, 51]. Beyond the semi-classical regime addressed here, an exciting future direction is to extend this interference-based control into the quantum regime using platforms that combine scalable photonic lattices with chemically engineered single photon emitters and open-cavity readout. Such systems could enable the observation of collective quantum optical phenomena, including subradiant bound states in the continuum [19] and tunable range light-localization in the presence of photonic band-gaps.

From the perspective of band-engineered lasing modes, the two features (independent lasing of parallel lines and phase locking of crossing lines) anticipate great flexibility in the design of densely integrated lasers with special real-space patterns, particularly when considering electrical injection with line or site resolution. First observations of lasing under electrical injection in lattices of coupled micropillars [202, 203] anticipate exciting prospects in this direction. However, we have shown that blueshifts (a characteristic of the loss of strong coupling in polariton lattices) play an important role in the confinement of the lasing modes into individual lines. It remains an open question if similar lasing line modes would be present in lattices of VCSELs at room temperature, which operate in the weak coupling regime and show much weaker energy shifts.

We expect that the results and insights presented in this manuscript, together with the perspectives outlined above, will help in the further exploration and innovation of new physics in non-Hermitian lattices.

A

SAMPLE DETAILS

A.1 1D chain lattice

The nominal growth parameters of the semiconductor microcavity used for the one-dimensional lattice experiments on optical switching, directional transport, and localization are summarized in Table A.1.

Design 1	Material	δz [nm]	$n(\lambda = 858\,\text{nm})$	Rep
DBR_1	$Ga_{0.90}Al_{0.10}As$	62.0	3.43	32
DBR_2	$Ga_{0.05}Al_{0.95}As$	72.6	2.93	32
Sp	GaAs	113.6	3.51	1
QW	$In_{0.05}Ga_{0.95}As$	15	3.51	1
Sp	GaAs	113.6	3.51	1
DBR_2	$Ga_{0.05}Al_{0.95}As$	72.6	2.93	36
DBR_1	$Ga_{0.90}Al_{0.10}As$	62.0	3.43	36
Sub	GaAs	3.5×10^5	3.51	1
ARC	$SiO_{0.18}N_{1.22}$	~ 113.5	1.88	1

Table A.1: Nominal parameters used for the growth of the semiconductor microcavity. The target central cavity wavelength is $\lambda_c = 858\,\text{nm}$. δz is the layer thickness, n is the refractive index at λ_c, and Rep is the number of repetitions of each layer. ARC denotes the anti-reflective coating.

A.2 Lieb sp lattice

The nominal growth parameters of the semiconductor microcavity used for the Lieb *sp* lattice experiments for line lasing are summarized in Table A.2.

Design 1	Material	δz [nm]	$n(\lambda = 849\,\text{nm})$	Rep
DBR_1	$Ga_{0.90}Al_{0.10}As$	61.5	3.46	31
DBR_2	$Ga_{0.05}Al_{0.95}As$	71.8	2.96	31
Sp	GaAs	111.6	3.54	1
QW	$In_{0.05}Ga_{0.95}As$	17	3.51	1
Sp	GaAs	111.6	3.54	1
DBR_2	$Ga_{0.05}Al_{0.95}As$	71.8	2.96	27
DBR_1	$Ga_{0.90}Al_{0.10}As$	61.5	3.46	27
Sub	GaAs	3.5×10^5	3.54	1
ARC	$SiO_{0.18}N_{1.22}$	~ 115	1.88	1

Table A.2: Nominal parameters used for the growth of the semiconductor microcavity. The target central cavity wavelength is $\lambda_c = 849\,\text{nm}$. δz is the layer thickness, n is the refractive index at λ_c, and Rep is the number of repetitions of each layer. ARC denotes the anti-reflective coating.

B

ANALYTICAL DERIVATION FOR INTENSITY OF SITES IN A 1D LATTICE

B.1 General expression - Two pump spots

This section aims to provide an analytical description of the spatial light distribution within photonic lattices in the linear regime. To simplify the calculation without losing important features, we assume the polariton to be 100% photonic (and thus having no interaction) and neglect the contribution originating from the next-nearest neighbor coupling ($t' = 0$). Under these assumptions, we can write a driven-dissipative tight-binding model, in the rotating frame of the pump laser, describing the dynamics of the photon field ψ_m on each site m:

$$i\hbar\dot{\psi}_m = (\epsilon_0 - \omega_p)\psi_m - i\gamma\psi_m - t(\psi_{m+1} + \psi_{m-1}) + F_m, \tag{B.1}$$

where ϵ_0 is the middle band photonic energy, γ is the radiative decay, t is the nearest neighbor coupling and F_m is the field source term.

It is convenient to write the problem in the reciprocal space using $\psi_m = \frac{1}{\sqrt{M}}\sum_k \psi_k e^{ikm}$ and $F_m = \frac{1}{\sqrt{M}}\sum_k F_k e^{ikm}$ to get:

$$i\hbar\dot{\psi}_k = \left(\epsilon_0 - \omega_p\right)\psi_k - i\gamma\psi_k - 2t\cos k\,\psi_k + F_k, \tag{B.2}$$

with $k \in [-\pi, \pi]$ and M the total number of sites. Introducing $\Delta = \omega_p - \epsilon_0$ and looking for a steady state solution, we obtain

$$\psi_k = \frac{F_k}{\Delta + 2t\cos k + i\gamma}. \tag{B.3}$$

We focus on the situation of interest in the main section of the paper, where only two sites m_1 and m_2 are pumped with a phase difference of $\Delta\phi$. Such pumping can be explicitly written in position space like:

$$F_m = \frac{F}{\sqrt{M}}(\delta_{m,m_1} + e^{i\Delta\phi}\delta_{m,m_2}), \tag{B.4}$$

with $\delta_{m,n}$ the Kronecker delta, or in Fourier space as:

$$F_k = \sum_m F_m e^{-ikm} = \frac{F}{\sqrt{M}} \left(e^{-ikm_1} + e^{i\Delta\phi} e^{-ikm_2} \right). \tag{B.5}$$

We can write the momentum space components of the steady-state solution:

$$\psi_k = \frac{F}{\sqrt{M}} \frac{e^{-km_1} + e^{i\Delta\phi} e^{-ikm_2}}{\Delta + 2t\cos k + i\gamma}. \tag{B.6}$$

We transform back to real space and approximate the discrete sum in momenta by an integral to obtain

$$\psi_m = \frac{1}{\sqrt{M}} \sum_k \psi_k e^{ikm} \approx \frac{F}{2\pi} \int_{-\infty}^{\infty} \frac{e^{ik(m-m_1)} + e^{i\Delta\phi} e^{ik(m-m_2)}}{\Delta + 2t\cos k + i\gamma} dk, \tag{B.7}$$

where the integration limits have been extended from $-\infty$ to ∞ because the integrand vanishes outside the first Brillouin zone. This integral can be calculated using complex analysis and the residue theorem. Depending on the sign of $m - m_1$ and $m - m_2$, the exponential terms $e^{ik(m-m_j)}$ determine whether the integration contour should be closed in the upper or lower half of the complex k-plane. The three scenarios for this are:

1. The considered site is to the left of the two pumped sites: $m < m_1 < m_2 \Rightarrow m - m_1 < 0$ and $m - m_2 < 0$
2. The considered site is in between the two pumped sites: $m_1 < m < m_2 \Rightarrow m - m_1 > 0$ and $m - m_2 < 0$
3. The considered site is to the right of the two pumped sites: $m_1 < m_2 < m \Rightarrow m - m_1 > 0$ and $m - m_2 > 0$

Following the derivation as shown in Appendix B of Ref. [140], we will investigate the above three scenarios and perform the calculation explicitly in one of them to show that we obtain the expression presented in Eq. 2.8 of Chapter 2. The calculations in the other two scenarios are similar and do not present additional complexities compared to the one presented.

B.1.0.1 *Case 1: $m - m_1 < 0$ and $m - m_2 < 0$*

In this case, Eq. (B.7) can be written in the following way, with explicit negative signs in the complex exponent in the integrands:

$$\psi_m \approx \frac{F}{2\pi} \int_{-\infty}^{\infty} \frac{e^{-ik|m-m_1|} + e^{i\Delta\phi} e^{-ik|m-m_2|}}{\Delta + 2t\cos k + i\gamma} dk. \tag{B.8}$$

To evaluate the above integral using the residue theorem, we identify the poles of the integrand in the complex k-plane. These occur where the denominator vanishes

and therefore the dominant contribution arises from the poles closest to the real axis:

$$\Delta + 2t\cos k \approx 0. \tag{B.9}$$

Here, we define the resonant momentum k_0 through:

$$\cos k_0 = -\frac{\Delta}{2t} \quad \Rightarrow \quad k_0 = \arccos\left(-\frac{\Delta}{2t}\right). \tag{B.10}$$

Then, we expand $\cos k$ around $k = k_0$ up to first-order in k to get

$$\cos k \approx \cos k_0 - \sin k_0 (k - k_0). \tag{B.11}$$

Performing some algebra by multiplying both sides by $2t$, substituting $\cos k_0$ by $-\frac{\Delta}{2t}$ and re-arranging the expression, we obtain:

$$\Delta + 2t\cos k \approx -2t\sin k_0 (k - k_0). \tag{B.12}$$

Identifying $\sin k_0$ as:

$$\sin k_0 = \sqrt{1 - \cos^2 k_0} = \sqrt{1 - \left(\frac{\Delta}{2t}\right)^2} = \frac{\sqrt{4t^2 - \Delta^2}}{2t}, \tag{B.13}$$

and plugging in the previous expression, we finally get:

$$\Delta + 2t\cos k \approx -\sqrt{4t^2 - \Delta^2}(k - k_0) \tag{B.14}$$

Doing the same calculation for $k \approx -k_0$, we get:

$$\Delta + 2t\cos k \approx +\sqrt{4t^2 - \Delta^2}(k + k_0), \tag{B.15}$$

Finally, we have

$$\Delta + 2t\cos k \approx \begin{cases} -\sqrt{4t^2 - \Delta^2}\left[k - \arccos\left(\dfrac{-\Delta}{2t}\right)\right] & \text{for } k \text{ close to } k_0 \\ +\sqrt{4t^2 - \Delta^2}\left[k + \arccos\left(\dfrac{-\Delta}{2t}\right)\right] & \text{for } k \text{ close to } -k_0 \end{cases} \tag{B.16}$$

where $k_0 \equiv \arccos\left(\dfrac{-\Delta}{2t}\right)$. These expressions allow us to transform Eq. B.7 into the following integral in which the integrand is only important around the two poles at k_0 and $-k_0$:

$$\psi_m \approx \frac{F}{2\pi}\int_{-\infty}^{\infty}\left[\frac{e^{-ik|m-m_1|} + e^{i\Delta\phi}e^{-ik|m-m_2|}}{-\sqrt{4t^2 - \Delta^2}(k - k_0) + i\gamma} + \frac{e^{-ik|m-m_1|} + e^{i\Delta\phi}e^{-ik|m-m_2|}}{+\sqrt{4t^2 - \Delta^2}(k + k_0) + i\gamma}\right] dk \tag{B.17}$$

At this stage, it is informative to compute the density of state (DOS) to understand how it appears in the final expression. Indeed, the density of states (DOS) is defined by:

$$D(E) = \left|\frac{dk}{dE}\right| = \left|\frac{1}{\frac{dE}{dk}}\right|. \tag{B.18}$$

Starting from the dispersion relation given by:

$$E(k) = -2t\cos k \Rightarrow \frac{dE}{dk} = 2t\sin k \Rightarrow D(E) = \left|\frac{1}{2t\sin k}\right| \tag{B.19}$$

and substituting $\cos k_0 = -\frac{\Delta}{2t}$, we get:

$$\sin k_0 = \sqrt{1-\cos^2 k_0} = \frac{\sqrt{4t^2-\Delta^2}}{2t} \tag{B.20}$$

which brings $D(\Delta) = \frac{1}{\sqrt{4t^2-\Delta^2}}$. Substituting $D(\Delta)$ in Eq. (B.7), we obtain

$$\psi_m \approx -\frac{FD(\Delta)}{2\pi}\int_{-\infty}^{+\infty}\left\{\begin{array}{l}\underbrace{\frac{e^{-ik|m-m_1|}}{k-k_0-i\gamma D(\Delta)}}_{(1)} + \underbrace{e^{i\Delta\phi}\frac{e^{-ik|m-m_2|}}{k-k_0-i\gamma D(\Delta)}}_{(2)} \\ -\underbrace{\frac{e^{-ik|m-m_1|}}{k+k_0+i\gamma D(\Delta)}}_{(3)} - \underbrace{e^{i\Delta\phi}\frac{e^{-ik|m-m_2|}}{k+k_0+i\gamma D(\Delta)}}_{(4)}\end{array}\right\} dk \tag{B.21}$$

We can now evaluate individual integrals using the residue theorem to obtain an expression for $|\psi_m|^2$.

The integrand term (1) has a pole at $k = k_0 + i\gamma D(\Delta)$, which lies in the upper-half complex plane. Since $|m-m_1| > 0$, the exponential $e^{-ik|m-m_1|}$ decays as $\mathrm{Im}(k) \to -\infty$, i.e., in the lower-half plane. To ensure convergence, the contour is closed in the lower-half, which does not enclose the pole. Therefore, the integral is zero.

$$\int_{-\infty}^{+\infty} dk \frac{e^{-ik|m-m_1|}}{k-k_0-i\gamma D(\Delta)} = 0 \tag{B.22}$$

Similar to the first term, the integrand term (2) has a pole at $k = k_0 + i\gamma D(\Delta)$ that lies in the upper-half plane. The exponential $e^{-ik|m-m_2|}$ decays in the lower-half, so the contour is again closed downward and the pole is not enclosed. Thus, the integral evaluates to zero.

$$\int_{-\infty}^{+\infty} dk \frac{e^{-ik|m-m_2|}}{k-k_0-i\gamma D(\Delta)} = 0 \tag{B.23}$$

The integrand term (3) has a pole at $k = -k_0 - i\gamma D(\Delta)$, which lies in the lower-half plane. Since $|m - m_1| > 0$, the exponential $e^{-ik|m-m_1|}$ also decays in the lower-half. Therefore, we close the contour in the lower-half, and the pole is enclosed. The residue contributes, yielding a non-zero result ($e^{-i(-k_0-i\gamma D(\Delta))|m-m_1|} = e^{+ik_0|m-m_1|}e^{-\gamma D(\Delta)|m-m_1|}$), which brings

$$\int_{-\infty}^{+\infty} dk \frac{e^{-ik|m-m_1|}}{k + k_0 + i\gamma D(\Delta)} = -2\pi i\, e^{+ik_0|m-m_1|}\, e^{-\gamma D(\Delta)|m-m_1|} \tag{B.24}$$

The integrand term (4) follows the same logic as the third: it has a pole at $k = -k_0 - i\gamma D(\Delta)$ which lies in the lower-half plane, and the exponential decays there as well. Thus, closing the contour downward encloses the pole, and the residue contributes a non-zero value.

$$\int_{-\infty}^{+\infty} dk \frac{e^{-ik|m-m_2|}}{k + k_0 + i\gamma D(\Delta)} = -2\pi i\, e^{+ik_0|m-m_2|}\, e^{-\gamma D(\Delta)|m-m_2|} \tag{B.25}$$

Thus, assembling all these results together, we obtain the following expression for the field at sites located at the left of the pumping spots:

$$\psi_m = -FD(\Delta)i\left[e^{ik_0|m-m_1|}e^{-\gamma D(\Delta)|m-m_1|} + e^{i\Delta\phi}e^{ik_0|m-m_2|}e^{-\gamma D(\Delta)|m-m_2|}\right] \tag{B.26}$$

Taking the square modulus brings:

$$I_m = |\psi_m|^2 = |F|^2 D(\Delta)^2 \left|e^{ik_0|m-m_1|}e^{-\gamma D(\Delta)|m-m_1|} + e^{i\Delta\phi}e^{ik_0|m-m_2|}e^{-\gamma D(\Delta)|m-m_2|}\right|^2 \tag{B.27}$$

We recover the equation present in Eq. 2.8 of Chapter 2. In the following, we show the different cases for completeness, but we do not reproduce all the details of the calculations. We mainly explain how we recover the same expression for I_m.

B.1.0.2 *Case 2: $m - m_1 > 0$ and $m - m_2 < 0$*

Using the same derivation as in case 1, and taking care of the right sign of the complex exponents in case (2), we obtain an equation similar to Eq. (3):

$$\psi_m \approx -\frac{FD(\Delta)}{2\pi}\int_{-\infty}^{+\infty}\left\{\begin{array}{l}\underbrace{\dfrac{e^{ik|m-m_1|}}{k - k_0 - i\gamma D(\Delta)}}_{(1)} + \underbrace{\dfrac{e^{i\Delta\phi}e^{-ik|m-m_2|}}{k - k_0 - i\gamma D(\Delta)}}_{(2)} \\ -\underbrace{\dfrac{e^{ik|m-m_1|}}{k + k_0 + i\gamma D(\Delta)}}_{(3)} - \underbrace{\dfrac{e^{i\Delta\phi}e^{-ik|m-m_2|}}{k + k_0 + i\gamma D(\Delta)}}_{(4)}\end{array}\right\} dk \tag{B.28}$$

This case is symmetric to case 1, but the roles of m_1 and m_2 are reversed in terms of which exponential contributes. Terms (1) and (4) now contribute to the integral, while (2) and (3) vanish. The derivation proceeds in exactly the same manner, and the resulting expression for I_m is unchanged.

B.1.0.3 *Case 3: $m - m_1 > 0$ and $m - m_2 > 0$*

Similarly, we get the following expression:

$$\psi_m \approx -\frac{FD(\Delta)}{2\pi}\int_{-\infty}^{+\infty}\left\{\begin{array}{l}\underbrace{\dfrac{e^{ik|m-m_1|}}{k-k_0-i\gamma D(\Delta)}}_{(1)}+\underbrace{\dfrac{e^{i\Delta\phi}e^{ik|m-m_2|}}{k-k_0-i\gamma D(\Delta)}}_{(2)}\\ -\underbrace{\dfrac{e^{ik|m-m_1|}}{k+k_0+i\gamma D(\Delta)}}_{(3)}-\underbrace{\dfrac{e^{i\Delta\phi}e^{ik|m-m_2|}}{k+k_0+i\gamma D(\Delta)}}_{(4)}\end{array}\right\}dk \tag{B.29}$$

In this case, both exponential terms $e^{ik|m-m_1|}$ and $e^{ik|m-m_2|}$ decay in the upper-half complex plane. As a result, the contour is closed in the upper-half, enclosing the poles at $k = k_0 + i\gamma D(\Delta)$. The poles of the first two terms lie in the upper-half plane and are enclosed. Therefore, only the contributions from terms (1) and (2) yield non-zero residues. After applying the residue theorem, we again obtain the same structure for ψ_m, and consequently the same final expression for the intensity $I_m = |\psi_m|^2$.

Therefore, in all three cases, we get the following result;

$$I_m = |\psi_m|^2 = |F|^2 D(\Delta)^2 \left| e^{ik_0|m-m_1|}e^{-\gamma D(\Delta)|m-m_1|} + e^{i\Delta\phi}e^{ik_0|m-m_2|}e^{-\gamma D(\Delta)|m-m_2|}\right|^2 \tag{B.30}$$

B.2 Derivation of the criteria for directionality

To derive the conditions under which directional emission occurs, we analyze the steady-state intensity in the region to the left of both pump sites, i.e., for $m < m_1$ and $m < m_2$, that is, case 1. The link with the general expression is made by having in mind that $(m - m_1) = -|m - m_1|$ and $(m - m_2) = -|m - m_2|$. Identifying the conditions for complete destructive interference, we can determine the values of $\Delta\phi$ and k_0 that suppress propagation in this direction and thus lead to directional transport. Specifically, the intensity at the site m takes the form:

$$I_m = |F|^2 D(\Delta)^2 \underbrace{\left| e^{-ik_0(m-m_1)} e^{\gamma D(\Delta)(m-m_1)} + e^{i\Delta\phi} e^{-ik_0(m-m_2)} e^{\gamma D(\Delta)(m-m_2)} \right|^2}_{= 0 \text{ (complete destructive interference)}} \tag{B.31}$$

$$I_m = |F|^2 D(\Delta)^2 |A+B|^2 = |F|^2 D(\Delta)^2 (|A|^2 + |B|^2 + A^*B + AB^*) \tag{B.32}$$

$$\begin{aligned} A &= e^{-ik_0(m-m_1)} e^{\gamma D(\Delta)(m-m_1)} \\ B &= e^{i\Delta\phi} e^{-ik_0(m-m_2)} e^{\gamma D(\Delta)(m-m_2)} \end{aligned}$$

$$\begin{aligned} |A|^2 &= e^{2\gamma D(\Delta)(m-m_1)} \\ |B|^2 &= e^{2\gamma D(\Delta)(m-m_2)} \\ A^*B &= e^{i\Delta\phi} e^{ik_0(m_2-m_1)} e^{\gamma D(\Delta)(2m-m_1-m_2)} \\ AB^* &= e^{-i\Delta\phi} e^{-ik_0(m_2-m_1)} e^{\gamma D(\Delta)(2m-m_1-m_2)} \end{aligned}$$

Therefore,

$$\begin{aligned} \frac{I_m}{|F|^2 D(\Delta)^2} = {} & e^{2\gamma D(\Delta)(m-m_1)} + e^{2\gamma D(\Delta)(m-m_2)} \\ & + e^{\gamma D(\Delta)(2m-m_1-m_2)} \left[2\cos(\Delta\phi + k_0(m_2-m_1)) \right] \end{aligned} \tag{B.33}$$

In the limit of small γ compared to $t|m_1 - m_2|$, we have $e^{-\gamma D(\Delta)|m-m_2|} \approx e^{-\gamma D(\Delta)|m-m_1|}$ allowing us to write

$$I_m / (|F|^2 D(\Delta)^2) \approx 2e^{2\gamma D(\Delta)(m-m_1)} \left[1 + \cos\left(\Delta\phi + k_0(m_2-m_1)\right) \right], \tag{B.34}$$

which is equal to 0 in the case where

$$\Delta\phi + k_0(m_2 - m_1) = (2\ell+1)\pi, \quad \ell \in \mathbb{Z}. \tag{B.35}$$

This is the phase matching condition (Equation 2.10) in Chapter 2.

BIBLIOGRAPHY

[1] I. L. Garanovich et al., 'Light propagation and localization in modulated photonic lattices and waveguides,' Physics Reports, vol. 518, no. 1, pp. 1–79, 2012 (cit. on p. 1).

[2] M. Polini et al., 'Artificial honeycomb lattices for electrons, atoms and photons,' Nature nanotechnology, vol. 8, no. 9, pp. 625–633, 2013 (cit. on p. 1).

[3] M.-H. Lu et al., 'Phononic crystals and acoustic metamaterials,' Materials Today, vol. 12, no. 12, pp. 34–42, 2009 (cit. on p. 1).

[4] D. Leykam et al., 'Artificial flat band systems: From lattice models to experiments,' Advances in Physics: X, vol. 3, no. 1, p. 1 473 052, 2018 (cit. on p. 1).

[5] Y. Chen et al., 'Tight-binding model in optical waveguides: Design principle and transferability for simulation of complex photonics networks,' Phys. Rev. A, vol. 104, p. 023 501, 2 2021 (cit. on p. 1).

[6] E. Yablonovitch, 'Photonic band-gap structures,' JOSA B, vol. 10, no. 2, pp. 283–295, 1993 (cit. on pp. 1, 40).

[7] R. D. V. Meade et al., Photonic crystals: Molding the flow of light. Princeton University Press, 2008 (cit. on pp. 1, 40).

[8] M. Bellec et al., 'Tight-binding couplings in microwave artificial graphene,' Phys. Rev. B, vol. 88, p. 115 437, 11 2013 (cit. on p. 1).

[9] T. Pertsch et al., 'Optical bloch oscillations in temperature tuned waveguide arrays,' Physical Review Letters, vol. 83, no. 23, p. 4752, 1999 (cit. on p. 1).

[10] R. Morandotti et al., 'Experimental observation of linear and nonlinear optical bloch oscillations,' Physical Review Letters, vol. 83, no. 23, p. 4756, 1999 (cit. on p. 1).

[11] Z. Wang et al., 'Reflection-free one-way edge modes in a gyromagnetic photonic crystal,' Phys. Rev. Lett., vol. 100, p. 013 905, 1 2008 (cit. on p. 1).

[12] M. C. Rechtsman et al., 'Photonic floquet topological insulators,' Nature, vol. 496, no. 7444, pp. 196–200, 2013 (cit. on pp. 1, 50).

[13] Z. Yang et al., 'Topological acoustics,' Physical review letters, vol. 114, no. 11, p. 114 301, 2015 (cit. on p. 1).

[14] F. Zangeneh-Nejad et al., 'Topological wave insulators: A review,' Comptes Rendus. Physique, vol. 21, no. 4-5, pp. 467–499, 2020 (cit. on p. 1).

[15] S. Mukherjee et al., 'Observation of a localized flat-band state in a photonic lieb lattice,' Phys. Rev. Lett., vol. 114, p. 245 504, 24 2015 (cit. on p. 1).

[16] L. Tang et al., 'Photonic flat-band lattices and unconventional light localization,' Nanophotonics, vol. 9, no. 5, pp. 1161–1176, 2020 (cit. on pp. 1, 50).

[17] R. A. Vicencio et al., 'Observation of localized states in lieb photonic lattices,' Physical review letters, vol. 114, no. 24, p. 245 503, 2015 (cit. on pp. 1, 50).

[18] T. Ramos et al., 'Topological input-output theory for directional amplification,' Physical Review A, vol. 103, no. 3, p. 033 513, 2021 (cit. on p. 2).

[19] A. González-Tudela, 'Connecting steady-states of driven-dissipative photonic lattices with spontaneous collective emission phenomena,' New Journal of Physics, vol. 24, no. 4, p. 043 001, 2022 (cit. on pp. 2, 102).

[20] C. Noh et al., 'Quantum simulations and many-body physics with light,' Reports on Progress in Physics, vol. 80, no. 1, p. 016 401, 2016 (cit. on p. 2).

[21] M. Biondi et al., 'Spatial correlations in driven-dissipative photonic lattices,' New Journal of Physics, vol. 19, no. 12, p. 125 016, 2017 (cit. on p. 2).

[22] C. Wang et al., 'Non-hermitian optics and photonics: From classical to quantum,' Advances in Optics and Photonics, vol. 15, no. 2, pp. 442–523, 2023 (cit. on pp. 2, 3).

[23] M. Wouters et al., 'Superfluidity and critical velocities in nonequilibrium bose-einstein condensates,' Physical review letters, vol. 105, no. 2, p. 020 602, 2010 (cit. on p. 2).

[24] C. Hahn et al., 'Observation of exceptional points in reconfigurable non-hermitian vector-field holographic lattices,' Nature communications, vol. 7, no. 1, p. 12 201, 2016 (cit. on p. 3).

[25] M.-A. Miri et al., 'Exceptional points in optics and photonics,' Science, vol. 363, no. 6422, eaar7709, 2019 (cit. on p. 3).

[26] L. Feng et al., 'Non-hermitian photonics based on parity–time symmetry,' Nature Photonics, vol. 11, no. 12, pp. 752–762, 2017 (cit. on p. 3).

[27] H. Zhao et al., 'Parity–time symmetric photonics,' National science review, vol. 5, no. 2, pp. 183–199, 2018 (cit. on p. 3).

[28] Y. Song et al., 'Two-dimensional non-hermitian skin effect in a synthetic photonic lattice,' Phys. Rev. Appl., vol. 14, p. 064 076, 6 2020 (cit. on p. 3).

[29] S. Longhi, 'Incoherent non-hermitian skin effect in photonic quantum walks,' Light: Science & Applications, vol. 13, no. 1, p. 95, 2024 (cit. on p. 3).

[30] L. Chusseau et al., 'Mode competition in a dual-mode quantum-dot semiconductor microlaser,' Phys. Rev. A, vol. 88, p. 015 803, 1 2013 (cit. on p. 3).

[31] R. Iwami et al., 'Chaotic mode-competition dynamics in a multimode semiconductor laser with optical feedback and injection,' Optics Express, vol. 31, no. 7, pp. 11 274–11 291, 2023 (cit. on p. 3).

[32] L. A. Lugiato, 'Ii theory of optical bistability,' in Progress in optics, vol. 21, Elsevier, 1984, pp. 69–216 (cit. on p. 3).

[33] H. Gibbs, Optical bistability: controlling light with light. Elsevier, 2012 (cit. on p. 3).

[34] A. Baas et al., 'Optical bistability in semiconductor microcavities,' Phys. Rev. A, vol. 69, p. 023 809, 2 2004 (cit. on p. 3).

[35] P. Grelu et al., 'Dissipative solitons for mode-locked lasers,' Nature photonics, vol. 6, no. 2, pp. 84–92, 2012 (cit. on p. 3).

[36] H. Souissi et al., 'Mode-locked waveguide polariton laser,' Optica, vol. 11, no. 7, pp. 962–970, 2024 (cit. on p. 3).

[37] E. Cancellieri et al., 'Multistability of a two-component exciton-polariton fluid,' Physical Review B—Condensed Matter and Materials Physics, vol. 83, no. 21, p. 214 507, 2011 (cit. on p. 3).

[38] Z.-F. Yu et al., 'Non-hermitian spectrum and multistability in exciton-polariton condensates,' Phys. Rev. B, vol. 104, p. 235 408, 23 2021 (cit. on p. 3).

[39] C. Weisbuch et al., 'Observation of the coupled exciton-photon mode splitting in a semiconductor quantum microcavity,' Physical review letters, vol. 69, no. 23, p. 3314, 1992 (cit. on pp. 3, 12, 16–18).

[40] C. Ciuti et al., 'Role of the exchange of carriers in elastic exciton-exciton scattering in quantum wells,' Physical Review B, vol. 58, no. 12, p. 7926, 1998 (cit. on pp. 3, 21).

[41] M. Vladimirova et al., 'Polariton-polariton interaction constants in microcavities,' Physical Review B—Condensed Matter and Materials Physics, vol. 82, no. 7, p. 075 301, 2010 (cit. on pp. 3, 21).

[42] P. Walker et al., 'Suppression of zeeman splitting of the energy levels of exciton-polariton condensates in semiconductor microcavities in an external magnetic field,' Physical review letters, vol. 106, no. 25, p. 257 401, 2011 (cit. on p. 3).

[43] S. Klembt et al., 'Exciton-polariton topological insulator,' Nature, vol. 562, no. 7728, pp. 552–556, 2018 (cit. on pp. 4, 29, 30).

[44] A. Amo et al., 'Exciton-polaritons in lattices: A non-linear photonic simulator,' Comptes Rendus Physique, vol. 17, no. 8, pp. 934–945, 2016 (cit. on pp. 4, 12, 40).

[45] S. Rahimzadeh Kalaleh Rodriguez et al., 'Nonlinear polariton localization in strongly coupled driven-dissipative microcavities,' ACS Photonics, vol. 5, no. 1, pp. 95–99, 2018 (cit. on pp. 4, 5).

[46] M. Milićević et al., 'Lasing in optically induced gap states in photonic graphene,' SciPost Physics, vol. 5, no. 6, p. 064, 2018 (cit. on p. 5).

[47] V. Goblot et al., 'Nonlinear polariton fluids in a flatband reveal discrete gap solitons,' Physical Review Letters, vol. 123, no. 11, p. 113 901, 2019 (cit. on p. 5).

[48] S. Lovett et al., 'Flat-band compactons in a two-dimensional driven-dissipative lieb lattice,' arXiv preprint arXiv:2506.03963, 2025 (cit. on p. 5).

[49] O. Jamadi et al., 'Reconfigurable photon localization by coherent drive and dissipation in photonic lattices,' Optica, vol. 9, no. 7, pp. 706–712, 2022 (cit. on pp. 5, 51, 54).

[50] B. Real et al., 'Controlling directional propagation in driven two-dimensional photonic lattices,' Opt. Exp., vol. 32, no. 26, pp. 47 458–47 467, 2024 (cit. on pp. 5, 42, 102).

[51] G. Usaj, 'Localization engineering by resonant driving in dissipative polariton arrays,' SciPost Physics Core, vol. 7, no. 3, p. 052, 2024 (cit. on pp. 5, 51, 102).

[52] A. Muñoz de las Heras et al., 'Nonlinearity-enabled localization in driven-dissipative photonic lattices,' Physical Review A, vol. 109, no. 6, p. 063 523, 2024 (cit. on pp. 5, 101).

[53] M.-S. Hwang et al., 'Ultralow-threshold laser using super-bound states in the continuum,' Nature Communications, vol. 12, no. 1, p. 4135, 2021 (cit. on pp. 6, 7).

[54] P. Miao et al., 'Orbital angular momentum microlaser,' Science, vol. 353, no. 6298, pp. 464–467, 2016 (cit. on pp. 6, 7).

[55] P. St-Jean et al., 'Lasing in topological edge states of a one-dimensional lattice,' Nature Photonics, vol. 11, no. 10, pp. 651–656, 2017 (cit. on pp. 6, 7).

[56] M. Nixon et al., 'Observing geometric frustration with thousands of coupled lasers,' Phys. Rev. Lett., vol. 110, p. 184 102, 18 May 2013 (cit. on pp. 6, 7).

[57] Z. Qiao et al., 'High orbital angular momentum lasing with tunable degree of chirality in a symmetry-broken microcavity,' Optica, vol. 10, no. 7, pp. 846–853, 2023 (cit. on p. 7).

[58] L. Pickup et al., 'Synthetic band-structure engineering in polariton crystals with non-hermitian topological phases,' Nature communications, vol. 11, no. 1, p. 4431, 2020 (cit. on p. 7).

[59] S. Klembt et al., 'Polariton condensation in S- and P-flatbands in a two-dimensional Lieb lattice,' Applied Physics Letters, vol. 111, no. 23, p. 231 102, 2017 (cit. on pp. 7, 8, 71, 72).

[60] C. E. Whittaker et al., 'Exciton Polaritons in a Two-Dimensional Lieb Lattice with Spin-Orbit Coupling,' Phys. Rev. Lett., vol. 120, no. 9, p. 97 401, 2018 (cit. on pp. 8, 71, 72).

[61] R. P. Feynman, 'Simulating physics with computers,' in Feynman and computation, cRc Press, 2018, pp. 133–153 (cit. on p. 12).

[62] I. Bloch et al., 'Many-body physics with ultracold gases,' Reviews of modern physics, vol. 80, no. 3, pp. 885–964, 2008 (cit. on p. 12).

[63] R. Blatt et al., 'Quantum simulations with trapped ions,' Nature Physics, vol. 8, no. 4, pp. 277–284, 2012 (cit. on p. 12).

[64] Y. Makhlin et al., 'Quantum-state engineering with josephson-junction devices,' Reviews of modern physics, vol. 73, no. 2, p. 357, 2001 (cit. on p. 12).

[65] J. L. O'brien et al., 'Photonic quantum technologies,' Nature photonics, vol. 3, no. 12, pp. 687–695, 2009 (cit. on p. 12).

[66] A. Aspuru-Guzik et al., 'Photonic quantum simulators,' Nature physics, vol. 8, no. 4, pp. 285–291, 2012 (cit. on p. 12).

[67] I. Carusotto et al., 'Quantum fluids of light,' Reviews of Modern Physics, vol. 85, no. 1, pp. 299–366, 2013 (cit. on pp. 12, 18, 30).

[68] D. Sanvitto et al., 'The road towards polaritonic devices,' Nature materials, vol. 15, no. 10, pp. 1061–1073, 2016 (cit. on p. 12).

[69] G. Tosi et al., 'Sculpting oscillators with light within a nonlinear quantum fluid,' Nature physics, vol. 8, no. 3, pp. 190–194, 2012 (cit. on p. 12).

[70] P. Yeh, 'Optical waves in layered media,' 2006 (cit. on pp. 12, 13).

[71] H. A. Macleod et al., Thin-film optical filters. CRC press, 2010 (cit. on p. 12).

[72] M. BornandE, 'Wolf, principles of optics,' Chapter X (London, 1959), 1999 (cit. on p. 13).

[73] G. Bastard, 'Wave mechanics applied to semiconductor heterostructures,' 1990 (cit. on pp. 14, 16).

[74] D. A. B. Miller et al., 'Electric field dependence of optical absorption near the band gap of quantum-well structures,' Phys. Rev. B, vol. 32, pp. 1043–1060, 1985 (cit. on p. 14).

[75] D. Bimberg et al., Quantum Dot Heterostructures. Wiley, 1999 (cit. on p. 14).

[76] N. Pernet, 'Non-linear physics associated to chiral symmetry in driven dissipative polariton lattices,' Ph.D. dissertation, Université Paris-Saclay, 2022 (cit. on p. 15).

[77] A. Rahimi-Iman, 'Polariton physics,' Springer Series in Optical Sciences, vol. 229, 2020 (cit. on pp. 15, 21).

[78] G. Bastard et al., 'Exciton binding energy in quantum wells,' Physical Review B, vol. 26, no. 4, p. 1974, 1982 (cit. on p. 15).

[79] P. Savvidis et al., 'Angle-resonant stimulated polariton amplifier,' Physical review letters, vol. 84, no. 7, p. 1547, 2000 (cit. on p. 16).

[80] B. Deveaud et al., 'Radiative properties of a highly excited quantum well,' Appl. Phys. Lett., vol. 58, no. 14, p. 1485, 1991 (cit. on p. 16).

[81] L. C. Andreani et al., 'Accurate theory of excitons in gaas-ga 1- x al x as quantum wells,' Physical Review B, vol. 42, no. 14, p. 8928, 1990 (cit. on p. 16).

[82] J.-M. Gérard et al., 'Enhanced spontaneous emission by quantum boxes in a monolithic optical microcavity,' Physical review letters, vol. 81, no. 5, p. 1110, 1998 (cit. on p. 16).

[83] V. Savona et al., 'Quantum well excitons in semiconductor microcavities: Unified treatment of weak and strong coupling regimes,' Solid State Communications, vol. 93, no. 9, pp. 733–739, 1995 (cit. on p. 16).

[84] G. Khitrova et al., 'Vacuum rabi splitting in semiconductors,' Nature physics, vol. 2, no. 2, pp. 81–90, 2006 (cit. on p. 16).

[85] E. M. Purcell et al., 'Resonance absorption by nuclear magnetic moments in a solid,' Physical review, vol. 69, no. 1-2, p. 37, 1946 (cit. on p. 17).

[86] A. Kavokin et al., Microcavities. Oxford university press, 2017 (cit. on pp. 17, 18, 20).

[87] P. Goy et al., 'Observation of cavity-enhanced single-atom spontaneous emission,' Physical review letters, vol. 50, no. 24, p. 1903, 1983 (cit. on p. 17).

[88] J. J. Hopfield, 'Theory of the Contribution of Excitons to the Complex Dielectric Constant of Crystals,' Phys. Rev., vol. 112, no. 5, pp. 1555–1567, 1958 (cit. on pp. 17, 18).

[89] H. Benisty et al., Confined photon systems: fundamentals and applications. Springer, 1999 (cit. on p. 18).

[90] H. Haug et al., Quantum theory of the optical and electronic properties of semiconductors. world scientific, 2009 (cit. on p. 18).

[91] S. Christopoulos et al., 'Room-temperature polariton lasing in semiconductor microcavities,' Physical review letters, vol. 98, no. 12, p. 126 405, 2007 (cit. on p. 18).

[92] J. Kasprzak et al., 'Bose–einstein condensation of exciton polaritons,' Nature, vol. 443, no. 7110, pp. 409–414, 2006 (cit. on p. 20).

[93] A. Amo et al., 'Superfluidity of polaritons in semiconductor microcavities,' Nature Physics, vol. 5, no. 11, pp. 805–810, 2009 (cit. on p. 20).

[94] F. Tassone et al., 'Exciton-exciton scattering dynamics in a semiconductor microcavity and stimulated scattering into polaritons,' Physical Review B, vol. 59, no. 16, p. 10 830, 1999 (cit. on p. 21).

[95] I. Frérot et al., 'Bogoliubov excitations driven by thermal lattice phonons in a quantum fluid of light,' Physical Review X, vol. 13, no. 4, p. 041 058, 2023 (cit. on pp. 22, 23, 61).

[96] V. R. Pande, 'Analysis of exciton-polariton condensation under different pumping schemes for 1d and 2d microcavities including the effect of strong correlation between polaritons,' arXiv preprint arXiv:2501.02958, 2025 (cit. on pp. 22, 24).

[97] M. Milicevic, 'Manipulation of dirac cones and edge states in polariton honeycomb lattices,' Ph.D. dissertation, Sorbonne Université, 2018 (cit. on pp. 23, 31).

[98] D. Porras et al., 'Polariton dynamics and bose-einstein condensation in semiconductor microcavities,' Physical Review B, vol. 66, no. 8, p. 085 304, 2002 (cit. on p. 24).

[99] M. Wouters et al., 'Excitations in a nonequilibrium bose-einstein condensate of exciton polaritons,' Physical review letters, vol. 99, no. 14, p. 140 402, 2007 (cit. on p. 24).

[100] B. M. R. Elgueda, 'Transport and driven-dissipative localization in exciton-polariton lattices,' Ph.D. dissertation, Université de Lille, 2022 (cit. on pp. 25, 54).

[101] C. Schneider et al., 'Exciton-polariton trapping and potential landscape engineering,' Reports on Progress in Physics, vol. 80, no. 1, p. 016 503, 2016 (cit. on p. 27).

[102] C. Ciuti et al., 'Theory of polariton parametric interactions in semiconductor microcavities,' Semiconductor science and technology, vol. 18, no. 10, S279, 2003 (cit. on p. 27).

[103] R. Balili et al., 'Bose-einstein condensation of microcavity polaritons in a trap,' Science, vol. 316, no. 5827, pp. 1007–1010, 2007 (cit. on p. 27).

[104] E. Cerda-Méndez et al., 'Polariton condensation in dynamic acoustic lattices,' Physical review letters, vol. 105, no. 11, p. 116 402, 2010 (cit. on p. 27).

[105] E. Cerda-Méndez et al., 'Exciton-polariton gap solitons in two-dimensional lattices,' Physical review letters, vol. 111, no. 14, p. 146 401, 2013 (cit. on p. 27).

[106] E. Cerda-Méndez et al., 'Quantum fluids of light in acoustic lattices,' Journal of Physics D: Applied Physics, vol. 51, no. 3, p. 033 001, 2017 (cit. on p. 27).

[107] E. Wertz et al., 'Spontaneous formation and optical manipulation of extended polariton condensates,' Nature physics, vol. 6, no. 11, pp. 860–864, 2010 (cit. on p. 28).

[108] A. Askitopoulos et al., 'Polariton condensation in an optically induced two-dimensional potential,' Physical Review B—Condensed Matter and Materials Physics, vol. 88, no. 4, p. 041 308, 2013 (cit. on pp. 28, 97).

[109] N. G. Berloff et al., 'Realizing the classical xy hamiltonian in polariton simulators,' Nature materials, vol. 16, no. 11, pp. 1120–1126, 2017 (cit. on p. 28).

[110] S. Alyatkin et al., 'Quantum fluids of light in all-optical scatterer lattices,' Nature Communications, vol. 12, no. 1, p. 5571, 2021 (cit. on p. 28).

[111] N. Y. Kim et al., 'Exciton–polariton condensates near the dirac point in a triangular lattice,' New Journal of Physics, vol. 15, no. 3, p. 035 032, 2013 (cit. on p. 28).

[112] N. Masumoto et al., 'Exciton–polariton condensates with flat bands in a two-dimensional kagome lattice,' New Journal of Physics, vol. 14, no. 6, p. 065 002, 2012 (cit. on p. 28).

[113] R. I. Kaitouni et al., 'Engineering the spatial confinement of exciton polaritons in semiconductors,' Physical Review B—Condensed Matter and Materials Physics, vol. 74, no. 15, p. 155 311, 2006 (cit. on p. 28).

[114] O. El Daıf et al., 'Polariton quantum boxes in semiconductor microcavities,' Applied Physics Letters, vol. 88, no. 6, 2006 (cit. on p. 28).

[115] R. Cerna et al., 'Coherent optical control of the wave function of zero-dimensional exciton polaritons,' Physical Review B—Condensed Matter and Materials Physics, vol. 80, no. 12, p. 121 309, 2009 (cit. on p. 28).

[116] K. Winkler et al., 'A polariton condensate in a photonic crystal potential landscape,' New Journal of Physics, vol. 17, no. 2, p. 023 001, 2015 (cit. on p. 28).

[117] M. Bayer et al., 'Optical demonstration of a crystal band structure formation,' Physical Review Letters, vol. 83, no. 25, p. 5374, 1999 (cit. on p. 29).

[118] C. Whittaker et al., 'Exciton polaritons in a two-dimensional lieb lattice with spin-orbit coupling,' Physical review letters, vol. 120, no. 9, p. 097 401, 2018 (cit. on p. 29).

[119] D. Bajoni et al., 'Polariton laser using single micropillar gaas-gaalas semiconductor cavities,' Physical review letters, vol. 100, no. 4, p. 047 401, 2008 (cit. on p. 30).

[120] F. Baboux et al., 'Bosonic condensation and disorder-induced localization in a flat band,' Physical review letters, vol. 116, no. 6, p. 066 402, 2016 (cit. on p. 30).

[121] S. Klembt et al., 'Polariton condensation in s-and p-flatbands in a two-dimensional lieb lattice,' Applied Physics Letters, vol. 111, no. 23, 2017 (cit. on p. 30).

[122] M. J. Hartmann et al., 'Quantum many-body phenomena in coupled cavity arrays,' Laser & Photonics Reviews, vol. 2, no. 6, pp. 527–556, 2008 (cit. on p. 30).

[123] U. Hohenester, 'Cavity quantum electrodynamics with semiconductor quantum dots: Role of phonon-assisted cavity feeding,' Physical Review B—Condensed Matter and Materials Physics, vol. 81, no. 15, p. 155 303, 2010 (cit. on p. 30).

[124] T. Jacqmin et al., 'Direct observation of dirac cones and a flatband in a honeycomb lattice for polaritons,' Physical review letters, vol. 112, no. 11, p. 116 402, 2014 (cit. on pp. 30, 68, 91).

[125] N. C. Zambon, 'Chirality and nonlinear dynamics in polariton microresonators,' Ph.D. dissertation, Université Paris-Saclay, 2020 (cit. on pp. 31–33).

[126] M. Galbiati et al., 'Polariton condensation in photonic molecules,' Physical review letters, vol. 108, no. 12, p. 126 403, 2012 (cit. on p. 34).

[127] S. Rodriguez et al., 'Interaction-induced hopping phase in driven-dissipative coupled photonic microcavities,' Nature communications, vol. 7, no. 1, p. 11 887, 2016 (cit. on p. 38).

[128] F. Mangussi et al., 'Multi-orbital tight binding model for cavity-polariton lattices,' Journal of Physics: Condensed Matter, vol. 32, no. 31, p. 315 402, 2020 (cit. on p. 39).

[129] B. A. Bell et al., 'Spectral photonic lattices with complex long-range coupling,' Optica, vol. 4, no. 11, pp. 1433–1436, 2017 (cit. on p. 40).

[130] T. Ozawa et al., 'Topological photonics,' Rev. Mod. Phys., vol. 91, no. 1, p. 015 006, 2019 (cit. on pp. 40, 50).

[131] M. Kremer et al., 'Topological effects in integrated photonic waveguide structures,' Optical Materials Express, vol. 11, no. 4, pp. 1014–1036, 2021 (cit. on p. 40).

[132] D. N. Christodoulides et al., 'Discretizing light behaviour in linear and nonlinear waveguide lattices,' Nature, vol. 424, no. 6950, pp. 817–823, 2003 (cit. on p. 40).

[133] I. L. Garanovich et al., 'Light propagation and localization in modulated photonic lattices and waveguides,' Physics Reports, vol. 518, no. 1-2, pp. 1–79, 2012 (cit. on p. 40).

[134] H. Pichler et al., 'Quantum optics of chiral spin networks,' Physical Review A, vol. 91, no. 4, p. 042 116, 2015 (cit. on p. 42).

[135] T. Ramos et al., 'Non-markovian dynamics in chiral quantum networks with spins and photons,' Physical Review A, vol. 93, no. 6, p. 062 104, 2016 (cit. on p. 42).

[136] B. Kannan et al., 'On-demand directional microwave photon emission using waveguide quantum electrodynamics,' Nature Physics, vol. 19, no. 3, pp. 394–400, 2023 (cit. on p. 42).

[137] C. Joshi et al., 'Resonance fluorescence of a chiral artificial atom,' Physical Review X, vol. 13, no. 2, p. 021 039, 2023 (cit. on p. 42).

[138] A. González-Tudela et al., 'Engineering and harnessing giant atoms in high-dimensional baths: A proposal for implementation with cold atoms,' Physical review letters, vol. 122, no. 20, p. 203 603, 2019 (cit. on p. 42).

[139] I. Carusotto et al., 'Probing Microcavity Polariton Superfluidity through Resonant Rayleigh Scattering,' Phys. Rev. Lett., vol. 93, no. 16, p. 166 401, 2004. (cit. on p. 45).

[140] A. Muñoz de las Heras et al., 'Nonlinearity-enabled localization in driven-dissipative photonic lattices,' Phys. Rev. A, vol. 109, p. 063 523, 2024 (cit. on pp. 46, 51, 56–58, 66, 106).

[141] T. Schwartz et al., 'Transport and anderson localization in disordered two-dimensional photonic lattices,' Nature, vol. 446, no. 7131, pp. 52–55, 2007 (cit. on p. 50).

[142] L. Levi et al., 'Disorder-enhanced transport in photonic quasicrystals,' Science, vol. 332, no. 6037, pp. 1541–1544, 2011 (cit. on p. 50).

[143] V. Goblot et al., 'Emergence of criticality through a cascade of delocalization transitions in quasiperiodic chains,' Nature Physics, vol. 16, no. 8, pp. 832–836, 2020 (cit. on p. 50).

[144] O. Painter et al., 'Defect modes of a two-dimensional photonic crystal in an optically thin dielectric slab,' Journal of the Optical Society of America B, vol. 16, no. 2, pp. 275–285, 1999 (cit. on p. 50).

[145] I. D. Vatnik et al., 'Anderson localization in synthetic photonic lattices,' Scientific reports, vol. 7, no. 1, p. 4301, 2017 (cit. on p. 50).

[146] S. Mukherjee et al., 'Observation of a localized flat-band state in a photonic lieb lattice,' Physical review letters, vol. 114, no. 24, p. 245 504, 2015 (cit. on p. 50).

[147] D. Leykam et al., 'Perspective: Photonic flatbands,' Apl Photonics, vol. 3, no. 7, 2018 (cit. on p. 50).

[148] C. W. Hsu et al., 'Bound states in the continuum,' Nature Reviews Materials, vol. 1, no. 9, pp. 1–13, 2016 (cit. on p. 50).

[149] G. Ordonez et al., 'Bound states in the continuum in quantum-dot pairs,' Physical Review A—Atomic, Molecular, and Optical Physics, vol. 73, no. 2, p. 022 113, 2006 (cit. on p. 50).

[150] S. Longhi, 'Bound states in the continuum in a single-level fano-anderson model,' The European Physical Journal B, vol. 57, no. 1, pp. 45–51, 2007 (cit. on p. 50).

[151] Y. Plotnik et al., 'Experimental observation of optical bound states in the continuum,' Physical review letters, vol. 107, no. 18, p. 183 901, 2011 (cit. on p. 50).

[152] A. Regensburger et al., 'Observation of defect states in pt-symmetric optical lattices,' Physical review letters, vol. 110, no. 22, p. 223 902, 2013 (cit. on p. 50).

[153] H. Ohno et al., 'Observation of "tamm states" in superlattices,' Physical Review Letters, vol. 64, no. 21, p. 2555, 1990 (cit. on p. 50).

[154] N. Malkova et al., 'Transition between tamm-like and shockley-like surface states in optically induced photonic superlattices,' Physical Review A—Atomic, Molecular, and Optical Physics, vol. 80, no. 4, p. 043 806, 2009 (cit. on p. 50).

[155] C. Symonds et al., 'Emission of tamm plasmon/exciton polaritons,' Applied Physics Letters, vol. 95, no. 15, 2009 (cit. on p. 50).

[156] M. Hafezi et al., 'Imaging topological edge states in silicon photonics,' Nat. Photon., vol. 7, no. 12, pp. 1001–1005, 2013. (cit. on p. 50).

[157] C. Poli et al., 'Selective enhancement of topologically induced interface states in a dielectric resonator chain,' Nat. Commun., vol. 6, p. 6710, Apr. 2015, Publisher: Nature Publishing Group, ISSN: 2041-1723. (cit. on p. 50).

[158] P. St-Jean et al., 'Lasing in topological edge states of a one-dimensional lattice,' Nature Photonics, vol. 11, no. 10, pp. 651–656, 2017, ISSN: 1749-4893. (cit. on p. 50).

[159] J. Noh et al., 'Topological protection of photonic mid-gap defect modes,' Nature Photonics, vol. 12, no. 7, pp. 408–415, 2018, ISSN: 1749-4893. (cit. on p. 50).

[160] S. Mittal et al., 'Photonic quadrupole topological phases,' Nature Photonics, vol. 13, pp. 692–696, 2019, ISSN: 1749-4893. (cit. on p. 50).

[161] S. Weimann et al., 'Compact surface fano states embedded in the continuum of waveguide arrays,' Physical review letters, vol. 111, no. 24, p. 240 403, 2013 (cit. on p. 50).

[162] S. Flach et al., 'Detangling flat bands into fano lattices,' Europhysics Letters, vol. 105, no. 3, p. 30 001, 2014 (cit. on p. 50).

[163] L. Morales-Inostroza et al., 'Simple method to construct flat-band lattices,' Physical Review A, vol. 94, no. 4, p. 043 831, 2016 (cit. on p. 50).

[164] A. González-Tudela et al., 'Quantum emitters in two-dimensional structured reservoirs in the nonperturbative regime,' Physical Review Letters, vol. 119, no. 14, p. 143 602, 2017 (cit. on p. 51).

[165] P. Lodahl et al., 'Controlling the dynamics of spontaneous emission from quantum dots by photonic crystals,' Nature, vol. 430, no. 7000, pp. 654–657, 2004 (cit. on p. 58).

[166] Y. Lahini et al., 'Anderson localization and nonlinearity in one-dimensional disordered photonic lattices,' Physical Review Letters, vol. 100, no. 1, p. 013 906, 2008 (cit. on p. 58).

[167] Y. Lahini et al., 'Observation of a localization transition in quasiperiodic photonic lattices,' Physical review letters, vol. 103, no. 1, p. 013 901, 2009 (cit. on p. 58).

[168] E. R. Christensen et al., 'Microscopic theory of polariton-polariton interactions,' Physical Review B, vol. 110, no. 19, p. 195 435, 2024 (cit. on p. 61).

[169] M. Richard et al., 'Excitonic oscillator-strength saturation dominates polariton-polariton interactions,' arXiv preprint arXiv:2501.07899, 2025 (cit. on p. 61).

[170] O. Painter et al., 'Science,' Science, vol. 284, no. 5421, pp. 1819–1821, 1999 (cit. on p. 68).

[171] T. Inoue et al., 'General recipe to realize photonic-crystal surface-emitting lasers with 100-w-to-1-kw single-mode operation,' Nature Communications, vol. 13, no. 1, p. 3262, 2022 (cit. on p. 68).

[172] M. Yoshida et al., 'Double-lattice photonic-crystal resonators enabling high-brightness semiconductor lasers with symmetric narrow-divergence beams,' Nature materials, vol. 18, no. 2, pp. 121–128, 2019 (cit. on p. 68).

[173] J. Bravo-Abad et al., 'Enabling single-mode behavior over large areas with photonic dirac cones,' Proceedings of the National Academy of Sciences, vol. 109, no. 25, pp. 9761–9765, 2012 (cit. on p. 68).

[174] R. Contractor et al., 'Scalable single-mode surface-emitting laser via open-dirac singularities,' Nature, vol. 608, no. 7924, pp. 692–698, 2022 (cit. on p. 68).

[175] B. Bahari et al., 'Nonreciprocal lasing in topological cavities of arbitrary geometries,' Science, vol. 358, no. 6363, pp. 636–640, 2017 (cit. on p. 68).

[176] M. A. Bandres et al., 'Topological insulator laser: Experiments,' Science, vol. 359, no. 6381, eaar4005, 2018 (cit. on p. 68).

[177] Y. Zeng et al., 'Electrically pumped topological laser with valley edge modes,' Nature, vol. 578, no. 7794, pp. 246–250, 2020 (cit. on p. 68).

[178] B. Bahari et al., 'Photonic quantum hall effect and multiplexed light sources of large orbital angular momenta,' Nature Physics, vol. 17, no. 6, pp. 700–703, 2021 (cit. on p. 68).

[179] A. Dikopoltsev et al., 'Topological insulator vertical-cavity laser array,' Science, vol. 373, no. 6562, pp. 1514–1517, 2021 (cit. on p. 68).

[180] C. Bennenhei et al., 'Organic room-temperature polariton condensate in a higher-order topological lattice,' ACS photonics, vol. 11, no. 8, pp. 3046–3054, 2024 (cit. on p. 68).

[181] C. Cantillano et al., 'Observation of dipolar transport in one-dimensional photonic lattices,' Science Bulletin, vol. 62, no. 5, pp. 339–344, 2017 (cit. on p. 68).

[182] Y. Zhang et al., 'Realization of photonic p-orbital higher-order topological insulators,' Elight, vol. 3, no. 1, p. 5, 2023 (cit. on p. 68).

[183] R. A. Vicencio, 'Multi-orbital photonic lattices,' APL Photonics, vol. 10, no. 7, 2025 (cit. on p. 68).

[184] G. Wirth et al., 'Evidence for orbital superfluidity in the p-band of a bipartite optical square lattice,' Nature Physics, vol. 7, no. 2, pp. 147–153, 2011 (cit. on p. 68).

[185] X. Li et al., 'Topological states in a ladder-like optical lattice containing ultracold atoms in higher orbital bands,' Nature communications, vol. 4, no. 1, p. 1523, 2013 (cit. on p. 68).

[186] W. Beugeling et al., 'Topological states in multi-orbital hgte honeycomb lattices,' Nature communications, vol. 6, no. 1, p. 6316, 2015 (cit. on p. 68).

[187] M. Galbiati et al., 'Polariton Condensation in Photonic Molecules,' Phys. Rev. Lett., vol. 108, no. 12, p. 126 403, 2012 (cit. on p. 69).

[188] C. Schneider et al., 'Exciton-polariton trapping and potential landscape engineering,' Reports on Progress in Physics, vol. 80, p. 016 503, 2017 (cit. on p. 69).

[189] G. Nardin et al., 'Probability density optical tomography of confined quasiparticles in a semiconductor microcavity,' Appl. Phys. Lett., vol. 94, no. 18, p. 181 103, 2009 (cit. on p. 72).

[190] S. R. K. Rodriguez et al., 'Interaction-induced hopping phase in driven-dissipative coupled photonic microcavities,' Nat. Commun., vol. 7, p. 11 887, 2016 (cit. on p. 74).

[191] R. Butté et al., 'Transition from strong to weak coupling and the onset of lasing in semiconductor microcavities,' Phys. Rev. B, vol. 65, no. 20, p. 205 310, 2002 (cit. on p. 74).

[192] I. Carusotto et al., 'Quantum fluids of light,' Reviews of Modern Physics, vol. 85, no. 1, pp. 299–366, 2013 (cit. on p. 88).

[193] T. M. Blessan et al., 'Directional transport and nonlinear localization of light in a one-dimensional driven-dissipative photonic lattice,' Physical Review Research, vol. 7, no. 3, p. 033 283, 2025 (cit. on p. 88).

[194] F. Baboux et al., 'Unstable and stable regimes of polariton condensation,' Optica, vol. 5, no. 10, pp. 1163–1170, 2018 (cit. on p. 89).

[195] Q. Fontaine et al., 'Kardar–Parisi–Zhang universality in a one-dimensional polariton condensate,' Nature, vol. 608, no. 7924, pp. 687–691, 2022 (cit. on p. 89).

[196] C. W. Lai et al., 'Coherent zero-state and p-state in an exciton-polariton condensate array,' Nature, vol. 450, p. 529, 2007 (cit. on p. 91).

[197] D. Tanese et al., 'Polariton condensation in solitonic gap states in a one-dimensional periodic potential,' Nat. Commun., vol. 4, p. 1749, 2013 (cit. on p. 91).

[198] H. Ohadi et al., 'Spontaneous Spin Bifurcations and Ferromagnetic Phase Transitions in a Spinor Exciton-Polariton Condensate,' Phys. Rev. X, vol. 5, no. 3, p. 031 002, 2015 (cit. on p. 92).

[199] L. S. Ricco et al., 'Qubit gate operations in elliptically trapped polariton condensates,' Scientific Reports, vol. 14, no. 1, p. 4211, 2024 (cit. on p. 97).

[200] S. Alyatkin et al., 'Optical control of couplings in polariton condensate lattices,' Physical Review Letters, vol. 124, no. 20, p. 207 402, 2020 (cit. on p. 97).

[201] N. Pernet et al., 'Gap solitons in a one-dimensional driven-dissipative topological lattice,' Nature Physics, vol. 18, no. 6, pp. 678–684, 2022 (cit. on p. 102).

[202] H. Suchomel et al., 'Platform for electrically pumped polariton simulators and topological lasers,' Physical review letters, vol. 121, no. 25, p. 257 402, 2018 (cit. on p. 102).

[203] H. Suchomel et al., 'Spatio-temporal coherence in vertically emitting gaas-based electrically driven polariton lasers,' Applied Physics Letters, vol. 116, no. 17, 2020 (cit. on p. 102).